

Instituto Tecnológico y de Estudios Superiores de Monterrey

Campus Monterrey

School of Engineering and Sciences



**Auxetic Lattice Sensor for In-Socket Load Evaluation**

A thesis presented by

**Diana Laura Ramírez Gutiérrez**

Submitted to the

School of Engineering and Sciences

in partial fulfillment of the requirements for the degree of

Master of Science

Monterrey, Nuevo León, June, 2022

©2022 by Diana Laura Ramírez Gutiérrez  
All Rights Reserved

# Acknowledgements

I would like to express my deepest gratitude to all those who have been side by side with me. First to my advisor, Dr Enrique Cuan, for introducing me to the scientific world and being an exceptional guide in this research project (even though many meetings would end up in more work to add to my "pendings list"); and for each "keep it up" that made the thesis to seem not so scary. To Dr Rita, for her valuable and uncountable knowledge shared to achieve this work, and for being ready and available to solve my many doubts. I am very grateful to Dr Armando Roman and Dr Manuel Navarro for their suggestions to improve my work. And to Marco Antonio Alcaráz and Jorge León for the assistance provided in the laboratories.

To all my friends and class mates. Cesar, Albert, Mario, Mauricio, Jose Luis, and all the Metamaterials Lab people, who shared with me suggestions to survive the MsC and tips for cool figures. Also, to the Cyberphysical Lab people (Dani, Emmanuel, Juan, Alex and Dr. Gustavo), for making me feel the most welcome during my GDL stay. My sincere gratitude to the ones that were here before I started this adventure, and are here still, my dearest friends Ana Pau, Edgardo, Ali, Pablo, Fer, Ana Karen, Cesar, Karen, Arturo, Cris, and Barbi. And for being here since forever, Mari, Pao and Jime. To the friends that were added to the list along this trip. Joy, who made the project look fun and not so lonely; Juan, for his support in every chapter delivery; and my folklore's incredible team, Ismali, Zin, Mon and Noy, who where with me everyday along the way ready to celebrate or listen to my ups and downs.

Finally, I could never find the enough words to express my deepest and sincerest gratitude to my family, Emma, Rodo, Clau and Emi. For their unconditional love and for always encouraging me to pursue my dreams.

I could not finish a list of people that were somehow involved in this project. Thanks to everyone. Finally, Tecnológico de Monterrey support on tuition and CONACyT with the support for living are acknowledged.

# **Auxetic Lattice Sensor for In-Socket Load Evaluation**

by

Diana Laura Ramírez Gutiérrez

## **Abstract**

Auxetic metamaterials present an uncommon dome shape when subjected to an out-of-plane bending moment, known as synclasticity. This property has them potential candidates in aerospace, biomedical and textiles. Currently, the use of wearable devices has increased. These sensors allow the tracking of physical activity of the human body, which provide useful information about health. They need to withstand repeated large deformations and conform to the complex curved geometries of the human body without loss in performance. Conformability has presented a challenge in materials science and engineering and one approach to overcome this, has been the implementation of auxetic topologies. Still, most applications remain in their infancy and require more research. Despite biomedical sensors being subjected to complex loading conditions, most of the literature has focused on auxetic metamaterials under simple tensile and compressive loadings.

The geometrical parameter-Poisson's ratio was thoroughly characterized via Finite element modeling (FEM). This brought up a thorough relation between their geometrical parameters and auxeticity. Their out-of-plane stiffness was also characterized via FEM and corroborated with additive manufactured samples subjected to the same boundary conditions. A conformability ratio was computed with digital image processing, and a generalized linear model of 95% confidence interval exhibited the relation between each parameter and this property. Topologies with similar conformability ratio were found, which allowed to establish a relation between geometrical parameters, conformability and stiffness.

Finally, the fabrication of pressure-sensing devices was achieved by the instrumentation of velostat with different auxetic porous arrangements. This exposed a general view of their electric response under different loading conditions. These devices were also tested as in-socket pressure sensors, establishing a link between their electric and mechanical

response while being stretched to conform an artificial residual limb. This, in addition to in-plane, and out-of-plane characterization, lead to key properties when deciding the geometry specific for applications; deformation mechanism, relative density, auxetic behavior and stiffness.

# List of Figures

1.1	Material under tension with Poisson’s ratio a. Positive, and b. Negative . . . . .	2
1.2	Types of behavior of materials subjected to out-of-plane bending moment exhibiting a. Anticlastic (saddle shape) and b. Synclastic (dome shape). . . . .	2
2.1	Examples of re-entrant auxetic structures: a. bowtie honeycomb, b. triangular re-entrant, and c. re-entrant star structure. . . . .	11
2.2	Re-entrant structures in applications: fashion items using the a. triangular re-entrant [44] and b. the bowtie honeycomb [33]; c. cardiac patch for the treatment of myocardial infarction [21]; d. 3D printed ionogel strain sensor [27], e. Piezoresistive hybrid sensor [32], f. Stretchable strain sensor [53], g. Graphene-based stretchable/wearable touch sensor [28], and h. 3D printed hydrogel strain sensor [18]. . . . .	12
2.3	Rotating unit mechanisms a. Square and b. Triangle; and examples of applications: c. Bandage substrate film for elbows [51], and d. Force sensor film for hand rehabilitation [24]. . . . .	13
2.4	a. tetrachiral, b. hexachiral, and c. anti-tetrachiral auxetic structures; and d. Piezoelectric strain sensor diagram in the form of anti-tetrachiral structures [9]. . . . .	14
2.5	a. Sinusoidal pattern implemented as a. 3D printed clothing for curved objects [19], and a capacitive sensor mounted onto b. Universal jamming gripper, and c. Human elbow[56]. . . . .	14

3.1	Schematics of the topologies chosen for the study: a. (1) Sinusoidal lattice W1, with a representation of its (2) unit cell, and (3) the parameters that define it; b. (1) Sinusoidal lattice W2, with a representation of its (2) unit cell and parameters that define it; and c. (1) Square lattice, with a representation of its (2) unit cell and the parameters that define it. . . . .	28
3.2	Process for the computational design of the square and sinusoidal lattices a. Square, b. Topology W2, and c. Topology W3. For a and b, 1. is the result of the macro implemented in SOLIDWORKS, 2. Extrusion of 1 mm to create a solid and 3. Repetition of unit cells to create the lattice. For c, 1. Curves result of the macro, 2. Curves mirrored in both axes to create the unit cell, 3. The surface was extruded 1 mm, and 4. A matrix of the solid unit cell was done to obtain a $5 \times 5$ cm lattice. . . . .	30
3.3	Process to compute relative density of sinusoidal topologies a. W2, and b. W1. Showing 1. External volume of the unit cell, 2, sine curves with length $s$ and thickness $t$ , and 3. Fraction of $t^2$ because of the inter crossing of each curve. . .	31
3.4	Square and sinusoidal lattices samples with equivalent values of relative density. $\lambda$ , $t$ and $A$ are in mm. . . . .	32
3.5	Illustration of the samples with minimum (up) and maximum (down) values of the variations of Topology W1's parameters a. Amplitude $A$ , b. Thickness $t$ , and c. Length of unit cell $\lambda$ ; and Topology W2's d. Amplitude $A$ , e. Thickness $t$ , and f. Length of unit cell $\lambda$ . . . . .	33
3.6	FEA of compression test to compute Poisson's ratio of the samples using shell elements: a. Variable $w$ to establish shell elements of the samples, b. Boundary Conditions of the samples subjected to compression, and c. Nodes of the samples were displacements were taken to do the calculations. . . . .	34
3.7	FEA of tensile test to compute Poisson's ratio of the samples: a. Fixed support and tensile load $F$ applied to the sample, b. Illustration of the nodes selected to calculate Poisson's ratio, its height ( $h$ ) and width ( $w$ ); and c. Illustration of the displacements in $x$ and $y$ used to calculate the strain. . . . .	35

3.8	Mesh obtained in different tests, FEA software, and element types: a. Tension in COMSOL Multiphysics using tetrahedral elements, b. Tension in ANSYS Workbench using tetrahedral elements, c. Compression in COMSOL Multiphysics using shell elements, d. Compression in ANSYS Workbench using shell elements, and e. Tension in ANSYS APDL using beam elements. . . . .	36
3.9	Results of $\nu$ for topology W1, presented as an individual plot for each modified parameter: a. Thickness $t$ , b. Amplitude $A$ , and c. Length of the unit cell $\lambda$ . The $y$ axis of all plots corresponds to plot a. Comparison of the results of $\nu$ for topology W1 in relation with the ratio of two parameters: d. Amplitude and length of the unit cell $A/\lambda$ , e. Amplitude and thickness $A/t$ , and f. Thickness and length of the unit cell $t/\lambda$ . . . . .	37
3.10	Results of $\nu$ for topology W2, presented as an individual plot for each modified parameter: a. Thickness $t$ , b. Amplitude $A$ , and c. Length of the unit cell $\lambda$ . The $y$ axis of all plots corresponds to plot a. Comparison of the results of $\nu$ for topology W2 in relation with the ratio of two parameters: d. Amplitude and length of the unit cell $A/\lambda$ , e. Amplitude and thickness $A/t$ , and f. Thickness and length of the unit cell $t/\lambda$ . . . . .	39
3.11	$\nu$ results of additional samples of topology W2, fixing $t = 0.5$ with modifications of a. Amplitude $A$ , and b. Length of the unit cell $\lambda$ ; and c. comparison of all the modifications made of topology W2 in relation with $t/\lambda$ ratio. The dashed line marks $\nu = 0$ to separate auxetic and non-auxetic results. . . . .	40
4.1	Samples designed for the study of the square and sinusoidal lattice, grouped by their parameters. All units in mm. . . . .	44
4.2	Experimental setup to hold the sample in place consisting on four pairs of jaws hold by a support that is placed on a base fixed to the texture analyzer. a. Top and b. Front views . . . . .	45
4.3	Boundary conditions to evaluate $k$ on FEA simulations. a. Top view showing the fixed supports on the corners of the samples, b. Front view illustrating the applied force on the face of the fractioned sphere. . . . .	46



4.4	Main effects plots of each parameter grouped by sinusoid topologies a. W1 and b. W2, including the square lattice into each group as a sinusoid lattice with zero amplitude. <i>y</i> axis is the same for both plots. . . . .	47
4.5	Stiffness <i>k</i> in terms of the length of the unit cell $\lambda$ plots grouped by type of topology a. Square, b. Topology W1, and c. Topology W2 lattices. <i>y</i> axis is the same for all plots. . . . .	48
4.6	Stiffness <i>k</i> in terms of thickness <i>t</i> plots grouped by type of topology a. Square, b. Topology W1, and c. Topology W2 lattices. <i>y</i> axis is the same for all plots. . . .	49
4.7	Stiffness <i>k</i> in terms of the amplitude <i>A</i> plots grouped by sinusoid topologies a. W1 and b. W2, including the square lattice into each group as a sinusoid lattice with zero amplitude. <i>y</i> axis is the same for both plots. . . . .	49
4.8	Stiffness <i>k</i> calculated thru simulations in terms of type of topology, only samples with equivalent relative density $\bar{\rho}$ were included. For topology W1 high <i>A</i> 's value corresponds to 0.5, and low <i>A</i> to 1.6, for topology W1 the values are 0.25 and 0.8 respectively. . . . .	50
4.9	Force-displacement plots of experimental tests of sinusoidal topology a. W1- $\lambda 5 - t 0.5$ , and b. W2- $\lambda 5 - t 0.5$ , each curve corresponds to different amplitudes, including the square lattice into each group as a sinusoid lattice with zero amplitude. <i>y</i> axis is the same for both plots. . . . .	51
4.10	Deformed shapes of the a. Square, b. Topology W1 and c. Topology W2 lattices during out-of-plane loading in 1. experimental tests and FEA simulations 1. front view and 2. isometric view. The dashed line shows the difference between the deformation of square and the sinusoidal topologies lattices. . . . .	52
4.11	Force-displacement plot from the experimental run of the sample designed with topology W1, $\lambda = 5$ mm, $t = 5$ mm and $A = 1.6$ mm, run 1. Slope 1 marks the beginning of the test (sphere touches the sample), slope 2 occurs when the sample slides from the clamps, and slope 3 possible combination of plastic deformation of the sample and bending of the experimental setup. . . . .	52
4.12	Standard deviation and FEA results of stiffness <i>k</i> from a. Original CAD and b. CAD with adjustments of <i>t</i> and <i>w</i> , showing the reduction of error between both characterizations. . . . .	55

4.13	Image processing methodology in the software ImageJ after the experimental out-of-plane loading tests of fabricated samples. a. Decomposition of the 1. Original RGB color image; into the RGB stack presented as 8 bit images for each channel: 2. Red, 3. Green, and 4. Blue; b. Process to isolate the painted area of the sample: 1. Red channel from the stack, 2. Adjustment of the threshold to filter the pixels that belong to the painted area, and 3. Resulting isolated painted area; and c. Process to separate the total area of the sample from the background: 1. Resulting image of the subtraction Red-Green channels, 2. Adjustment of the threshold to filter the pixels that belong to the sample, 3. Resulting isolated sample, with changed values of the pixels. . . . .	58
4.14	Geometrical selections of the processed images to obtain a. External area of the sample $A_e$ and b. Touching area from paint $A_t$ . . . . .	59
4.15	Fractured topologies during the experimental test a. SQ- $\lambda 5-t2$ , b. W1- $\lambda 5-t1.5-A1.6$ , and c. W2- $\lambda 5-t1.5-A0.8$ . . . . .	59
4.16	Main effects plot of the mean of conformability ratio of all the levels of each factor: topology type, . . . . .	60
4.17	Simultaneous 95% confidence intervals comparison of means of the factors a. Length of the unit cell $\lambda$ , and b. Thickness $t$ that belongs to specific Topology and $\lambda$ t(Topology, $\lambda$ ) for the conformability ratio of all the samples tested. If an interval does not contain zero, the corresponding means are significantly different. 62	62
4.18	Topologies with highest conformability ratio in terms of stiffness, grouped by their relative density a. $\bar{\rho} = 0.1$ , b. $\bar{\rho} = 0.28$ . . . . .	63
4.19	Topologies with similar conformability ratio grouped by relative density a. $\bar{\rho} = 0.19$ , b. $\bar{\rho} = 0.29$ . . . . .	63
4.20	Simultaneous 95% confidence intervals comparison of the means of Length of the unit cell $\lambda$ for the Conformability Ratio of square lattice samples tested. If an interval does not contain zero, the corresponding means are significantly different. 64	64

4.21	Simultaneous 95% confidence intervals comparison of means of the factors a. Length of the unit cell $\lambda$ , and b. Thickness $t$ ; and c. The interaction of amplitude and thickness $A*t$ , for the conformability ratio of all the topology W2 samples tested. If an interval does not contain zero, the corresponding means are significantly different. . . . .	66
4.22	Topologies with similar conformability ratio in terms of stiffness grouped in colors by parameters $\lambda$ and $t$ of lattices with topology a. W1, and b. W2. Amplitude $A$ values are identified by different markers. . . . .	67
5.1	Schematic of the voltage divider circuit for data acquisition, FSR is the force sensing resistor (sheet of conductive material). . . . .	70
5.2	Schematic diagram of the data acquisition and storage. . . . .	71
5.3	Experimental setup of the static characterization applying the load $F$ to the velostat. a. Frontal and b. Isometric views. . . . .	72
5.4	Example plot of Voltage and load in terms of time with an applied load of 3N. It is highlighted the fraction sample from which it was obtained the steady state measurement. . . . .	72
5.5	Static characterization data illustrating a. an approximation of a fitted curve to the data and b. the standard deviation of the measurements in each load. . . . .	73
5.6	Measured and simulated model output from transfer function of a. Cycle 1 and b. Cycle 10. . . . .	74
5.7	Amplitude bode plots of Cycles 1 and 10. . . . .	74
5.8	Sinusoidal topologies a. W1, and b. W2; and periodic cut patterns geometries with their parameters c. rotating square with rectangular cuts, d. rectangular perforations, and e. rotating triangle for sensing devices samples. . . . .	76
5.9	Adhesive copper pasted on each node (labeled) for electric measurements. Each node corresponds to a FSR that goes to a voltage divider for data acquisition with an Arudion UNO board and LabVIEW. . . . .	77
5.10	Circuit schematic of the 5 FSRs instrumented in each patterned sensor with its corresponding Arduino pin input. . . . .	77

5.11	Voltage and force in terms of time of tests performed on one of the nodes of the rotating square sensor under different loads: a. 10 N, b. 20 N, and 30 N. It is highlighted on each plot the fraction sample from which it was obtained the steady state measurement average. . . . .	79
5.12	Plots of the steady state electrical resistance measured for each sensor, divided by the load applied a. 10 N, b. 20 N, and c. 30 N. Each sensor is presented by column.	80
5.13	Averaged steady state resistance in terms of load of the five FSRs in each sensor.	81
5.14	Experimental setup of the tensile test: a. Isometric view of the 3D printed clamps to secure the sample, b. Front view and boundary conditions of tensile test, c. Sinusoidal lattice W1 sample mounted on the universal testing machine. . . . .	82
5.15	Experimental setup of the out-of-plane loading test: a. Front view and boundary conditions of tensile test, b. Isometric view of the 3D printed clamps to secure the sample, and c. Sinusoidal lattice W1 sample mounted on the universal testing machine. . . . .	83
5.16	Displacement and resistance response of the sensors of a. Topology W2 and b. Rotating square pattern during tensile loading. Each line corresponds to a FSR and is identified by the position in the sensor. . . . .	84
5.17	Example of the sensors with geometries a. Topology W2 1. before the tensile load, and 2. during the tensile load showing strain on the material; and b. Rotating square, 1. before the tensile load and 2. during the tensile load showing rotation of its hinges. . . . .	85
5.18	Resistance response of the sensors of a. Rotating square, b. Topology W1, c. Rotating triangle, and d. Topology W2 during out-of-plane loading. Each line corresponds to a FSR and is identified by its position. . . . .	86
5.19	Location of the measuring points marked in the artificial residual limb, a. Posterior, b. Lateral and c. Anterior views; and in the sensors' geometries d. Topology W1 and e. Rotating square with their dimensions in cm. . . . .	87
5.20	Location of the measuring points marked in the sensor samples with geometries a. Topology W1, and b. Rotating square. . . . .	88
5.21	Relative resistance in terms of time plots for each run performed with Topology W1 and Rotating square sensors of the simulation of a person standing three times.	89

5.22 Location of the measuring points marked in the sensor samples with geometries  
a. Topology W1, and b. Rotating square. . . . . 90

# List of Tables

2.1	Comparison of fabrication, auxetic structure and properties of the presented wearable sensors . . . . .	20
3.1	Comparison of the type and number of elements to compute $\nu$ . . . . .	36
4.1	Values of the parameters of the sinusoidal lattices samples designed. All units in mm. . . . .	43
4.2	Values of the parameters of square lattice samples. . . . .	44
4.3	Experimental and FEA simulations' results of stiffness . . . . .	54
4.4	Analysis of variance table of the analysis including all the topologies tested.	61
4.5	Analysis of variance table of the analysis of the square lattice samples tests.	64
4.6	Analysis of variance table of the analysis of the topology W1 lattice samples tests. . . . .	64
4.7	Analysis of variance table of the analysis of the topology W2 lattice samples tests. . . . .	65
5.1	Dimensions of the periodic cut samples . . . . .	75

# Contents

<b>Abstract</b>	<b>5</b>
<b>List of Figures</b>	<b>14</b>
<b>List of Tables</b>	<b>15</b>
<b>1 Introduction</b>	<b>1</b>
1.1 Additively manufactured auxetic metamaterials . . . . .	1
1.2 Auxetic metamaterials in biomedical engineering . . . . .	3
1.3 Motivation of the study . . . . .	5
1.4 Aims and objectives . . . . .	6
1.5 Thesis outline . . . . .	6
<b>2 State of the art</b>	<b>8</b>
2.1 Carbon loaded films implemented in pressure sensors in wearables . . . . .	9
2.2 Auxetic structures implemented in wearables . . . . .	10
2.2.1 Re-entrant auxetic structures . . . . .	10
2.2.2 Auxetic structures based on rotating unit mechanisms . . . . .	12
2.2.3 Auxetic structures with chirality and a-chirality . . . . .	13
2.2.4 Auxetic structures conformed with sinusoids . . . . .	13
2.3 Materials and fabrication methods of auxetic sensors . . . . .	14
2.3.1 Conductive materials deposited on flexible materials . . . . .	15
2.3.2 Sensors fabricated using Additive Manufacturing . . . . .	16

2.4	Mechanical characteristics for auxetic wearable products . . . . .	17
2.5	Electric properties in auxetic sensors . . . . .	19
2.6	Summary . . . . .	24
<b>3</b>	<b>Sinusoid lattice patterns: design, parametrization, and in-plane mechanical properties</b>	<b>26</b>
3.1	Sinusoid lattice parameterization and computational modeling . . . . .	26
3.1.1	Sinusoid lattice curves parameterization . . . . .	27
3.1.2	Computational modeling of samples . . . . .	29
3.1.3	Relative density . . . . .	29
3.2	Computational characterization of the role of sine geometry on the Poisson's ratio . . . . .	31
3.2.1	Sinusoidal topologies designed with different combinations of parameters . . . . .	32
3.2.2	Type of finite elements comparison for the numerical characterization of the $\nu$ . . . . .	33
3.2.3	Results and discussion of computational characterization of Poisson's ratio . . . . .	36
3.3	Summary . . . . .	40
<b>4</b>	<b>Out-of-plane mechanical properties of 3D printed samples and conformability tests</b>	<b>42</b>
4.1	Finite Element Analysis and experimental study of out-of-plane stiffness of sinusoidal lattices . . . . .	42
4.1.1	Additive manufacturing of samples and experimental setup description of out-of-plane stiffness evaluation . . . . .	43
4.1.2	Finite element analysis simulations to evaluate stiffness . . . . .	46
4.1.3	Stiffness numerical results . . . . .	47
4.1.4	Contrast of numerical results with experimental tests . . . . .	50
4.2	Conformability characterization via out-of-plane loading and digital image processing . . . . .	56



4.2.1	Digital image processing methodology for conformability characterization . . . . .	56
4.2.2	Experimental results and statistical analysis of conformability ratio . . . . .	59
4.3	Summary . . . . .	66
<b>5</b>	<b>Auxetic pressure sensor: fabrication and electric response under mechanical loading</b>	<b>69</b>
5.1	Electric characterization of velostat . . . . .	70
5.1.1	Instrumentation and data acquisition . . . . .	70
5.1.2	Electric static characterization of velostat . . . . .	71
5.1.3	Electric dynamic characterization of velostat . . . . .	73
5.2	Fabrication of sensing samples: geometries and instrumentation . . . . .	75
5.2.1	Auxetic cut patterns geometries . . . . .	75
5.2.2	Instrumentation . . . . .	76
5.3	Static measurement of electric resistance with varying loads of velostat based sensors . . . . .	78
5.3.1	Experimental setup and data acquisition . . . . .	78
5.3.2	Results and discussion of the steady state electric resistance measurements . . . . .	78
5.4	Response of velostat based sensors under tension and out-of-plane loading	81
5.4.1	Boundary conditions and experimental setup . . . . .	81
5.4.2	Electric resistance results and discussion of sensors subjected to tension and out-of-plane loading . . . . .	83
5.5	Auxetic patterned sensors evaluated in-socket . . . . .	85
5.5.1	Experiment description . . . . .	86
5.5.2	Results and discussion of in-socket evaluation tests . . . . .	88
5.6	Summary . . . . .	90
<b>6</b>	<b>Conclusions and future work</b>	<b>92</b>
6.1	General conclusions . . . . .	92
6.2	Future work . . . . .	94

<b>A Sine topologies generator</b>	<b>96</b>
<b>Bibliography</b>	<b>111</b>

# Chapter 1

## Introduction

In recent times, the use of wearable products has dramatically grown because of its great potential in biomedical devices and soft robotic applications. Wearable sensors can convert physical variables such as motion, pressure or temperature, into electronic signals. Simultaneously, they should be able to conform to the target's surface and undergo large amounts of strain without loss in performance. One application in biomedical engineering has been in-socket pressure sensors. A biomedical device for this application needs to withstand repeated large deformations, and conform to the complex, curved geometry of the patient's residual limb. Conformability presents a challenge in materials science and engineering. One approach to improve it has been the implementation of auxetic topologies, which have inspired the present work. The motivation and the objectives of the research are presented in this chapter.

### 1.1 Additively manufactured auxetic metamaterials

A metamaterial is a type of material whose properties are not inherent only from the material from which is made, but also from its internal structuring. They can be tailored to present unusual mechanical properties such as elastic modulus, density, energy absorption, acoustic performance and negative Poisson's ratio [39]. The latter, are known as auxetic

and characterizes a materials property to expand or contract in the direction perpendicular to the load [39]. This is further explained with a material subjected to tension (figure 1.1). Conventionally, when stretched in one direction, materials become thinner in the the transverse direction of the load (figure 1.1a). On the contrary, auxetic materials expand in the transverse direction (figure 1.1b).

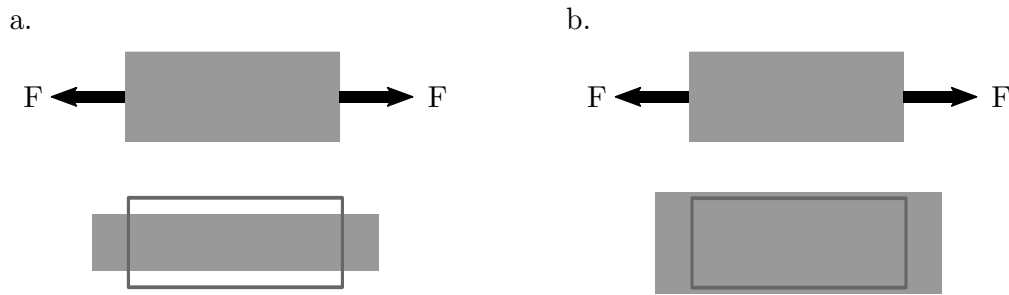


Figure 1.1: Material under tension with Poisson's ratio a. Positive, and b. Negative

The uncommon deformation accompanies metamaterials with desirable properties, such as an increase of the shear modulus, fracture toughness, high acoustic damping, indentation resistance, and synclastic behavior [9]. This last, refers to a material demonstrating a dome shape (illustrated in figure 1.2b.) when subjecting an out-of-plane bending moment. Conventional materials exhibit a saddle shape (figure 1.2a.). Synclasticity makes auxetic metamaterials potential candidates for applications in aerospace, automotive, biomedical, military, smart sensors and textiles [39].

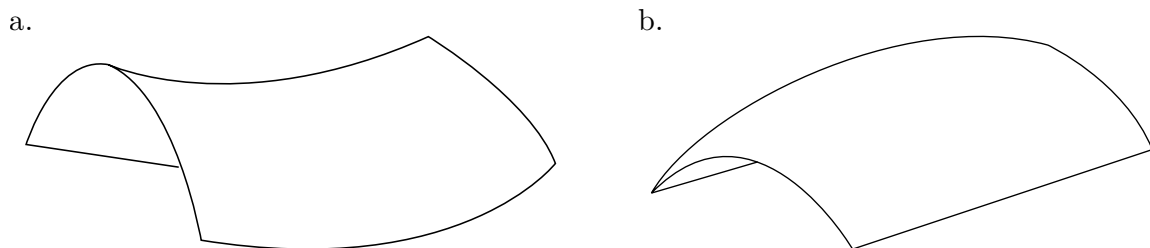


Figure 1.2: Types of behavior of materials subjected to out-of-plane bending moment exhibiting a. Anticlastic (saddle shape) and b. Synclastic (dome shape).

Finite element modelling (FEM) has been a key element to move forward on the study of auxetic structures. The effect of changing design parameters and the outcome

of their plastic deformation can be predicted. Enabling to save numerous iterations of manufacturing and testing, so that design changes are validated to tune desired mechanical properties [10]. The fabrication of auxetic metamaterials has been investigated with various additive manufacturing (AM) techniques as the same computational models used for FEM can be used for fabricating purposes. AM creates 3D models by adding layer by layer, there are several techniques such as:

- Stereolithography (SLA): ultraviolet laser is aimed onto the surface of liquid resin in the desired places to build a product. The election of materials is limited to light-sensitive polymers but gives better surface finish [17].
- Selective laser sintering (SLS): sintering of material in the form of powder is accomplished with the application of a laser beam [17].
- Fused deposition modelling (FDM): a heated thermoplastic material is extruded through a nozzle layer by layer [17].

Although AM enables to print almost any design, considering the manufacturing procedure, mass production is not feasible. The cost of manufacturing is still too high and more research is needed to implement these materials with superior properties into real applications [39].

## 1.2 Auxetic metamaterials in biomedical engineering

Because of the counter-intuitive behavior of auxetic materials, they have been used for several applications in sports, textiles, biomedical engineering and smart sensors. There are several types of biomedical sensors. One of them are mechanical sensors, which have the potential to be used in rehabilitation and prosthesis. They track the physical activity of the human body and provide useful information about health. This can lead to detection of abnormal patterns that are precursors of various diseases [47]. They are categorized as stretchable strain sensors and pressure or tactile sensors. The former detect motion through quantifying mechanical deformation and are implemented in pulse monitoring, tracking respiration and bending of joints. Pressure sensors demand high flexibility and

stretchability, they should be fully functional while withstanding strong mechanical forces [23]. Parameters needed to be monitored depending on the application are [42]:

- Sensitivity: measures the capability of a sensor to transduce pressure.
- Linearity: range to which the sensor behaves linearly.
- Limit of detection: smallest pressure that the sensor can distinguish.
- Hysteresis: incapability of a sensor to return to its original state when the load is removed. Low hysteresis is desirable so that the performance is reproducible.
- Response time: time from the instant that the load is applied until reaching 90% of a stable output.
- Recovery or relaxation time: time to recover its initial state once the load is removed.
- Endurance or stability: number of loading and unloading cycles without significant difference in its output.

These sensors are available in several types of transducers, some of them are piezoelectric, piezocapacitive and piezoresistive. Piezoelectric sensors produce electrical charges under mechanical stress, weight or strain. Piezocapacitive are usually fabricated using two parallel plates that act as an electrode with an interlayer sandwiched acting as a dielectric. The capacitance depends on the interlayer, separation between the two plates and the electrode area [47]. The piezoresistive transducers consist on conductive material that changes its electrical resistance when exposed to mechanical deformation. Their high sensitivity, adaptability, stretchability and low hysteresis make them adequate for biomedical sensors [47].

Research and commercialization of these sensors has increased recently, along with the smart adaptation of mechanical and electrical methods of measuring the body. This adaptation has involved innovations in how to make them conformal and flexible. However, challenges still demand significant improvements that can be met by understanding the features of the skin [15]. Because of the negative Poisson's ratio, auxetic structures

could match the deformation of the skin and provide stable performance in varied environments [22]. This has paved the way to research the implementation of auxetic topologies into sensors with improved characteristics. An example is a stretchable strain sensor with 24-fold improvement of sensitivity, which could stretch up to 98% [18]. Another is a 3D printed auxetic strain sensor with improved is the operational range [53].

Apart from sensors, there have been explored other applications in biomedical engineering such as the development of prosthesis liners [50], the design of orthopedic bone plates fabricated with AM [49], in medical bandages [34] and auxetic bone screws [55]. Currently efforts are being made to produce the next generation of sensors by integrating auxetic materials [22].

### 1.3 Motivation of the study

The use of biomedical wearable devices has become relevant in the detection of many pathologies [5]. Some of them include plantar pressure sensors for detecting abnormalities in running, jumping or walking [5], and systems to assess sitting posture, which are important to detect asymmetry that may lead to musculoskeletal pain, low back pain and spinal deformity. Other application of these devices are in-socket sensors that map the pressure distribution inside prosthetic sockets for their design. This reduces the incidence of skin irritation, ulcers or tissue breakdown caused by a poor fitting of the residual limb-socket interface [2].

As previously stated, conformability becomes especially important for these and has been difficult to achieve [54]. A motivation for the present work arises from the challenge that conformability in this type of devices represents and the great potential of auxetic materials to solve it. Most applications still remain in their infancy and require more exploration of auxetics to take projects from the stage of laboratory study into the implementation of real applications. Moreover, most researchers have focused on the study of auxetic behavior either in compression or tension [39], and studies involving more complex loading conditions could be very useful for biomedical applications.

## 1.4 Aims and objectives

This dissertation is concerned with the mechanical properties and electric response of auxetic lattice topologies to evaluate its potential use in wearable products. The majority of literature has been focused on the in-plane mechanical properties of lattices implemented in wearables, however studies on out-of-plane properties and conformability evaluations are scarce.

With the aim of filling this gap, the objective of the present work is to establish a structure-property relation of a lattice biomedical sensor, between its lattice topology, its ability to conform and its electric response; in order to improve its conformability to complex-curved geometries. The main objectives are:

1. To establish a relation between the geometrical parameters of sine-based topologies, their relative density and auxeticity, by finite element modeling simulations of tensile loading. stiffness and conformability by finite element modeling simulations of lattice
2. To obtain the lattice topologies' out-of-plane mechanical properties and compare it with 3D printed samples evaluated experimentally to establish a relation between their geometrical parameters and mechanical behavior.
3. To implement lattice topologies into an electro-conductive material to fabricate pressure-measuring devices with the aim to evaluate their electric response under tensile and out-of-plane loading.
4. To compare the lattice sensor samples with other periodic pattern topologies and evaluate their mechanical and electric response and implement the fabricated sensing samples as in-socket sensors.

## 1.5 Thesis outline

This document is organised into 6 chapters. A general introduction to all the areas involved is given in Chapter 1. A review of the literature in different areas including the



---

implementations of auxetic structures in wearable products and their characteristics is presented in Chapter 2. The description of sinusoid based topologies, their parameterization, computational modeling and characterization of their relative density and Poisson's ratio are described in Chapter 3. Their out-of-plane loading response and conformability tests are described in Chapter 4. The fabrication method and instrumentation of pressure sensing samples, along with their static characterization, results of the mechanical loadings and evaluation as in-socket pressure devices are presented in Chapter 5. Finally, the conclusions and future work derived from the outcomes of the present work are summarised in Chapter 6.

# Chapter 2

## State of the art

As mentioned before, wearable sensors must be able to convert physical variables into electronic signals, simultaneous to conform to a target surface (skin). This translates to sensors that endure large amounts of strain without loss in performance. One of the main challenges in materials science and engineering has been conformability. Most devices are made of hard materials or are hybrids consisting of hard and soft materials. While hard materials offer durability, fast response time, and overall device performance superior to soft materials; soft materials tend to fail when a great strain is applied [54]. There has been a lot of approaches and techniques, regarding methods of fabrication, materials employed, and structural changes to materials to overcome this challenge, reviewed in this chapter.

The review of the literature is distributed in sections as follows. In section 2.1 the novel carbon loaded films implementations as pressure sensors is covered. In section 2.2, structural changes to materials wearable products are reviewed. In section 2.3, the fabrication methods employed for each product. In section 2.4 the mechanical properties in wearable products are reviewed. Finally, in section 2.5, the electric properties of auxetic sensors will be summarized.

## 2.1 Carbon loaded films implemented in pressure sensors in wearables

Pressure measuring is a popular application of wearable sensors. They have been explored in different applications such as human movement monitoring, control of pressure, re-distributing insoles, sitting posture monitoring, quantification of hand forces and others. Among other factors, these devices must also be comfortable, and the transducer mounting should be easy and quick [16]. The most common pressure sensors are capacitive, piezoelectric and piezoresistive.

Piezoresistive sensors have been made commercially available through manufacturers in the form of force sensitive resistors (FSRs) [16]. These sensors are thin and small, ideal for measurements of the pressure inside reduced spaces. A biomedical application of these has been as estimators of pressure inside sockets of prosthetic limbs [43][1]. Still, conformability to the limb is an issue because of the irregular shape of the limb.

One approach to improve it has been the implementation of novel materials, such as graphene-based film [29], and RTV-silicone combined with milled carbon fibers [41]. A low-cost conductive material that is commercially available is the carbon-loaded film, also called Velostat. Hopkins et al. [16], produced a thin sensing device for use within lower limb prosthetic to quantify pressure using this material. The structure of the sensor consisted of a core using a circular piece of the conductive film and two circuitry layers sandwiching it. The implementation in the interior of a socket consisted of 12 sensor strips arranged 2 cm apart forming a circle-like pattern. The results showed that this sensor advantages related to low-cost and ease of integration. However, this device had many disadvantages in time, and complexity of calibration; since the device consisted of 12 individual sensors to monitor a single socket. It was stated that it could be possible to model many of the effects of factors (drift, cyclic drift, and thermal response) which could not be done for this design, since it had to be done for each sensor.

Anwary et al. [4] used this material to assess sitting posture, Ramya et al. [38] and Bello Ruiz [5] used it to foot pressure monitoring, Vedant et al. [48] to develop a device to assess finger engagement during manual assembly operations. All three devices implemented a multi-layer architecture to obtain a flexible sensor. The piezoresistive material

was sandwiched between two layers of copper, then covered with a plastic material to protect it. To obtain the signal, they used a voltage divider. The results they obtained were successful to their application, stating the potential of the carbon-loaded film in different configurations to develop a wearable device. Despite of the advances in calibration and characterization of the sensors, there is still room for improvement in accuracy [46]. Apart from carbon-loaded films, other materials combined with an introduction of an ordered arrangement to these have been explored to improve conformability.

## 2.2 Auxetic structures implemented in wearables

The use of architectural materials such as periodic cellular lattice structures can have a beneficial effect obtained from the porosity created [9]. In this section the auxetic cellular lattices found implemented in wearables are introduced. As mentioned in chapter 1, an auxetic structure is identified by its negative Poisson's ratio  $\nu$ . This property give materials many advantages in comparison to conventional ones, such as an increase of the shear modulus, fracture toughness, high acoustic damping, indentation resistance, and synclastic behavior. Therefore, the use of materials adopting periodic cellular lattice structures with auxetic elastic behavior is promising solution in the design of sensors [9].

Auxetics are the preferred design for wearable products. The human skin expands biaxially during bending, exhalation, and muscle tension - negative Poisson's ratio [23]. Hence it is patent to employ auxetics in such applications. Their geometry and deformation mechanism play a central role in the design of diverse applications, because from this depends The degree of auxetic behavior and the related material properties [7]. Therefore, two-dimensional auxetic topologies implemented in wearable devices are reviewed next.

### 2.2.1 Re-entrant auxetic structures

The most common type of auxetic materials are re-entrant auxetic structures, some examples can be found in figure 2.1. They are formed by truss-type structures that are composed of thin ribs and linking hinges. The unit cells of these structures are commonly folded inside the unit cells and the re-entrant sides and vertices form an important structural motif

of the re-entrant structures [7].

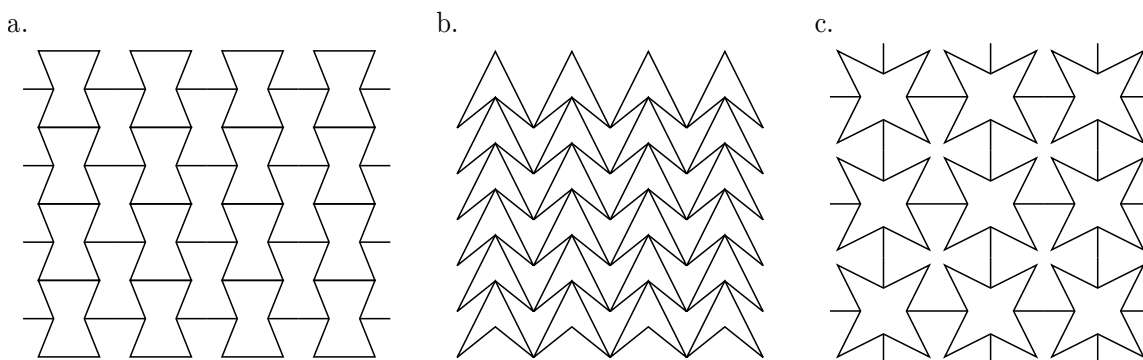


Figure 2.1: Examples of re-entrant auxetic structures: a. bowtie honeycomb, b. triangular re-entrant, and c. re-entrant star structure.

This type of structures have been used for a variety of applications, starting with 3D printed fashion items with the triangular re-entrant [44] (figure 2.2a) and the bowtie honeycomb [33] (figure 2.2b), achieving flexibility with a wide variety of inflexible materials, using less material while being able to convert any arbitrary topology into a desired structure ready to be fabricated. Because of its anisotropic characteristic (stiffer in one direction than the other), the bow-tie geometry was proved to be eligible for a cardiac patch for the treatment of myocardial infarction [21](figure 2.2c), it was achieved to tune its mechanical properties to match those of native heart tissue while maintaining the bulk properties of the material, being able to stretch and conform to match its movements.

This topology has also been used in the design of sensors, starting with a highly stretchable piezoresistive body-mounted sensor with potential applications such as gesture recognition, pulse wave and breathing monitoring [32] (figure 2.2e). Next, Jiang et al. [18] implemented this topology to enhance sensitivity of a stretchable strain sensor, which was successful to attach to a human wrist, and achieving good cyclic durability (figure 2.2f). Similarly, Wong et al. [53], and Lai and Yu [27] were able to use 3D printing of hydrogels to obtain a stretchable strain sensors (figure 2.2h and d), apart from high stretchability, the porous structure also brings high breathability for human skin. Liu et al. [30], used the two-dimensional bowtie honeycomb as one of the designs of textured soft strain gauges for monitoring animal skin, which outperformed the other patterns in obtaining the highest

decrease in maximum stress showed by animal skin. Another type of sensor tested have been touch sensors, Lee et al. [28] used this topology in a graphene-based wearable touch sensor (figure 2.2g), which provided stable electrical properties and wearable capability on skin, even with mechanical stretching.

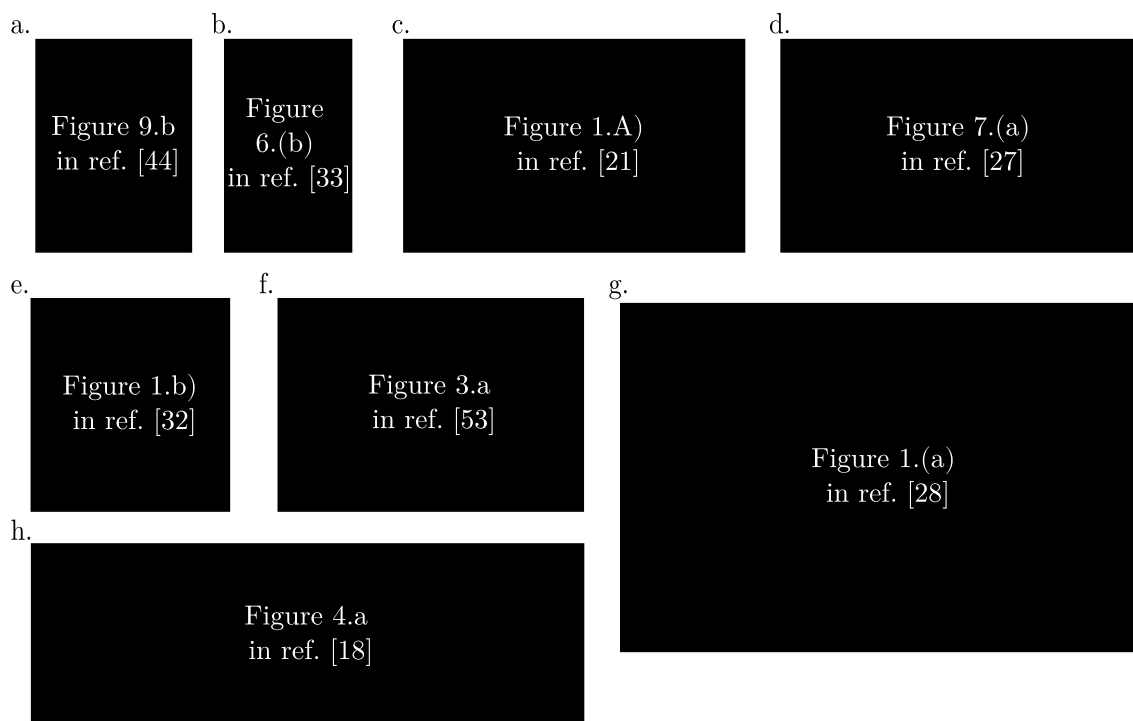


Figure 2.2: Re-entrant structures in applications: fashion items using the a. triangular re-entrant [44] and b. the bowtie honeycomb [33]; c. cardiac patch for the treatment of myocardial infarction [21]; d. 3D printed ionogel strain sensor [27], e. Piezoresistive hybrid sensor [32], f. Stretchable strain sensor [53], g. Graphene-based stretchable/wearable touch sensor [28], and h. 3D printed hydrogel strain sensor [18].

## 2.2.2 Auxetic structures based on rotating unit mechanisms

This mechanism consists of rigid units connected by smooth hinges, some examples can be found in figure 2.3. Rigid units are arranged slightly tilted in a clockwise or counter-clockwise direction, opposite to the tilting direction of the nearby units. There are several types, like the square rotating unit (figure 2.3a), and the rotating triangle (figure 2.3b).

The square rotating unit has been implemented to design bandage substrate films with great conformability (figure 2.3c) [51], and a force sensor for hand rehabilitation (figure 2.3d) [24] successfully attached to the wrist.

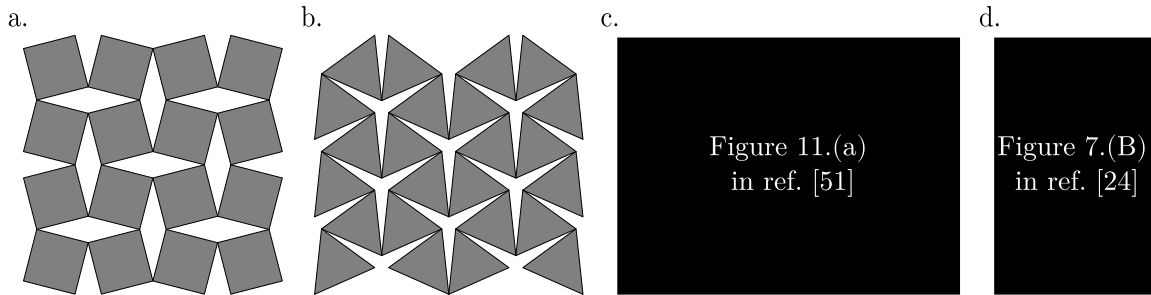


Figure 2.3: Rotating unit mechanisms a. Square and b. Triangle; and examples of applications: c. Bandage substrate film for elbows [51], and d. Force sensor film for hand rehabilitation [24].

### 2.2.3 Auxetic structures with chirality and a-chirality

These type of structures are formed by unit circles of chiral structures (its mirror image cannot be superposed in any combination of rotations) uniformly arranged in tri-, tetra- (figure 2.4a) or hexa-tessellation (figure 2.4b), and ribs chirally wrap around the circular units that link one circle to another. The mechanism that makes this structure behave as auxetic, consists of load transferred from an arranged chiral structure to the circular unit through chiral ribs. This transferred load is deflected from the center of the circle which generates a rotational torque [7]. De Bellis and Bacigalupo [9] implemented periodic cellular lattice structures in the form of anti-tetrachiral structures (figure 2.4c) to a piezoelectric strain sensor (figure 2.4d).

### 2.2.4 Auxetic structures conformed with sinusoids

These structures come from the combination of sinusoidal waves along two directions, given a specific combination of parameters, patterns with auxetic properties can be obtained. One of this patterns has been used to apply 3D printing textiles to safety protective clothing for elbows and knees [19] achieving a decreasing in load and elongation when

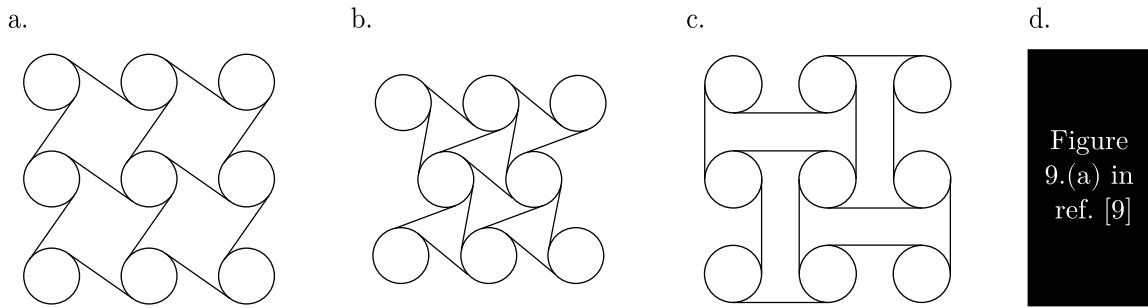


Figure 2.4: a. tetrachiral, b. hexachiral, and c. anti-tetrachiral auxetic structures; and d. Piezoelectric strain sensor diagram in the form of anti-tetrachiral structures [9].

fabricating samples with shape memory thermoplastic polyurethane (figure 2.5a). Also, as a 3D printed capacitive sensor mounted onto a universal jamming gripper (which has a deforming surface membrane, challenging for planar sensors to detect normal forces under elongation conditions) to measure gripping forces and identification of object shapes (figure 2.5c); and a human joint (figure 2.5d), enhancing surface conformability to diverse soft robotic surface morphological deformations and human joint surfaces [56], although no quantitative information of conformability was showed.

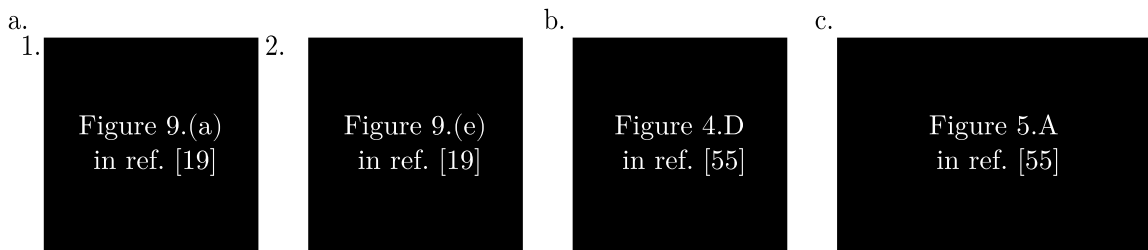


Figure 2.5: a. Sinusoidal pattern implemented as a. 3D printed clothing for curved objects [19], and a capacitive sensor mounted onto b. Universal jamming gripper, and c. Human elbow[56].

## 2.3 Materials and fabrication methods of auxetic sensors

Achieving a reliable performance in auxetic sensors strongly depend on the fabrication method used for their manufacturing. Consequently, ongoing search for new materials



that reach the required mechanical attributes through structural designs has demanded for new fabrication methods of complex geometries for laboratory research and commercial products [53]. In the last decade there has been progress in the use of low-cost flexible materials, such as polymers, paper, fabrics and cellulose nanofibers as templates for depositing metals or using carbon-based conductive inks (e.g. carbon nanotubes and graphene) as electrodes [53]. A drawback of this technique is the delamination or crack formation at large strains.

Additionally, additive manufacturing (AM) has been explored to produce fabric-like geometries, such as thin, continuous lattice structures [37]. AM became highly attractive because of its potential to match the complex form and mechanics of human bodies. Therefore, compared to other fabrication methods, is well-suited to production of wearable devices that offer enhanced fit. A solution for delamination, as well as the fabrication methods and materials used for both processes are presented.

### **2.3.1 Conductive materials deposited on flexible materials**

One solution for delamination has been the implementation of auxetic structures to soft materials, by making the material more stretchable. Ko et al. [24] designed and fabricated an auxetic stretchable force sensor for hand rehabilitation with microfiber sheets coated with gold particles to make them conductive. The microfiber sheets were fabricated using poly ( $\epsilon$ -caprolactone) (PCL), one of the most used synthetic polymers for biomedical engineering applications. The resin was deposited by a custom-made electrospinning apparatus with a computer numerical controlled (CNC) machine. To make a comparison between auxetic structured sheets and solid ones, some microfiber sheets were cut to fabricate the auxetic structures using a laser-machining system. Finally, all the sheets were coated with gold for the electrical current resistance tests.

Similar approaches of depositing a conductive material on thin films were tested by Kim et al. [23] and Jiang et al. [18]. The first used elastomer thin films spray-coated with Ag suspension to fabricate their stain-sensitive electrocardiogram (ECG) electrodes on a hygroscopic serpentine network structure, which resulted to have auxetic behavior. On the other hand, Jian et al. composed a sensor using conductive single-wall carbon

nanotube (SWCNT) network on polydimethylsiloxane (PDMS) thin film, with a PDMS auxetic frame. The PDMS thin film was fabricated by employing 3D printing-assisted molding, in conjunction with SWCNT self-pinning method to deposit the conductive material over the film. It is worth mentioning that neither presented delamination.

### **2.3.2 Sensors fabricated using Additive Manufacturing**

Additive manufacturing (AM) is a process that enables the rapid fabrication and iteration of complex geometries. Pattinson et al. [37] tailored a mesh of thermoplastic elastomer using fused deposition modeling (FDM). The mesh was directly printed using a continuous toolpath. This step is important for the mesh performance because interruptions of the toolpath could lead to defects that can compromise strength. Similarly, Yeong et al. [56] used this method to fabricate a capacitive sensor by printing carbon black thermoplastic polyurethane (PI-ETPU) electrodes insulated with thermoplastic polyurethane (TPU)

Wong et al. [53] also 3D printed a device, but using photolithography, instead of FDM. Some conductive structures with varied geometries were printed using ionogels. Ionogels are an emerging class of soft materials that exhibit ionic conductivity and thermal stability without the need to replenish ions or the addition of conductive particle fillers. First, the ionogel was synthesized using a polymer, then the patterns were printed using photolithography. Finally, a film that could be used as a sensor to detect stretching and twisting mechanical movements was successfully produced.

Apart from the advantages of using additive manufacturing, with respect to complex design, the fabrication of an auxetic material consumes less material when comparing it with the fabrication of solid sheets [53]. Other advantages in relation to physical and mechanical properties obtained by the implementation of auxetic structures are reviewed in the next sections.

## 2.4 Mechanical characteristics for auxetic wearable products

A stretchable sensor to be successfully employed, must achieve specific mechanical properties. Some of them are high stretchability, cyclic durability, and conformability, i.e. high mechanical compliance to the target surface. It becomes very challenging obtaining this properties and producing devices that replicate the mechanics of soft tissues, because they often have nonlinear tensile stress-strain responses. Moreover, this varies significantly according to the tissue type and can be different for individual patients according to their body type and health condition [37].

Auxetics, as reviewed in Section 2.2, can be endowed with extraordinary mechanical behaviors. This knowledge has been exploited for the development of stretchable devices. In the first approach of implementing auxetic structures to a strain sensor done by Ko et al. [24] these properties were tested by making a comparison of two sheets of microfiber, an Auxetic Microfiber Sheet (AMS) and a nonauxetic Microfiber Sheet (MS). Results showed that the AMS could be firmly attached on human skin because it had higher elasticity and larger strain than the MS. Correspondingly, the AMS sample could be stretched with a 10-fold smaller tensile force and presented linearity in tension and extension and its maximum strain was almost four times higher than the MS sample.

In a similar way, there have been obtained other highly stretchable devices, and, even when presented with small defects from the fabrication process, which limits stretchability, did not prevented to fulfill the required for skin-mounted wearable devices [18]. In other study, an auxetic strain sensor could be stretched further by over twice the distance, producing increased operational range, when compared to a nonauxetic film with the same outer dimensions [53].

Cyclic durability of auxetic strain sensors has also been tested, where an auxetic structured sensor were subjected to multiple stretching cycles at specific stretching distances, which exhibited good cyclic durability of 2000 consecutive loading and unloading cycles [18]. Other test demonstrated resilience of a thermoplastic wearable device with no perceptible change in the tensile response in over 1800 cycles [37].

Other mechanical property improved by the auxetic structure, is the mimic of the

nonlinear tensile response of soft tissue [37] and the minimization of local stress concentration at some regions [54]. The latest allowed the formation of complex curved structures on a flat sheet without stretching or shearing. And, since stretching occurred by unit rotation rather than deformation, the material in the structure was nearly strain-free. Getting to the conclusion that, by introducing an auxetic structure, any flat non-stretchable material can be transformed into a stretchable and conformable material with a wide range of desired shapes and patterns [54].

Moreover, out-of-plane stiffness has been evaluated apart, since it has been proven that is not the same as in-plane behavior and the equivalent in-plane elastic modulus cannot be used to characterize their deformation [6]. For instance, it was found that the anti-trichiral structure displays negative Poisson's ratio under uniaxial in-plane loading, but turned out not-auxetic in out-of-plane bending [3]. Research in this field is scarce [8] and only some structures have been studied. Related to this it was found in thin shells that auxeticity provides more flexibility than conventional lattices [52][31]. Furthermore, 3D printed auxetic sinusoidal thin shells could withstand higher strains, and, dependant to their degree of auxeticity, delay fracture or even avoid it [31]. Other studies have found relations between the geometrical parameters of the structures and their out-of-plane behavior. For instance, increasing relative density in chiral structures also increased their stiffness, this was proved by thickening and shortening its ligaments. [45]. Also, in bowtie honeycomb and triangular re-entrant 3D printed lattices, their internal angle was found to be proportional to stiffness [8].

Auxetics have also been compared along other types of structures on their ability to conform. Comparison of their synclastic behavior has proven that auxetics can produce curvature adaptive structures to generate complex bending shells [35], even with rigid materials [36], and that they can easily accommodate to the human body [8]. Along this line of study, computational optimizations have been done to produce topologies with a controlled deployment onto specific curved surfaces from flat auxetics design [26] [11] [40], even achieving double-curved shapes using multi-layered auxetic structures [12]. More specific for wearables, non-uniform auxetic topologies have been design for highly-stretched joint areas, matching the deformation behavior of the target skin, showing higher conformability than conventional uniform auxetic topologies [14][51][56]. Apart from the

mechanical properties affected by the implementation of auxetic structures into devices, it also has changes in its electric properties, described in the next section.

## 2.5 Electric properties in auxetic sensors

For a sensor to be successfully implemented as wearable devices there are other characteristics that it must be able to fulfill. Wearable sensors should be able to detect mechanical, electrical, or chemical signals from the body or sense external stimulations like pressure, strain and torque. One of the most important characteristics is sensitivity, since this allows a wide range of measurement to the sensor. Sensitivity is affected by the auxetic structuration of a material. This property is the responsible to allow the precise detection of movements, even the smallest ones, and is critical in devices designed for health monitoring, since they must be able to provide sufficient information for accurate diagnosis or analysis [18]. The challenge is to achieve high sensitivity under large strain.

To solve it, most of the research focused on changing and optimizing active materials, however, achievable sensitivity still remains limited. In conventional strain sensors, when a stretched elastomer expands in the longitudinal direction and compresses transversely, active materials are separated, this effect is contributed to sensitivity. On the other hand, compression squeezes active materials together, thus limiting the sensitivity. Then, establishing the relation between structure and sensitivity [18]. De Bellis and Bacigalupo [9] added to the comparison of the solid and auxetic sensor, a nonauxetic latticed structure. It was found that the strain sensor with auxetic microstructures was more sensitive than the nonauxetic latticed strain sensor, and this last was more sensitive than the solid film.

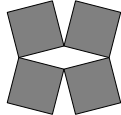
This type of structures can be tailored to enhance some properties yet maintain others we do not want modified as the case of resistance. As an example, Ko's et al. [24] force sensors (solid films and auxetic films) demonstrated similar results with respect to the change of resistance measured. However, when testing its resistance on human skin it showed a more linear response, this electric response is beneficial since the characterization of the device becomes easier. Kim's et al. [23] electrocardiogram (ECG) showed a similar behavior in addition stability under deformation, without the increase in the signal-to-noise ratio. Wong et al. [53] found that another advantage of using auxetic structures is

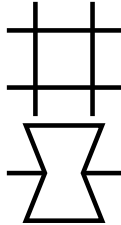
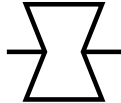
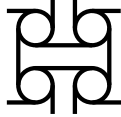

that this type of sensors remained conductive at certain points and could still provide current readings in response to strain after multiple failure points, while the bulk film stopped current readings immediate after failure.

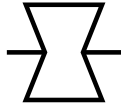
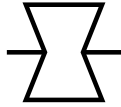
Moreover, the use of an auxetic structure on a non-electro-conductive material could enable the fabrication of a sensor by placing conventional hard devices (e.g., batteries, circuits, LEDs, etc.) without sacrificing device performance during large deformation [54]. In a comparable way, strain and force sensors are not the only wearable devices, there are other type of popular sensors, like pressure sensors, for which auxetic structures have not been implemented.

A summary of all the sensors presented is made in Table 2.1, with the characteristics of each one.



Table 2.1: Comparison of fabrication, auxetic structure and properties of the presented wearable sensors


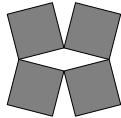
<b>Type of sensor</b>	<b>Fabrication method</b>	<b>Material Structure</b>	<b>Physical and mechanical properties</b>	<b>Electric Properties</b>
Stretchable force sensor for hand rehabilitation [24]	PCL film cut with laser-machining, coated with gold particles		High elasticity, can be stretched with a small tensile force, linear behavior of flexion and extension	Accurate measures of force and strain, low hysteresis, and high sensitivity

Capacitive touch sensor for wearable electronics [20]	Graphene electrodes onto PET substrate		Thin and stretchable, conformal to highly deformable human body parts. Minimized mechanical failure	Good pressure sensing properties, capacitance affected by changes in body temperature
Piezoresistive hybrid sensor for body-mounted biomedical applications [32]	Sensor fiber mounted on 3D printed TPE auxetic		Comfortable to wear around the wrist	Able to fulfill different sensing applications: gesture recognition, pulse wave monitoring and breathing.
Piezoelectric strain sensor [9]	-		Increased shear modulus, fracture toughness, indentation resistance	Improved sensitivity and piezoelectric behavior
Stretchable strain sensor [18]	3D printed PDMS film, deposited on conductive SWCNT		High stretchability, good cyclic durability	Elevated sensitivity

ECG on-skin sensor [23]	Elastomer films spray-coated with conductive Ag suspension over a serpentine network of hygroscopic gel	Not-specified auxetic	Conformal contact with skin under large body motions, breathability, ultralight and imperceptible in wearing, no delamination	Stability under deformation and during wetting, without increase in signal-to-noise ratio
Strain sensor [53]	3D Printed ionogel		Light weight and increased extensibility and operational range	Increased sensitivity, operational range and conductivity after multiple failure points
Touch sensor [28]	Graphene electrode		High stretchability, conformable to the human hand palm	Stable operation under severe deformation



Strain sensor [27]	3D printed ionogel		Conformal contact with the skin during large deformations	Able to identify body motions, steady response of relative resistance after 100 tensile test cycles, more sensitive than non-auxetic geometries
Strain sensor to monitor animal skin [30]	Soft elastomeric capacitor with textured surface		Tensile stresses significantly reduced with textures, decreasing the normal stress experienced by the skin	Auxetic patterns increase sensitivity
In-socket pressure sensor [16]	Carbon loaded film for the core, sandwiched between two circuitry layers	Non-auxetic strips arranged in circle	Not evaluated	Poor accuracy, complexity in calibration

Capacitive sensing array [56]	3D printing of carbon TPU electrodes on conventional TPU		Compliance and conformability to adhered curved-expanding surfaces	Stability under uniaxial stretch
Temperature sensor to monitor wound infections [51]	Temperature sensor installed on an auxetic flexible substrate bandage		Enhanced conformability and adhesion compared to a uniform auxetic and solid sample	Not evaluated

## 2.6 Summary

The great potential and benefits of implementing auxetic structures to a variety of materials in wearable products has been proved. It provides a new perspective to explore a wide variety of materials and fabrication techniques into stretchable electronics. Specially reviewing the benefits of the synclastic behavior, product of negative Poisson's ratio, which allows to produce curvature adaptive structures, even in rigid materials, and can easily conform to the human body. Moreover, auxetics bring many advantages in terms of electrical performance, such as enhanced sensitivity in strain sensors, and reduction of strain produced in the skin. Additionally, by replacing flexible with architected rigid materials could solve other electric performance problems, such as stability, accuracy, and linearity.

It is also brought to the attention the need to extend the study of the effect of the geometrical parameters onto the mechanical behavior of other structures different from the bowtie honeycomb. And, since out-of-plane behavior has been proven to be different from their in-plane mechanical properties, it highlights a gap in knowledge. A better comprehension of this would improve the evaluation of conformability.

Finally, it is brought to the attention their implementation to other types of sensor that, up to now, have not been evaluated. Particularly, in-socket pressure sensors would take benefit from the improved conformability, because of the irregular shape of the patients residual limb.

## **Chapter 3**

# **Sinusoid lattice patterns: design, parametrization, and in-plane mechanical properties**

An approach to improve conformability of wearable devices has been the adaptation of auxetic lattice structures to materials for the design of flexible devices. A type of these structures are topologies based on sinusoidal waves, under certain combinations of frequency, amplitude and length of the sine wave, present auxetic behavior.

In this chapter, the parameterization of sinusoid lattices is presented, along with their computational modeling, mathematical calculation of the relative density and computational characterization of Poisson's ratio.

### **3.1 Sinusoid lattice parameterization and computational modeling**

In this section, the description of the topologies based on sinusoidal waves is made, including their parameterization and dimensions for the computational modeling of a set of samples in computer aided design software (CAD). Finally, the calculation of their relative density is presented.

### 3.1.1 Sinusoid lattice curves parameterization

The chosen topologies for the study include two sinusoidal patterns (figure 3.1a. and 3.1b.) and the square lattice (3.1 c). All the patterns are constructed with unit cells defined by equations

$$y = A \sin(ki) \quad (3.1)$$

$$k = \frac{w\pi}{\lambda}, \quad (3.2)$$

where  $\lambda$  is the length of the unit cell,  $A$  is the amplitude of the sine wave,  $w$  defines the frequency of the sine wave, and  $i$  is each discretized value to construct the unit cell. These patterns are known to present auxetic behavior with certain combinations of their parameters, and are illustrated in figure 3.1, for each topology. The chosen values for the frequency  $w$  are 1 (figure 3.1a.) and 2 (figure 3.1b.), for the topologies referred to as topology W1 and topology W2, respectively. Apart from the frequency, another difference between both sine topologies is the direction of their sine waves. Topology W1 has each period of the sine wave mirrored to one another, while topology W2 has them parallel. The design process is detailed and illustrated in the computational modeling section.

As it can be observed, both topologies are constructed by the repetition of the horizontal and vertical sinusoidal waves (defined by its amplitude and length) with a given thickness  $t$ . Thickness was added with parallel curves, first, the parameterized form of equation 3.1,

$$f(i) = \begin{pmatrix} i \\ A \sin(ki) \end{pmatrix}. \quad (3.3)$$

was used to find the equations that define the  $x_p(i)$  and  $y_p(i)$  coordinates of the parallel lines given a parameterized curve:

$$x_p(i) = x' + \frac{ty'}{\sqrt{(x')^2 + (y')^2}}, \quad (3.4)$$

$$y_p(i) = y' - \frac{tx'}{\sqrt{(x')^2 + (y')^2}}, \quad (3.5)$$

respectively. Where  $x'$  and  $y'$  are the derivatives of the parameterized curve, and  $t$  is the

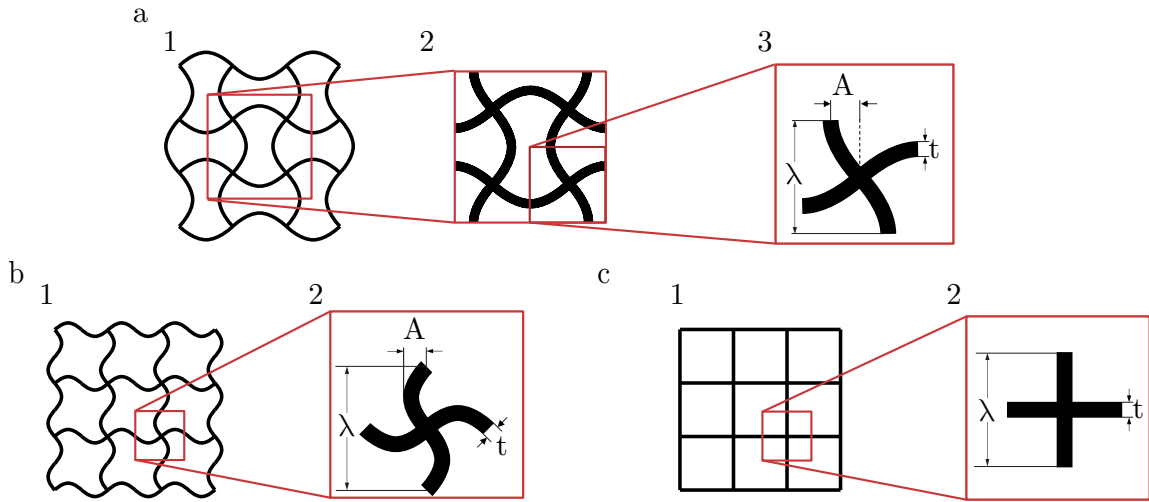


Figure 3.1: Schematics of the topologies chosen for the study: a. (1) Sinusoidal lattice W1, with a representation of its (2) unit cell, and (3) the parameters that define it; b. (1) Sinusoidal lattice W2, with a representation of its (2) unit cell and parameters that define it; and c. (1) Square lattice, with a representation of its (2) unit cell and the parameters that define it.

perpendicular distance from the original curve to its parallel, which was used as the thickness of the filament. Equation 3.3 was substituted in equations 3.4 and 3.5 and resulted in equations

$$x_p(i) = 1 + \frac{tAk \cos(ki)}{\sqrt{1 + [Ak \cos(ki)]^2}}, \quad (3.6)$$

$$y_p(i) = A \sin(ki) - \frac{t}{\sqrt{1 + [Ak \cos(ki)]^2}}, \quad (3.7)$$

The third topology chosen was the square lattice (Figure 3.1c.), note that is the sinusoidal wave when the amplitude is equal to zero, and was constructed using the same parameterized equations already mentioned. These equations were implemented in a macro for SOLIDWORKS for the design of the unit cell, which allowed to do variations of each parameter and generate automatically the unit cell of the topology.

### 3.1.2 Computational modeling of samples

The equations obtained from before (3.6 and 3.7) were implemented in a macro for SOLIDWORKS, for which each curve (vertical and horizontal) was discretized from the parameter  $\lambda$  into 1000 points. The value of  $t$  was defined as half the target thickness, so that both parallel curves were equally distanced from the main curve. The topology W2 unit cell is composed of a sine wave defined along the  $x$  axis (horizontal) and another along the  $y$  axis (vertical) defined by the same parameters, intersecting at the midpoint. This element is obtained from the macro, converted into a solid and repeated to obtain the desired topology. On the other hand, topology W1 is constructed using this same principle, with a vertical and a horizontal sine wave, but this element is mirrored along the  $x$  and  $y$  axes (Figure 3.2 c.1) to construct the unit cell to be repeated. From here, the unit cells of all the topologies were extruded 1 mm (Figures 3.2a.2, 3.2b.2, 3.2c.3) and repeated to create 5 cm<sup>2</sup> samples (Figures 3.2a.3, 3.2b.3, 3.2c.4).

### 3.1.3 Relative density

The relative density of a lattice, to be represented with the symbol  $\bar{\rho}$  from now on, is defined as the ratio between the superficial volume  $v_s$  and the external volume  $v_e$  of its unit cell, as follows

$$\bar{\rho} = \frac{v_s}{v_e}. \quad (3.8)$$

The dimensions of the unit cell are defined by  $\lambda$ , therefore, the external volume  $v_e$  corresponds to  $\lambda^2$ , as illustrated in figure 3.3 a.1 and b.1. The superficial volume  $v_s$  was calculated using the equation

$$v_e = 2st - t^2, \quad (3.9)$$

[13], where  $s$  corresponds to the length of the curve, and  $t$  the thickness of the filament. This equation represents that the unit cell is composed of two curves of length  $s$  with its defined thickness (figure 3.3 a.2 and b.2), intersect at the midpoint, thus eliminating the fraction corresponding to  $t^2$  (figure 3.3 a.3 and b.3). Substituting this equation in equation

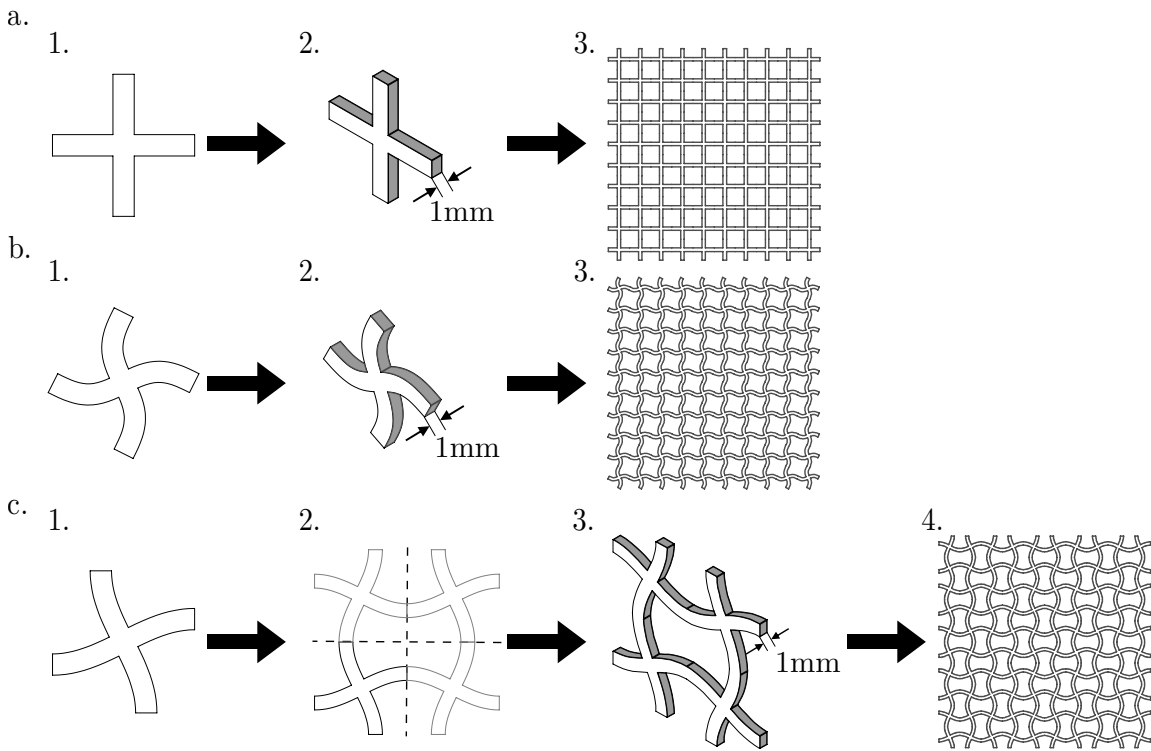


Figure 3.2: Process for the computational design of the square and sinusoidal lattices a. Square, b. Topology W2, and c. Topology W3. For a and b, 1. is the result of the macro implemented in SOLIDWORKS, 2. Extrusion of 1 mm to create a solid and 3. Repetition of unit cells to create the lattice. For c, 1. Curves result of the macro, 2. Curves mirrored in both axes to create the unit cell, 3. The surface was extruded 1 mm, and 4. A matrix of the solid unit cell was done to obtain a  $5 \times 5$  cm lattice.

3.8, it is obtained

$$\bar{\rho} = \frac{2st - t^2}{\lambda^2} \quad (3.10)$$

to calculate the relative density of the unit cells of the three topologies.

The calculation of  $s$  was done using the formula to of the length of a parameterized curve:

$$s = \int_0^\lambda \sqrt{f'(i) \cdot f'(i)} di = \int_0^\lambda \sqrt{1 + ((k \cdot A \cos(k \cdot i))^2}, \quad (3.11)$$

for which  $f(i)$  was already defined in equation 3.3). Some unit cells of the three topologies



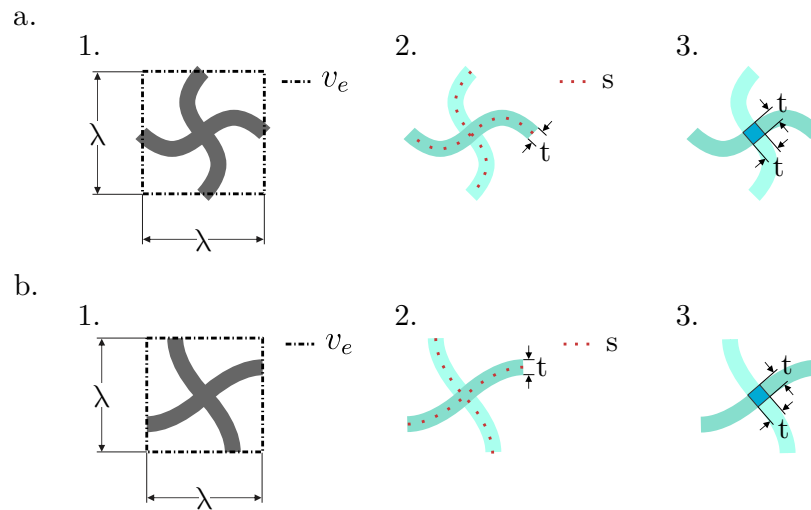


Figure 3.3: Process to compute relative density of sinusoidal topologies a. W2, and b. W1. Showing 1. External volume of the unit cell, 2, sine curves with length  $s$  and thickness  $t$ , and 3. Fraction of  $t^2$  because of the inter crossing of each curve.

grouped by their values of relative density and dimensions are presented in figure 3.4. It was found that amplitude increases relative density and that, for same values of  $\lambda$  and  $t$ , topology W2 had the same relative density than topology W1 with twice the amplitude.

## 3.2 Computational characterization of the role of sine geometry on the Poisson's ratio

As previously mentioned, auxetic structures have been the preferred topologies for materials in wearable applications. Here, a characterization of the topologies' Poisson's ratio  $\nu$  was measured using Finite Element Analysis simulations. The type of finite elements, boundary conditions, other specifications for the mechanical characterization via computations and their corresponding results are reported in this section.

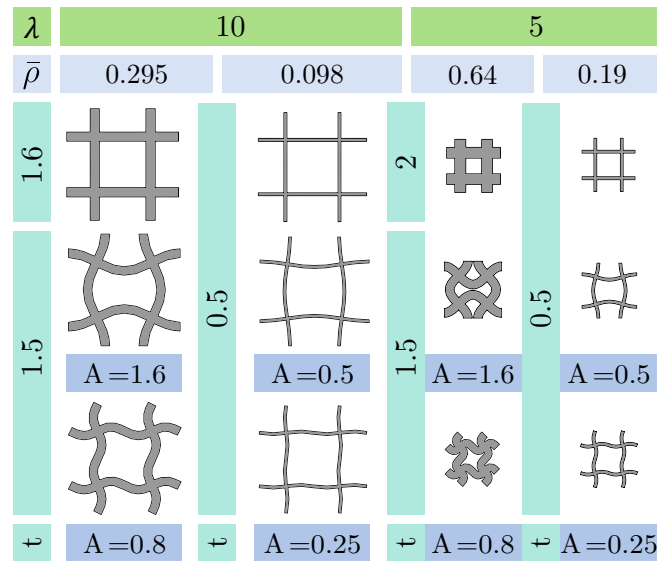


Figure 3.4: Square and sinusoidal lattices samples with equivalent values of relative density.  $\lambda$ ,  $t$  and  $A$  are in mm.

### 3.2.1 Sinusoidal topologies designed with different combinations of parameters

In order to establish a better structure-property relation between the parameters of the topology and its Poisson's ratio, there were made modifications to each parameter ( $\lambda$ ,  $t$ , and  $A$ ) of the topologies W1 and W2. Modifications were done by fixing two of the three parameters and varying the remaining one. For the analysis of  $\nu$  in terms of amplitude  $A$ ,  $\lambda$  was fixed to 10 mm, and  $t$  to 1.5 mm. The varying range for  $A$  was from 0.5 to 4, for topology W1; and 0.25 to 3.5 for topology W2, which was the highest value of amplitudes before the unit cell exceeded its dimensions in combination with the fixed values  $\lambda$  and  $t$ . Note that the square lattice is formed when  $A = 0$ . In figure 3.5a. and c. the samples for topology W1 and W2 are presented, respectively, with the minimum and maximum values of the variation of  $A$ . Equivalently, for the samples designed with varied thickness  $t$ , the values fixed were  $\lambda = 10$  mm, and  $A = 1.6$ ; and  $t$  was varied from 0.5 mm in increments of 0.25 mm to the maximum thickness permitted by the unit cell, 4 mm. The unit cells for minimum and maximum values are presented in figure 3.5b. and f. Finally,

for the variations of  $\lambda$ , thickness was fixed at  $t = 1.5$  mm, and the amplitude at  $A = 1.6$  and  $A = 0.8$  for each topology. The range of values of  $\lambda$  was set from 5 mm to 10 mm with increments of 0.5 mm, figure 3.5c. and g., shows the samples with the minimum and maximum value chosen for  $\lambda$ .

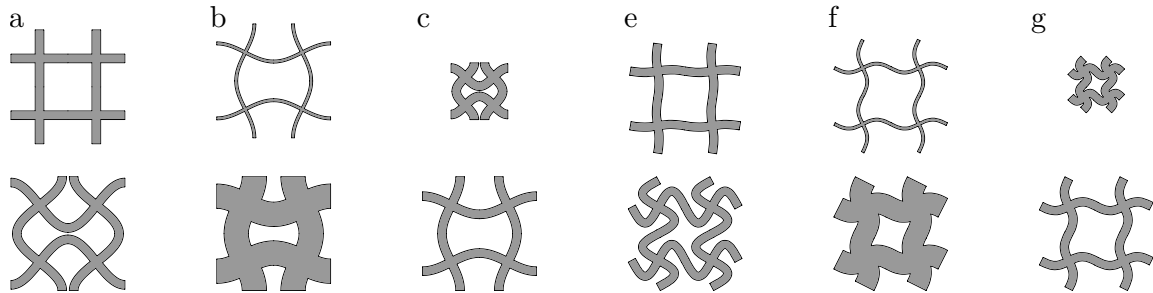


Figure 3.5: Illustration of the samples with minimum (up) and maximum (down) values of the variations of Topology W1's parameters a. Amplitude  $A$ , b. Thickness  $t$ , and c. Length of unit cell  $\lambda$ ; and Topology W2's d. Amplitude  $A$ , e. Thickness  $t$ , and f. Length of unit cell  $\lambda$ .

### 3.2.2 Type of finite elements comparison for the numerical characterization of the $\nu$

Poisson's ratio is the relation between strains  $\epsilon$  along two orthogonal axes. This property can be computed thru an FEA mechanic simulation of conventional test, such as tension or compression using the equation

$$\nu = \frac{\epsilon_T}{\epsilon_a}. \quad (3.12)$$

In both scenarios (tension and compression),  $\epsilon_T$  is the transverse strain (strain perpendicular to the load applied), and  $\epsilon_a$  is the axial strain (strain in the direction of the load).

As already mentioned, this characteristic can be obtained with two different mechanical tests, and there was a variety of Software available and element types to perform the FEA study. To determine which one was faster and more reliable, nine samples of the ones mentioned before were chosen randomly to compare these available tools.

A compression test was simulated using shell elements in COMSOL Multiphysics of  $10 \times 10$  cm samples designed. The width  $w$  of the samples was established as the

variable for the shell elements (Figure 3.6a.) defined at 10 cm to create cubic samples. The boundary conditions for these simulations are shown in figure 3.6b., they correspond to a force  $F$  of -1N applied on the top of the sample, and a fixed support applied on the bottom of the sample.

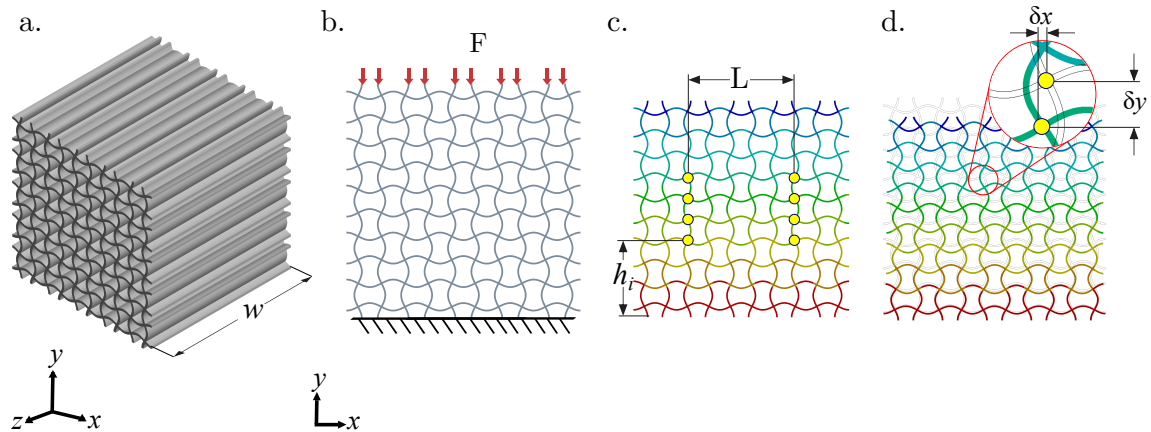


Figure 3.6: FEA of compression test to compute Poisson's ratio of the samples using shell elements: a. Variable  $w$  to establish shell elements of the samples, b. Boundary Conditions of the samples subjected to compression, and c. Nodes of the samples where displacements were taken to do the calculations.

Tensile tests were simulated using tetrahedral elements in COMSOL Multiphysics and ANSYS Workbench, and beam elements in ANSYS APDL. For this characterization,  $60 \times 180 \times 1$  mm samples were designed. The boundary conditions for these simulations are shown in figure 3.7b, that correspond to a force  $F$  of 1N applied on the top of the sample, and a fixed support applied on the bottom of the sample.

In both scenarios (tension and compression), the transverse strain  $\epsilon_T$  is the deformation of the sample along  $x$  axis; and the axial strain  $\epsilon_a$  is the deformation along  $y$  axis. These values were calculated as  $\epsilon = \frac{\delta}{L}$ , where  $\delta$  is the displacement of the node, and  $L$  is the length of the sample before deformation (both along its corresponding strain axis). The information of the central nodes, illustrated in figures 3.6c. and 3.7b., was used to calculate an average of the Poisson's ratio, so this would be free from the edge effects. Axial strain  $\epsilon_a$  was calculated by dividing the displacement in the  $y$  axis,  $\delta_y$  (Figure 3.7c.)

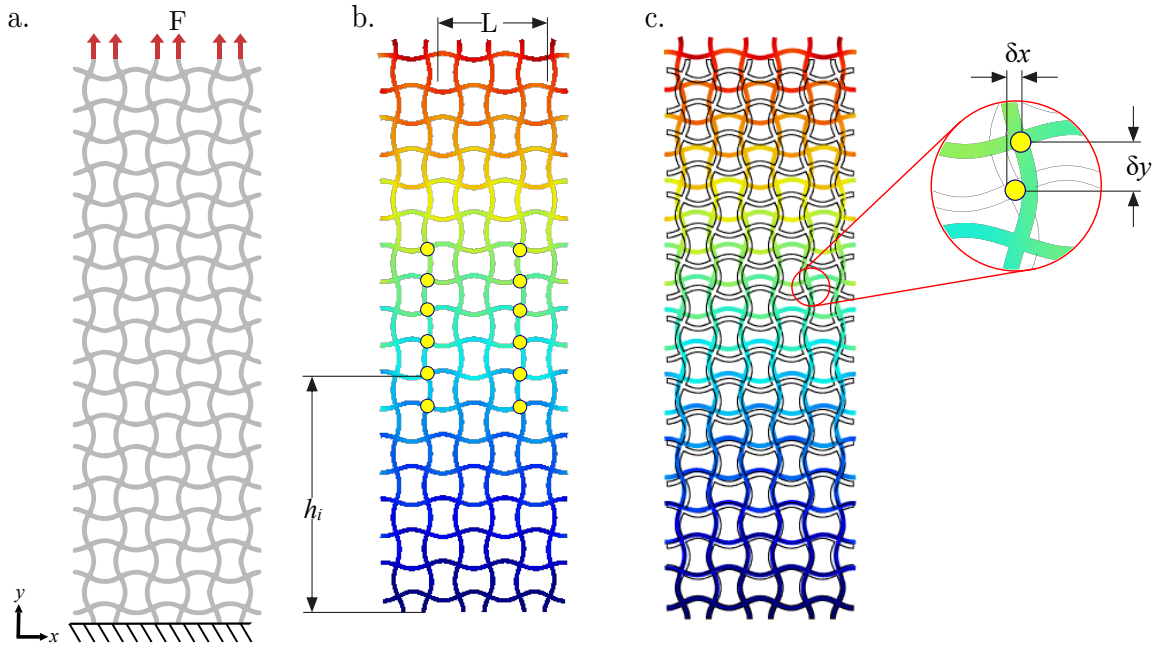


Figure 3.7: FEA of tensile test to compute Poisson's ratio of the samples: a. Fixed support and tensile load  $F$  applied to the sample, b. Illustration of the nodes selected to calculate Poisson's ratio, its height ( $h$ ) and width ( $w$ ); and c. Illustration of the displacements in  $x$  and  $y$  used to calculate the strain.

by the height of the node  $h$ , an average was made of all the nodes. In a similar way, transverse strain  $\epsilon_T$  was calculated by obtaining the average distance between the nodes of the left and right ( $L$ ), and dividing it by the average of the displacements of each node along the  $x$  axis,  $\delta_x$  (figures 3.6d and 3.7c).

A comparison of the Poisson's ratio results obtained from one of the samples (thickness variation of  $t = 3$  mm), along with the number and type of elements used is shown in Table 3.1, and the differences of the mesh quality obtained in each technique explored are illustrated in figure 3.8.

Table 3.1: Comparison of the type and number of elements to compute  $\nu$ 

Software	Test	Element Type	Total elements	Comp. time	$\nu$
COMSOL	Tension	Tetrahedral	2,073,768	6 min 32 s	-0.345
ANSYS WB	Tension	Tetrahedral	18,000	1 min 52 s	-0.327
COMSOL	Compression	Shell	340,944	5 min 3 s	-0.346
ANSYS WB	Compression	Shell	95,131	2 min 19 s	-0.09
ANSYS APDL	Tension	Beam	3,000	1 s	-0.315

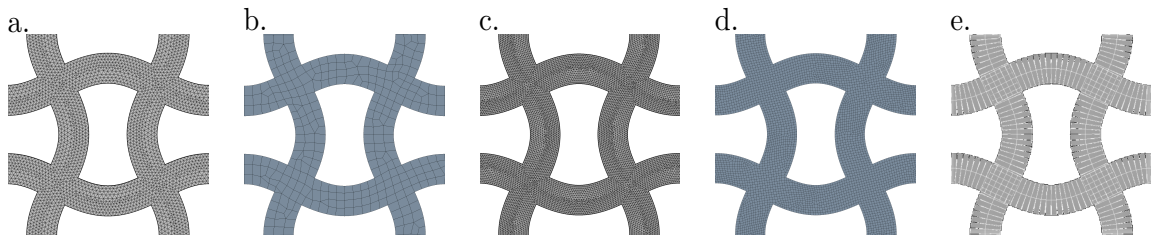


Figure 3.8: Mesh obtained in different tests, FEA software, and element types: a. Tension in COMSOL Multiphysics using tetrahedral elements, b. Tension in ANSYS Workbench using tetrahedral elements, c. Compression in COMSOL Multiphysics using shell elements, d. Compression in ANSYS Workbench using shell elements, and e. Tension in ANSYS APDL using beam elements.

### 3.2.3 Results and discussion of computational characterization of Poisson's ratio

After performing the comparison from above, it was determined to do a tensile test with tetrahedral elements in COMSOL Multiphysics, since it was the best quality of mesh obtained and computational performance was not limited. Each of the samples mentioned in section 3.2.1 was subjected to tension, and meshed with a maximum size of 0.6 mm. All topology W1's samples resulted to be auxetic. The effect of each parameter on the Poisson's ratio is presented in figure 3.9. Note a linear relation between thickness  $t$  and  $\nu$ , where thinner samples are more auxetic (figure 3.9 a.). Also, higher values of amplitude  $A$ , produce more auxetic topologies, meaning more negative values of  $\nu$  (figure 3.9 b). Finally, varying the values of  $\lambda$  seem to not have an effect on  $\nu$  (figure 3.9 c).

Moreover, a comparison was made plotting  $\nu$  against the non-dimensional ratio of

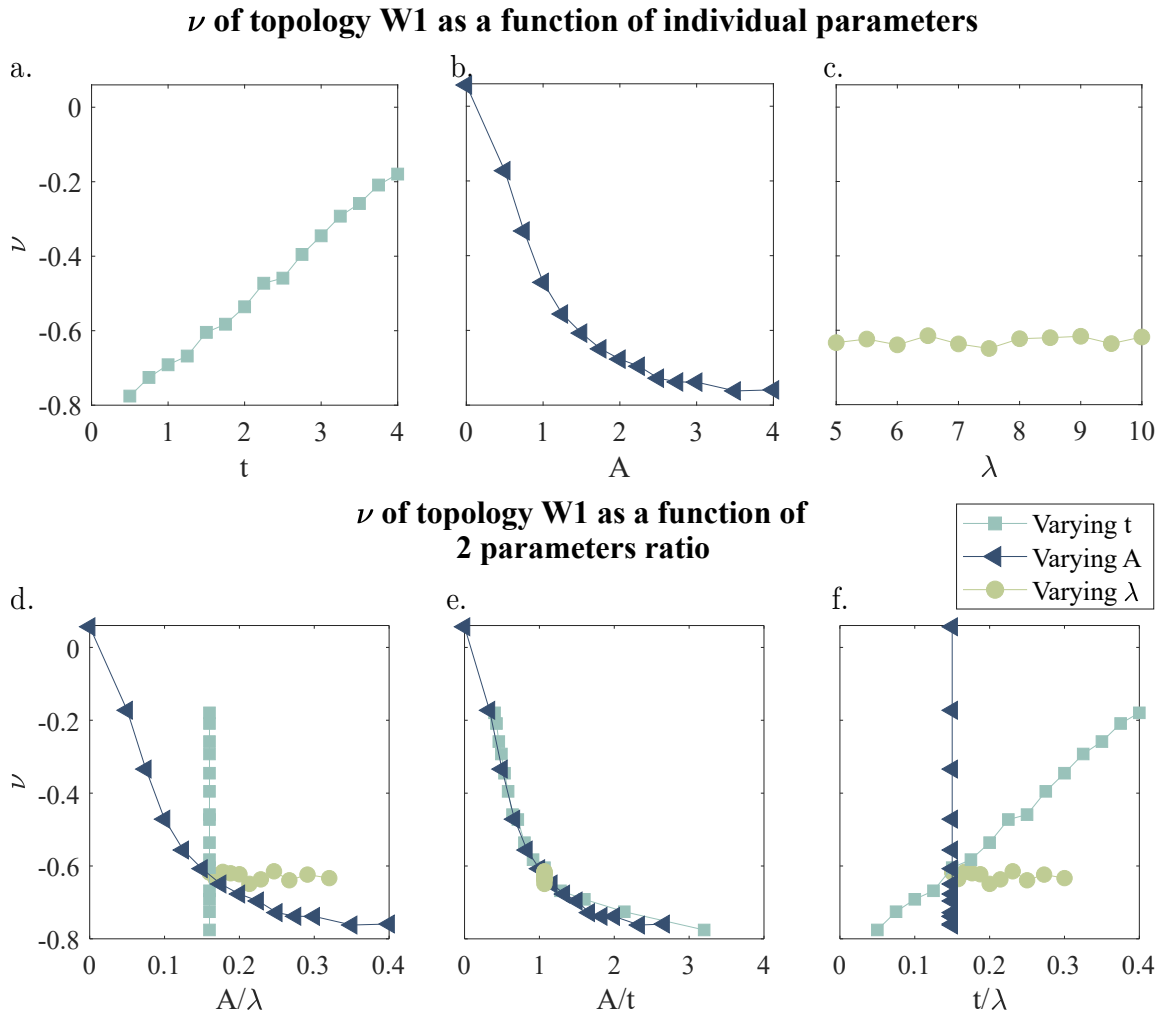


Figure 3.9: Results of  $\nu$  for topology W1, presented as an individual plot for each modified parameter: a. Thickness  $t$ , b. Amplitude  $A$ , and c. Length of the unit cell  $\lambda$ . The  $y$  axis of all plots corresponds to plot a. Comparison of the results of  $\nu$  for topology W1 in relation with the ratio of two parameters: d. Amplitude and length of the unit cell  $A/\lambda$ , e. Amplitude and thickness  $A/t$ , and f. Thickness and length of the unit cell  $t/\lambda$

two parameters:  $A/\lambda$  (figure 3.9d.),  $A/t$  (figure 3.9e.) and  $t/\lambda$  (figure 3.9f). Considering the  $A/t$  ratio it is observed that all the samples with the same ratio produce the same value of  $\nu$ , regardless of the individual value of each parameter (inside the range of values that were tested), and that this property is not influenced by  $\lambda$ , bringing the opportunity to design topologies with targeted  $\nu$  for specific applications.

In the study made for topology W2, on the contrary to what was observed for topology W1, some samples resulted not auxetic. An individual plot for each set of modifications of  $\nu$  as a function of each parameter is presented in figure 3.10, a dashed line marks  $\nu = 0$ , to differentiate auxetic from non auxetic results. A clear relation between  $\nu$  and  $t$  (figure 3.10 a.) is observed, where only very thin samples resulted in auxetic topologies. Recalling from section 3.2.1, parameter  $t$  was fixed in 1.5 mm for the variations of  $A$  and  $\lambda$ , the sample corresponding to this variation of  $t$  in figure 3.10a. is non-auxetic, and by further inspecting figures 3.10b. and 3.10c., all variations of  $A$  and  $\lambda$ , respectively, resulted in non-auxetic samples, indicating that these parameters do not have influence on auxeticity. Additionally, these results were also plotted against the ratio of two parameters, specifically in figure 3.10c., it can be observed the clear effect of the  $t/\lambda$  ratio on  $\nu$ , having the amplitude  $A$  almost a null effect. To support this conclusion, there were added more samples to the study, doing variations of  $A$  and  $\lambda$ , fixing the value of  $t$  at 0.5 mm. It was confirmed that this sample resulted with auxetic properties. These results can be found in the plots of figure 3.11, all the new modifications of the samples resulted in auxetic topologies, which supports the initial statement of  $A$  and  $\lambda$  not having an effect on determining the sign of the Poisson's ratio.



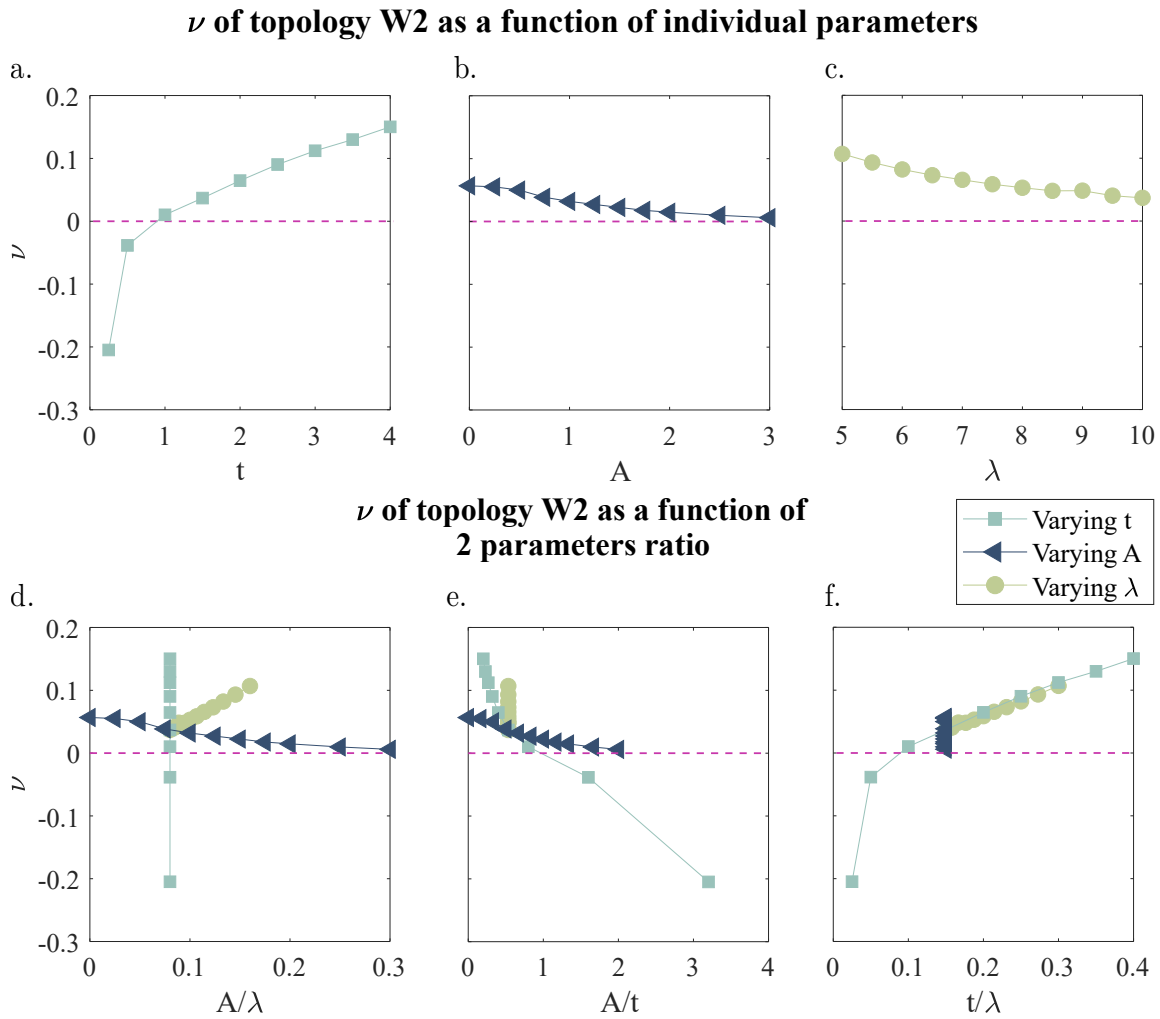


Figure 3.10: Results of  $\nu$  for topology W2, presented as an individual plot for each modified parameter: a. Thickness  $t$ , b. Amplitude  $A$ , and c. Length of the unit cell  $\lambda$ . The  $y$  axis of all plots corresponds to plot a. Comparison of the results of  $\nu$  for topology W2 in relation with the ratio of two parameters: d. Amplitude and length of the unit cell  $A/\lambda$ , e. Amplitude and thickness  $A/t$ , and f. Thickness and length of the unit cell  $t/\lambda$ .

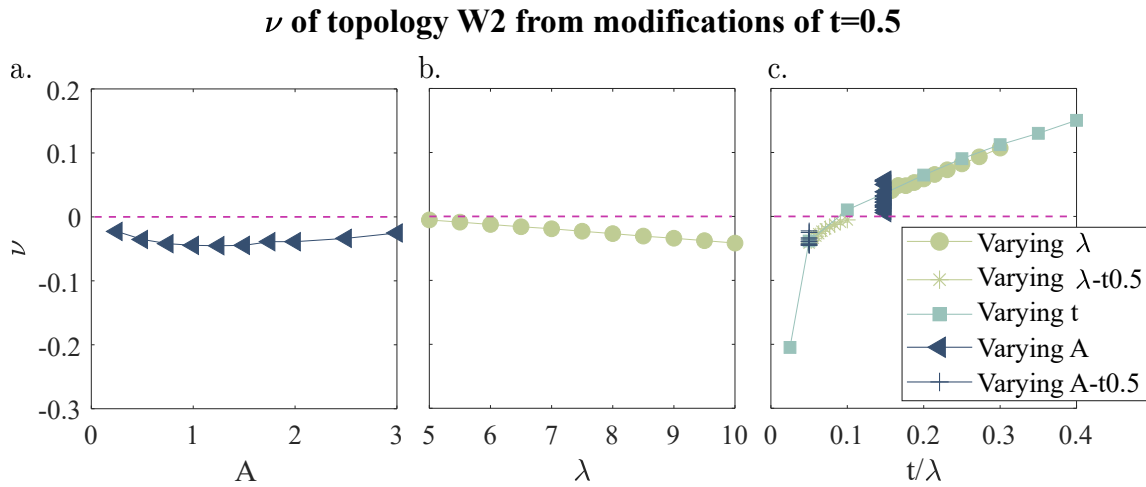


Figure 3.11:  $\nu$  results of additional samples of topology W2, fixing  $t = 0.5$  with modifications of a. Amplitude  $A$ , and b. Length of the unit cell  $\lambda$ ; and c. comparison of all the modifications made of topology W2 in relation with  $t/\lambda$  ratio. The dashed line marks  $\nu = 0$  to separate auxetic and non-auxetic results.

### 3.3 Summary

In the calculations of relative density it was found that amplitude increases relative density, compared to a square lattice of the same  $\lambda$  and  $t$ . Meaning that, to find a square and a sinusoidal lattice equally dense, an increase in thickness is needed. How much is needed to increase will depend on the other parameters. Moreover, for same values of  $\lambda$  and  $t$ , topology W2 has the same relative density than topology W1 with twice the amplitude.

The characterization of Poisson's ratio  $\nu$  of topology W1 indicated that  $\lambda$  has no influence on changing its value, and that samples with the same value in the ratio of  $A/t$  result in topologies with the same  $\nu$ , independent from the individual value of the three parameters. Moreover, in the characterization of topology W2, even though  $A$  and  $\lambda$  influence the value of  $\nu$ , they do not determine whether a sample presents auxetic property or not, hence, auxeticity depends mostly on the thickness of the sine waves  $t$ . Also, samples with the same value of the ratio  $t/\lambda$  result in the same  $\nu$ , regardless of the individual values of each parameter. This brings the opportunity to design topologies with targeted  $\nu$

for specific applications.

## **Chapter 4**

# **Out-of-plane mechanical properties of 3D printed samples and conformability tests**

As previously mentioned, conformability is an important characteristic for wearable devices, so that they can stretch and wrap around the target body part. In this chapter, a finite element analysis characterization of the sinusoidal and square lattices' out-of-plane-stiffness is presented and contrasted with experimental tests in section 4.1. Moreover, specifications of the conformability characterization via out-of-plane loading, including the methodology of digital image processing and its statistical analysis is described in section 4.2.

### **4.1 Finite Element Analysis and experimental study of out-of-plane stiffness of sinusoidal lattices**

A study of the stiffness  $k$ , of the samples in their out-of-plane direction was performed to determine the level of flexibility of the samples designed. This is done via FEA simulation and experimental tests on 3D printed samples. Specifications of the fabrication of samples, and the experimental setup for the mechanical tests, along with the boundary conditions

of the simulations and their results are presented in this section.

### 4.1.1 Additive manufacturing of samples and experimental setup description of out-of-plane stiffness evaluation

This experiment was used to evaluate out-of-plane at the same time as conformability (more details in section 4.2.1). A set of 20 samples with different parameters was designed. For each parameter, a minimum and maximum value was set, samples were designed using combinations of these. The biggest value for  $\lambda$  was set as 10 mm, and the smallest as 5 mm. As these samples were to be manufactured using Fused Deposition Modeling (FDM) and the extruder's nozzle had a diameter of 0.4 mm, the minimum thickness  $t$  was defined as 0.5 mm, and the maximum as 1.5 mm, which was the biggest thickness achievable for the  $\lambda = 5$  mm samples. Finally, the values for the amplitude  $A$  were defined specifically for each type of sinusoidal topology, for topology W1 the minimum value was 0.5 mm and the maximum 1.6 mm. In order to match the relative density between sinusoidal topologies, topology's W2 amplitude were half of the defined values for topology W1, 0.25 and 0.8 mm. These values were determined by combining the maximum thickness and amplitude and verifying the correct design of the topology for the smallest size of unit cell  $\lambda = 5$  mm. The final values of each parameter are summarized in Table 4.1.

Table 4.1: Values of the parameters of the sinusoidal lattices samples designed. All units in mm.

	$\lambda_{min}$	$\lambda_{max}$	$t_{min}$	$t_{max}$	$A_{min}$	$A_{max}$
Topology W1	5	10	0.5	1.5	0.5	1.6
Topology W2					0.25	0.8

The square lattices samples were obtained using parameters set to match the relative density of the sinusoidal samples. The values of  $\lambda$  were kept the same, and the variations were done to the thickness of the filament until a match in relative density was found. These parameters are shown in Table 4.2.

Table 4.2: Values of the parameters of square lattice samples.

$\lambda$ [mm]	$t_{min}$ [mm]	$t_{max}$ [mm]
5	0.5	2
10	0.5	1.6

Finally, all the unit cells studied here are depicted in figure 4.1. These unit cell designs are grouped according to the geometrical and dimension parameters used to conform them (top of figure 4.1) and the corresponding unit cells presented on the bottom sections of the figure.

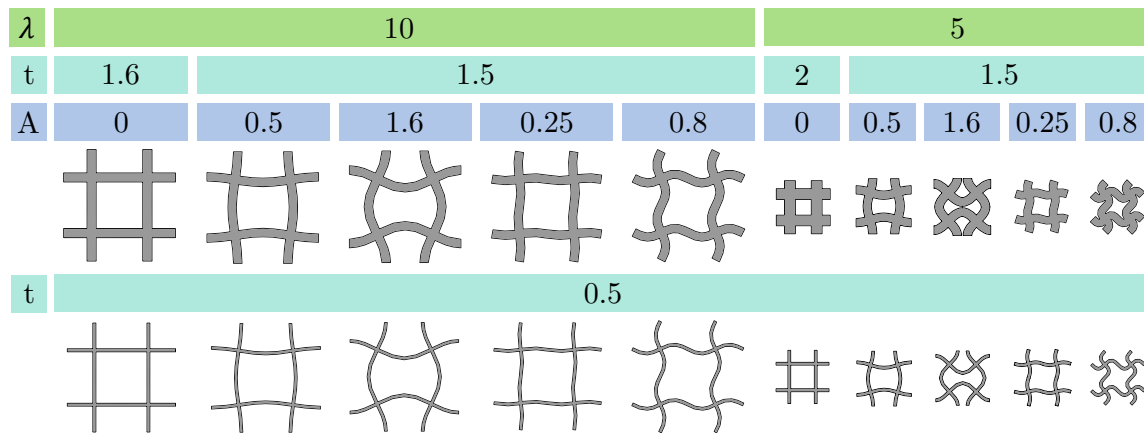


Figure 4.1: Samples designed for the study of the square and sinusoidal lattice, grouped by their parameters. All units in mm.

Three repetitions of each topology of  $5 \times 5$  cm and 1 mm of width were fabricated with Polylactic Acid (PLA) using Fused Filament Deposition Modeling, with the 3D printer Ultimaker 3. The specifications used were layer thickness of 0.1 mm and print speed of 50 mm/s, using a printing temperature of 200°C and a build plate temperature of 60°C. All samples were printed lying flat on the printing plane.

The experiment was put together using a setup to keep the samples in place to be tested with a Perten Instruments TVT 6700 texture analyzer. The setup consists of a series of elements assembled together illustrated in figure 4.2, which contains four pairs of jaws

designed to fix the samples from the corners adjusted to the size of the unit cell, a support to hold the jaws in place with screws, a base to put on the support, and a fixer for the base to be always on the same place of the texture analyzer.

Once the setup is assembled, the sample is fixed and a 1" spherical probe is placed in the texturometer. The probe is painted with Politec washable tempera (this step is used for the conformability analysis). The programmed test on the texture analyzer software TexCalc5 consists on placing the probe 20 mm on top of the sample and a downward displacement of the probe until a trigger force of 0.05 N is detected, then, it moves to a 15 mm displacement to load the sample at a velocity of 1 mm/s. Then, it holds the position for 5 seconds and returns to the starting position. This process was repeated on each of the three repetitions of each topology. The data saved from the test software consists on time (s), displacement (mm) and force (grams) at a 100 points per second (pps) rate.

To evaluate  $k$ , a single value of force from the elastic linear zone (slope 1 in figure 4.11) of the force-displacement curve was chosen. Its corresponding value of displacement was obtained and the average of the three repetitions of each topology was calculated.

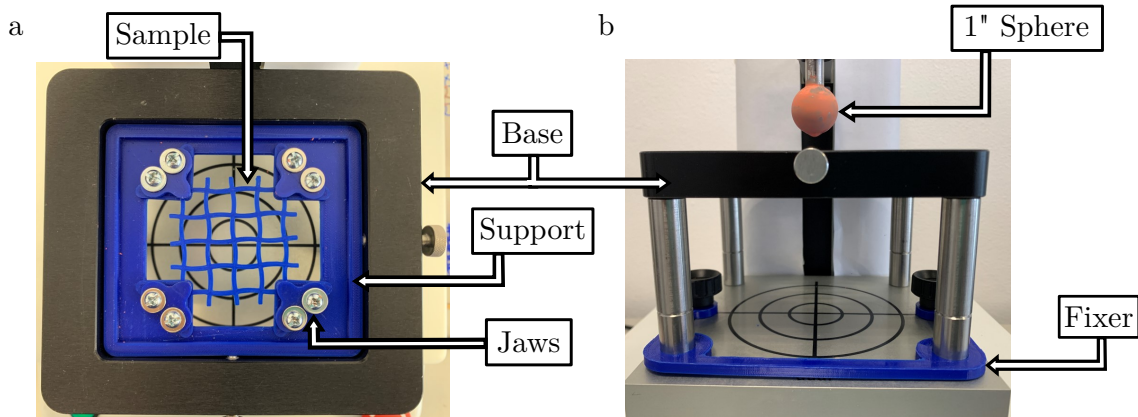


Figure 4.2: Experimental setup to hold the sample in place consisting on four pairs of jaws hold by a support that is placed on a base fixed to the texture analyzer. a. Top and b. Front views

### 4.1.2 Finite element analysis simulations to evaluate stiffness

Each sample subjected to out-of-plane loading in the finite element software Ansys Workbench to replicate the experiment. The boundary conditions used were fully fixed supports on the corners to have a restriction of displacement and rotation of the edges (figure 4.3a.). The material used for the samples was PLA with a Young's modulus of 2.35 GPa, obtained from the Ultimaker's material data sheet. A sectioned sphere of 1" diameter was centered on top of the sample, with zero displacement on  $x$  and  $y$  axes; free displacement and a force along  $z$  direction (figure 4.3b). A frictionless contact was established between the sample and the sphere, using a pinball region of radius 10 mm. This pinball determines the gap or penetration allowed for contact, if contact elements are in the near-field to the target elements, more contact checking is performed. Each sample was meshed using tetrahedral elements with maximum size of 0.4 mm for the samples with  $t = 1.5$  mm, and 0.25 for the samples of  $t = 0.5$  mm. The sphere was meshed also with tetrahedral elements with maximum size of 1 mm. The force applied to the sphere was specified for each sample according to their force-displacement curve obtained from the experimental tests, and the maximum displacement resulted in the  $z$  direction was used to compute the stiffness  $k$  illustrated in force-displacement curves.

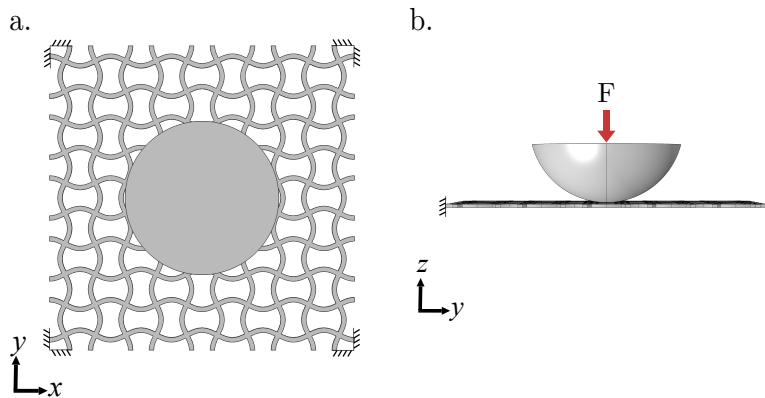


Figure 4.3: Boundary conditions to evaluate  $k$  on FEA simulations. a. Top view showing the fixed supports on the corners of the samples, b. Front view illustrating the applied force on the face of the fractioned sphere.



### 4.1.3 Stiffness numerical results

From the FEA simulations, the displacement  $\delta$  along the  $z$  axis produced by the applied force  $F$  was used to compute the stiffness of each sample using  $k = F/\delta$ . These values were used to analyze the tendency and effect of each topology parameter on the stiffness of the lattices. The main effects of the topology parameters on the stiffness  $k$ , grouped by the type of topology, is presented in figure 4.4. This type of plot computes the mean of a response variable grouped by the levels of each parameter, for example the value of stiffness for  $\lambda = 5$  mm, includes the  $k$  of all the samples with this parameter, regardless of its amplitude or thickness. In both plots it is observed that the three parameters affect the stiffness of the sample, however the thickness  $t$  has the highest influence. Both topologies have similar response to the change of length of the unit cell  $\lambda$ . However in terms of  $A$ , in the plot of topology W1 (figure 4.4a.) it is observed that shifting from the square lattice ( $A = 0$ ) to a sinusoid makes the sample more flexible, and increasing the amplitude does not have a proportional effect. Contrary to the topology W2, where increasing the amplitude from 0.25 to 0.8 mm has a higher effect, than increasing from 0.5 to 1.6 mm in topology W1.

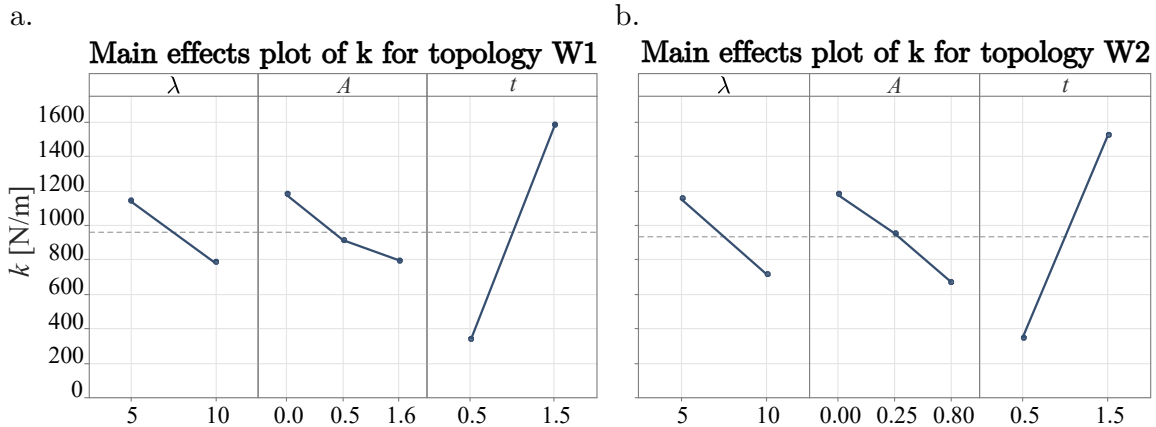


Figure 4.4: Main effects plots of each parameter grouped by sinusoid topologies a. W1 and b. W2, including the square lattice into each group as a sinusoid lattice with zero amplitude.  $y$  axis is the same for both plots.

The effect of each parameter is analysed individually, beginning with the length of the unit cell  $\lambda$ . Plots grouped by the three types of topologies are presented in figure 4.5,

note that increasing the value of  $\lambda$  makes the sample more flexible, this effect is more evident in the three types of topologies with values of  $t = 1.5$  mm, producing groups of thin and thick samples, which is more noticeable for the square lattice (figure 4.5a).

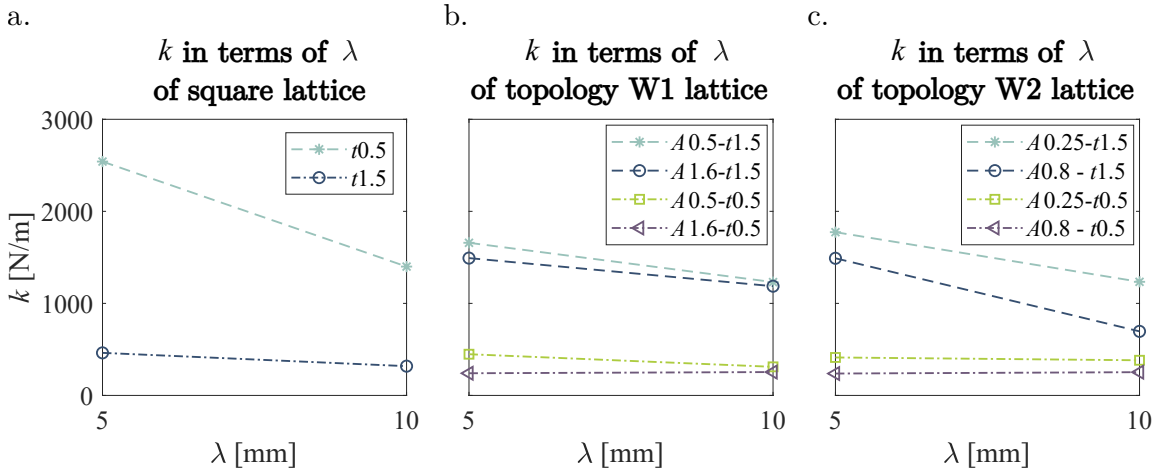


Figure 4.5: Stiffness  $k$  in terms of the length of the unit cell  $\lambda$  plots grouped by type of topology a. Square, b. Topology W1, and c. Topology W2 lattices.  $y$  axis is the same for all plots.

Following up with stiffness  $k$  in terms of thickness  $t$  (plots in figure 4.6), the effect of  $t$  is characterized, thicker filaments produce stiffer samples, and, at the same time, this has higher effect in samples with smaller unit cells.

The last parameter is amplitude  $A$ , plotted in figure 4.7, here the square lattice was included into each sinusoidal topology as  $A = 0$ . It can be observed that changing from the square lattice to a sinusoidal topology, even with small amplitude (0.5 mm for topology W1, and 0.25 mm for topology W2), reduces significantly the stiffness of the sample (more evident in the thicker samples  $t = 1.5$  mm with smaller unit cell  $\lambda = 5$ ) mm. This becomes more relevant taking into account that increasing the amplitude increases the relative density of the sample. This effect is reduced as the unit cell increases its size ( $\lambda = 10$  mm) and the sinusoid waves get thinner ( $t = 0.5$  mm).

A comparison of the stiffness between topologies with the same relative density  $\bar{\rho}$  is included in figure 4.8. In general it is observed that decreasing  $\bar{\rho}$ , also decreases the stiffness of the sample, and that including amplitude to the sample, makes it more flexible, i.e., changing the sample from the square lattice to any of the sinusoidal topologies. This

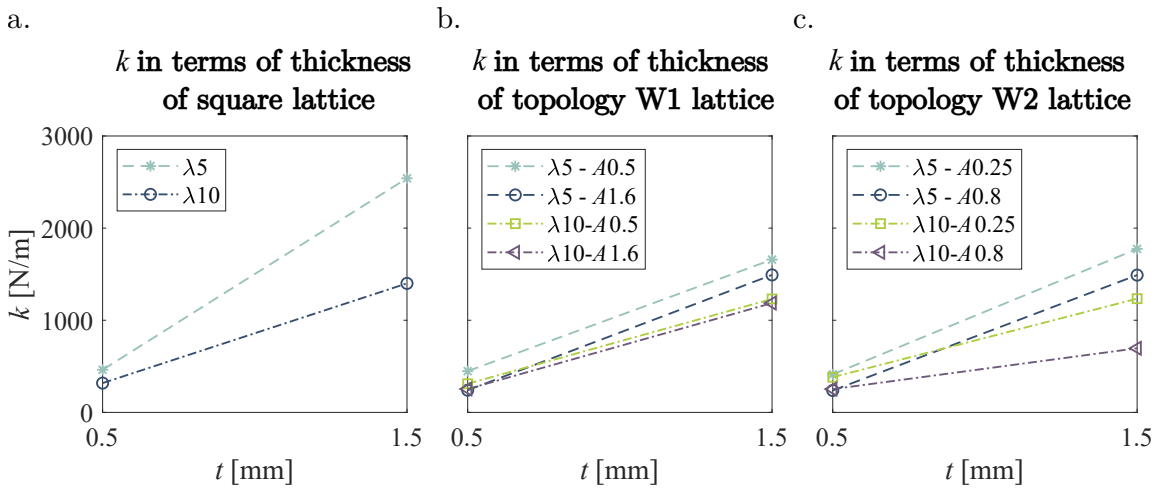


Figure 4.6: Stiffness  $k$  in terms of thickness  $t$  plots grouped by type of topology a. Square, b. Topology W1, and c. Topology W2 lattices.  $y$  axis is the same for all plots.

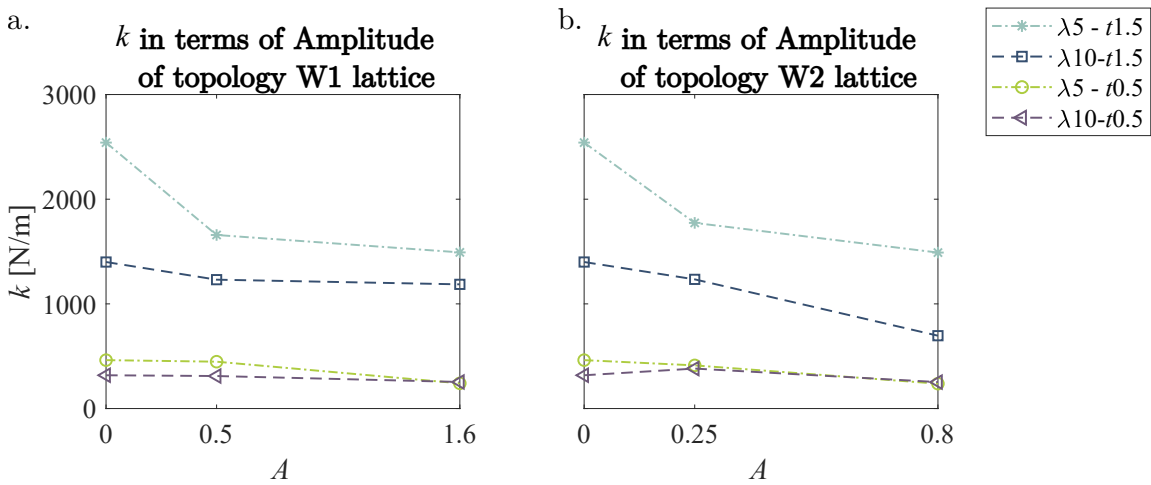


Figure 4.7: Stiffness  $k$  in terms of the amplitude  $A$  plots grouped by sinusoid topologies a. W1 and b. W2, including the square lattice into each group as a sinusoid lattice with zero amplitude.  $y$  axis is the same for both plots.

effect is most clearly demonstrated in the lines of  $\bar{\rho} = 0.28$  and  $0.29$ , where both correspond to the same parameters of  $\lambda$  and  $t$ , however, the most dense samples are the ones with the high value of amplitude (1.6 for topology W1 and 0.8 for topology W2), and are more flexible than those with the low value of amplitude (0.5 for topology W1 and 0.25

for topology W2), more clearly observed in the topology W2.

**Stiffness comparison of relative density and Topology type**

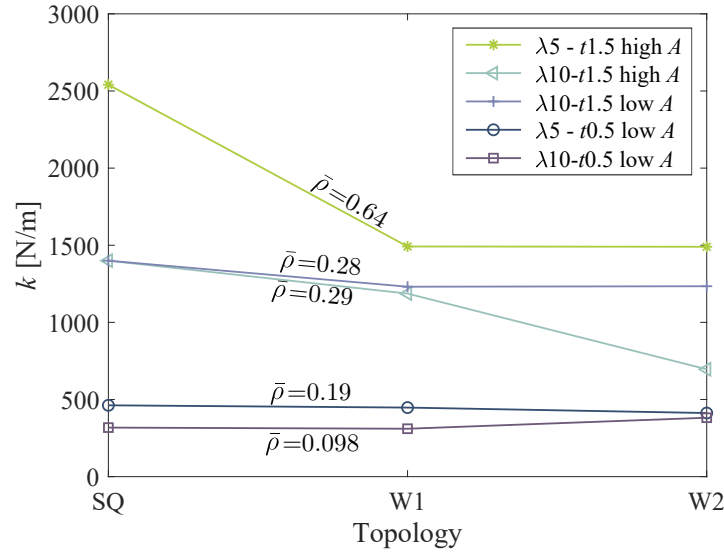


Figure 4.8: Stiffness  $k$  calculated thru simulations in terms of type of topology, only samples with equivalent relative density  $\bar{\rho}$  were included. For topology W1 high  $A$ 's value corresponds to 0.5, and low  $A$  to 1.6, for topology W1 the values are 0.25 and 0.8 respectively.

#### 4.1.4 Contrast of numerical results with experimental tests

In this section a comparison between numerical results obtained from before and the experimental tests is presented. Specific topologies are identified by their parameters in the form TT- $\lambda$ X- $A$ XX- $t$ XX, where TT corresponds to the type of topology (SQ for the square lattice, and W1 and W2 for sinusoidal topologies W1 and W2), and each parameter ( $\lambda$ ,  $A$  and  $t$ ) is followed by its value.

An initial validation of the results was done by comparing the behavior of the stiffness in terms of  $A$ . A pair of plots displaying the averaged force-displacement curves from the experimental tests of the three repetitions of three topologies with the same parameters of  $\lambda$  and  $t$ , and different  $A$  are included in figure 4.9. Note that follows the tendency stated in the plots of figure 4.7, where shifting from the square lattice to a sinusoidal topology (increasing amplitude) reduces stiffness. Pictures of these samples (SQ- $\lambda 5-t0.5$ ,

W1- $\lambda 5-t0.5-A1.6$  and W2- $\lambda 5-t0.5-A0.8$ ) with the load applied during the experiment are presented in Figure 4.10. The deformed samples in FEA simulations were also included in the same figure. A load of 2N was applied to all the samples, but sinusoidal topologies demonstrate more displacement, i.e. they are more flexible.

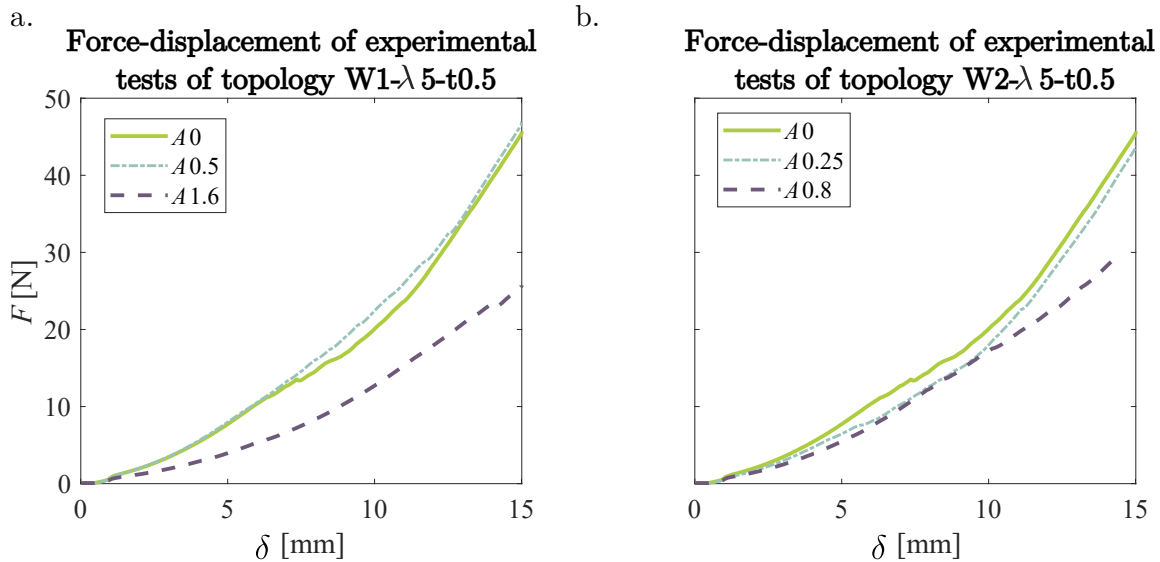


Figure 4.9: Force-displacement plots of experimental tests of sinusoidal topology a. W1- $\lambda 5 - t0.5$ , and b. W2- $\lambda 5 - t0.5$ , each curve corresponds to different amplitudes, including the square lattice into each group as a sinusoid lattice with zero amplitude.  $y$  axis is the same for both plots.

As the load-displacement curves resulted with changes in slopes, these were analyzed to identify the elastic linear zone. There is an example of a complete curve presented in figure 4.11, exhibiting these changes in different styles of line. From inspecting the video recorded tests, a clear slip of the sample from the clamps was noted and reflected in the force-displacement curve with evident changes in slope. Also, the rigidity of the fabricated support was so that the corners bent when the load was applied, affecting this measurement. Because of this, only the first slope of the curve was used to compute the stiffness of the samples, since the rest of it can be the beginning of the plastic deformation of the sample, bending of the experimental setup or a combination of both.

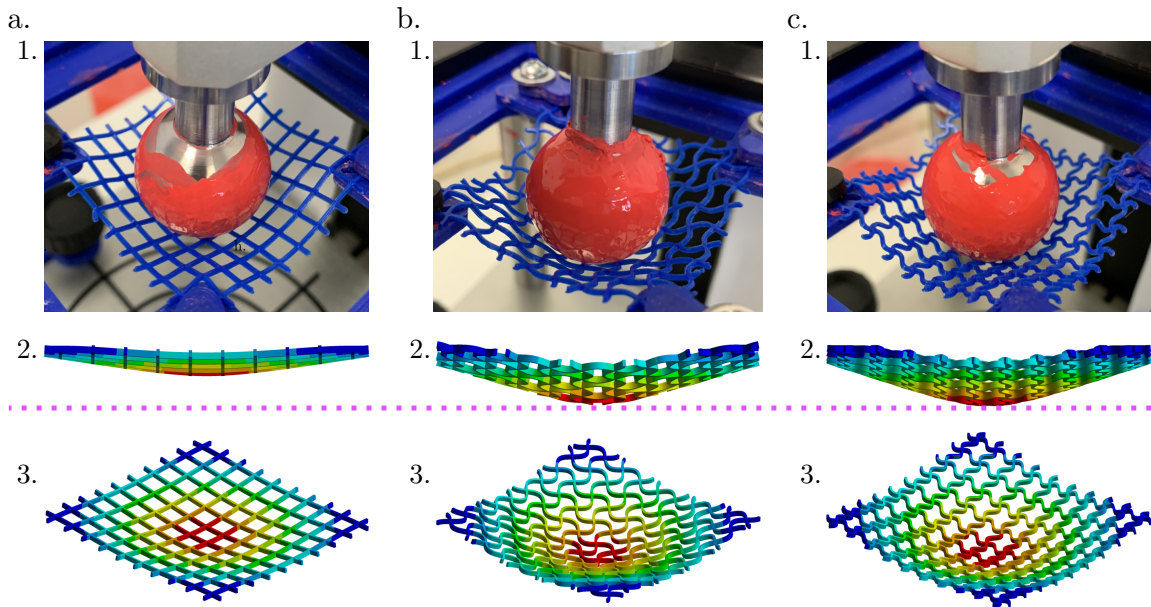


Figure 4.10: Deformed shapes of the a. Square, b. Topology W1 and c. Topology W2 lattices during out-of-plane loading in 1. experimental tests and FEA simulations 1. front view and 2. isometric view. The dashed line shows the difference between the deformation of square and the sinusoidal topologies lattices.

Experimental force-displacement plot

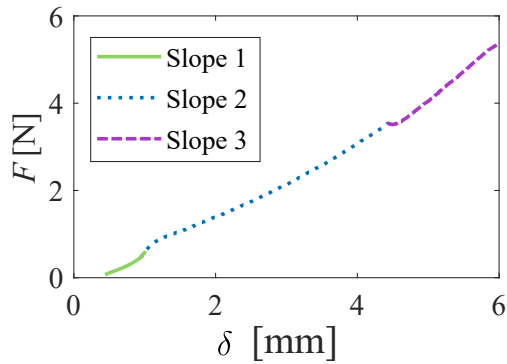


Figure 4.11: Force-displacement plot from the experimental run of the sample designed with topology W1,  $\lambda = 5$  mm,  $t = 5$  mm and  $A = 1.6$  mm, run 1. Slope 1 marks the beginning of the test (sphere touches the sample), slope 2 occurs when the sample slides from the clamps, and slope 3 possible combination of plastic deformation of the sample and bending of the experimental setup.


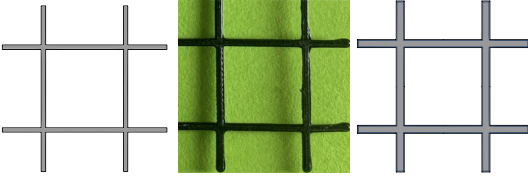
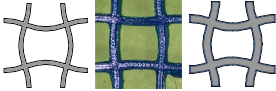
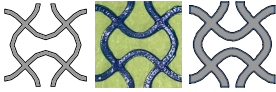


Taking this into consideration, the results obtained from both approaches (simulations and experimental) were compared to compute the percentage error between the average displacement from the experimental tests and the displacement obtained from the simulations. An initial comparison revealed high percentage errors (average errors measured 26.5%).

This could be attributed to fabrication defects, the resulting thickness  $t$  and width  $w$  of the 3D printed samples varied from the intended ones. Hence a further inspection of the 3D printed samples was done. This consisted of obtaining the dimensions of the actual samples. The thickness  $t$  of each fabricated sample was measured, taken three readings with a digital caliper from each sample, and the average was computed. It was obtained an averaged variation of 0.4 mm in all the samples, which lead to errors up to 70% between thickness in CAD models and 3D printed samples. This process was repeated with the width  $w$  of the samples, in the CAD models was designed to be 1 mm, however fabricated samples presented a width around 0.72 mm. It was found that fabrication defects have a wider effect on high amplitude samples, when redesigning samples to include  $t$  adjustments, high amplitude samples were not able to be designed, since sine waves overlapped with one another. For instance, when adjusting the thickness for the topology W2 with amplitude 0.8 mm,  $\lambda = 5$  mm,  $t = 1.5$  mm (real thickness 2.1 mm), it resulted in the unit cell illustrated in the third image of topology  $\lambda 5 - t 1.5 - A 0.8$  in Table 4.3, by reducing the amplitude in steps of 0.1, the maximum amplitude allowed for this thickness was 0.5 mm, which, according to the tendency, would make a sample stiffer.

To deepen in this analysis, there were chosen 6 samples with different values of errors from the original CADs to adjust its thickness  $t$  and width  $w$  to the measured values, their stiffness was computed and the error was re-calculated. From the six chosen samples, it was obtained a maximum error between simulations and experiments of 82.4% (% Error Original CAD in Table 4.3), then, when adjusting only the thickness the maximum error was 72.7%. Finally, when combining both adjustments,  $t$  and  $w$ , the maximum error found was reduced 18.9%. In Table 4.3 are also illustrated the original designs, the resulting fabricated sample, and the CAD with the adjustment of  $t$ .

In figure 4.12a. is plotted the standard deviation of the stiffness from experimental

Table 4.3: Experimental and FEA simulations' results of stiffness

Topology	% Error Original CAD	% Error Adjusted $t$	% Error Adjusted $t$ and $w$
$\lambda 5-t0.5$ 	3.9%	56.0%	1.4%
$\lambda 10-t0.5$ 	27.2%	72.7%	1.6%
$\lambda 5-t0.5-A0.5$ 	3.5%	50.6%	18.9%
$\lambda 5-t0.5-A1.6$ 	78.3%	37.7%	2.5%
$\lambda 5-t0.5-A0.8$ 	82.4%	47.4%	10.6%
$\lambda 5-t1.5-A0.8$ 	25.0%	29.2%	17.2%

tests of the six samples mentioned and the computed  $k$  from FEA simulations, high percentage errors drop outside its standard deviation. Moreover, in figure 4.12a. are shown the same results from experimental tests, now compared against the  $k$  from the adjusted  $t$  and  $w$ , where it is observed that most of the FEA results are inside or closer to the standard deviation.



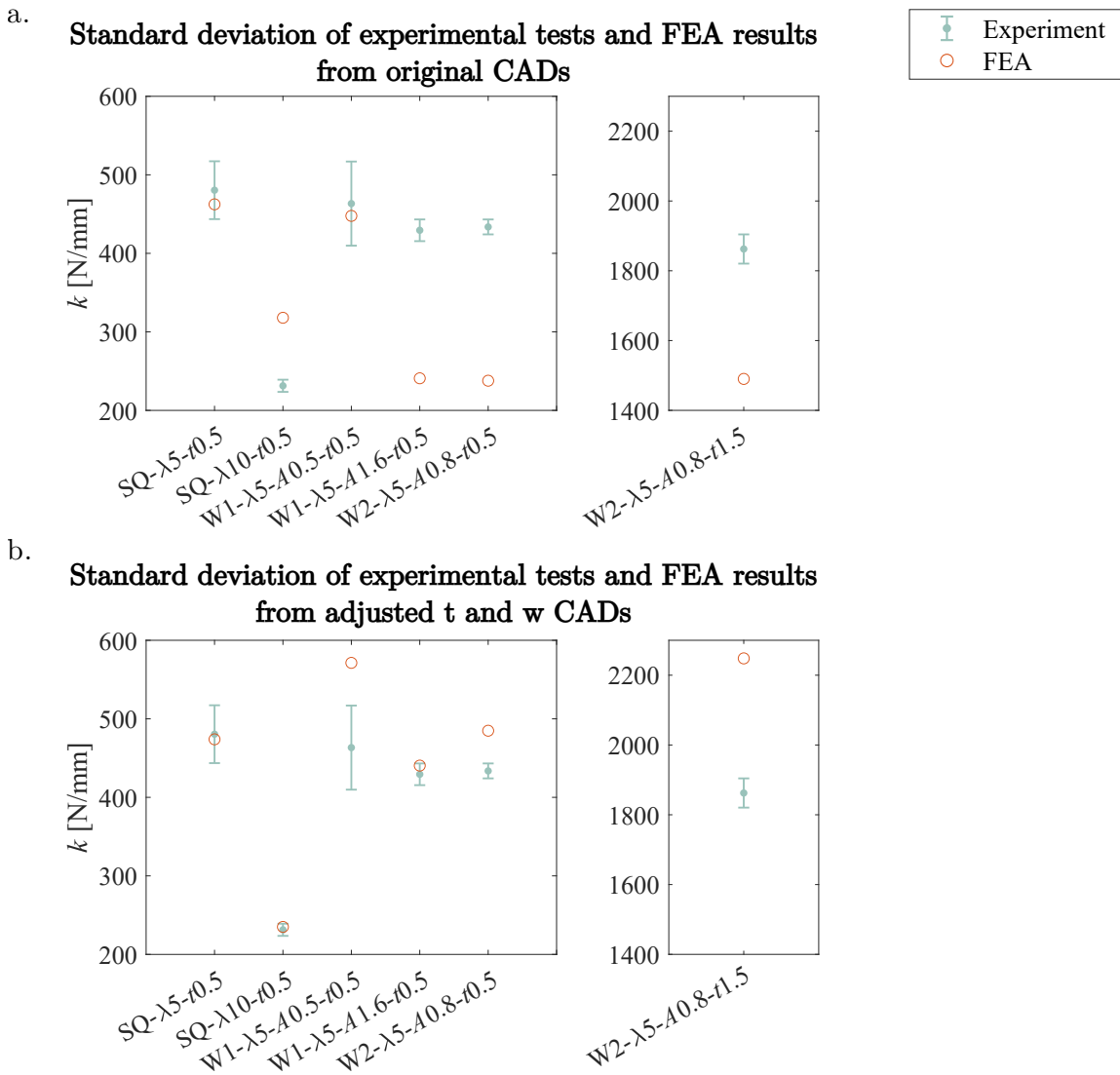


Figure 4.12: Standard deviation and FEA results of stiffness  $k$  from a. Original CAD and b. CAD with adjustments of  $t$  and  $w$ , showing the reduction of error between both characterizations.

## 4.2 Conformability characterization via out-of-plane loading and digital image processing

As mentioned in section 4.1, each sample was subjected to out-of-plane loading. Conformability was evaluated experimentally by computing a ratio between the area touching the sphere and the total area of the sample. These variables were obtained from the painted area left from the contact of the spherical probe on the sample. In this section the digital image processing method, is to be presented. Also, the results obtained from the conformability experimental tests, which covers an statistical analysis in Minitab in order to determine which parameters and combination of parameters affected the conformability ratio.

### 4.2.1 Digital image processing methodology for conformability characterization

Each sample was portrayed in a digital image after the out-of-plane loading, they were placed on a green sheet of paper, that contrasted with the blue PLA samples, a photograph was taken with a 12MP resolution camera at a distance of 150 mm and saved in a JPG format. These were processed on an image processing software, ImageJ, which manages it as an RGB color image (figure 4.13a.1). This means that the matrix of pixels that compose the image is presented into 256 values in each of the RGB channels (Red, Green, Blue). From here, it was changed to an RGB stack, which is a set of the three channels separated individually as 8-bit images, i.e. an image displayed in 256 gray levels (figure 4.13a.1, 4.13a.2, and 4.13a.3). This step allowed to isolate the colors useful to get resulting variables, achieved by doing calculations with the values of the pixels between the images of the stack. From this process a set of variables was obtained, the first was the area, in pixels, of the sample that was painted by the sphere during the experiment (figure 4.13b.3), and the total area, in pixels, of the sample (figure 4.13b.2).

The PLA samples painted area was isolated from the Red channel; the software allows to select a threshold in which the pixels inside the range change to all black pixels (an assigned value of 255, illustrated in figure 4.13b.2). The limits of the threshold were

adjusted manually for each sample to ensure including the whole painted area. Furthermore, the sample area was isolated from the difference between the pixel values of Red and Green channels (figure 4.13c.1), the threshold was adjusted to include the whole sample.

Conformability could be seen as the ratio between the area of the sample touching the sphere  $A_t$  and the sample's external area  $A_e$ . The software allows to do geometrical selections from the image and then measure the area in pixels. For the sample's external area  $A_e$ , the Rotated rectangle selection tool was chosen, and it was manually adjusted to fit in the whole sample, as illustrated in figure 4.14a. The touching area  $A_t$  (figure 4.14b.) was obtained from an ellipse approximation of the painted area, using the Elliptical selections tool (4.14b). A higher ration translates to more surface area of the sphere in contact with the sample, meaning it conformed better. These results are presented in the next section.

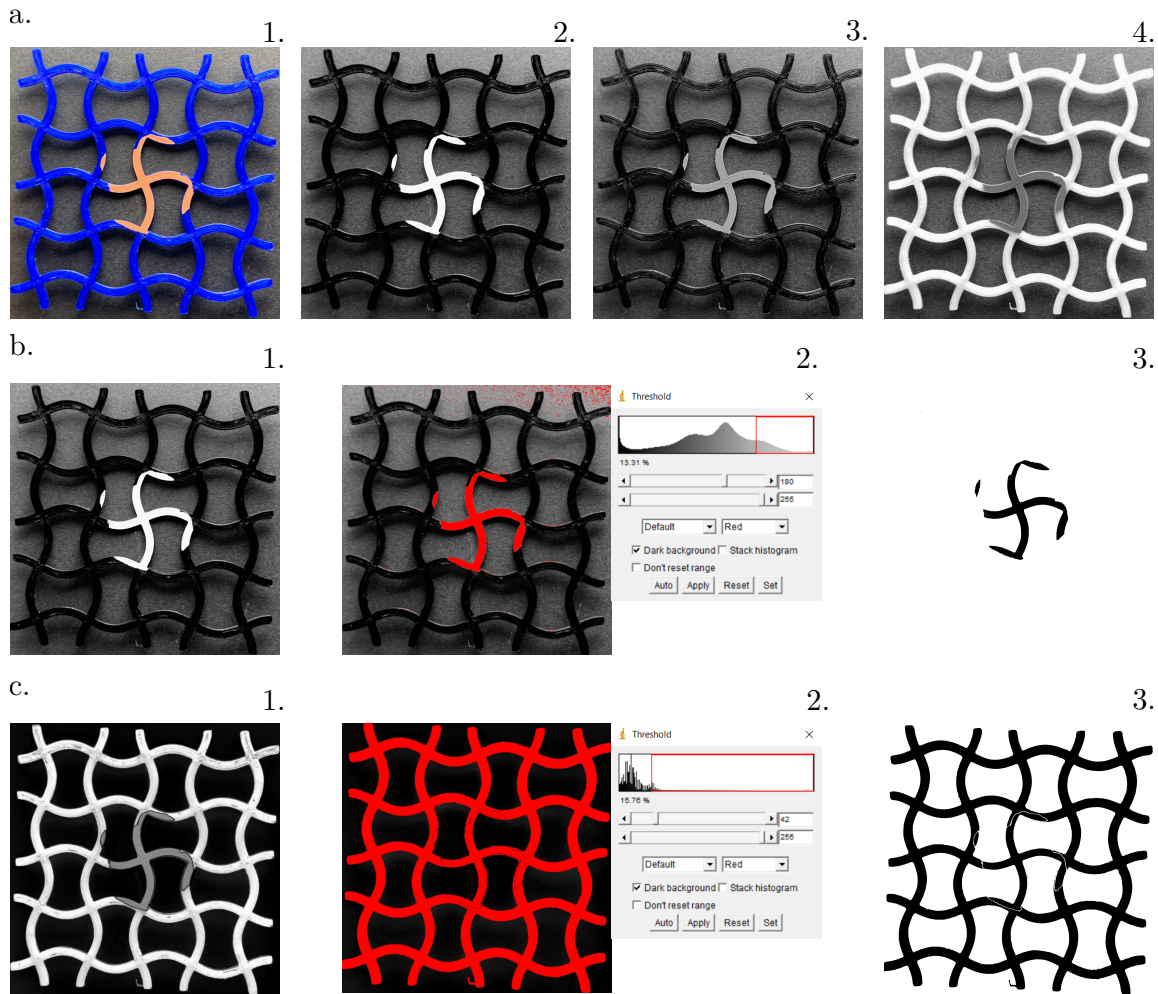


Figure 4.13: Image processing methodology in the software ImageJ after the experimental out-of-plane loading tests of fabricated samples. a. Decomposition of the 1. Original RGB color image; into the RGB stack presented as 8 bit images for each channel: 2. Red, 3. Green, and 4. Blue; b. Process to isolate the painted area of the sample: 1. Red channel from the stack, 2. Adjustment of the threshold to filter the pixels that belong to the painted area, and 3. Resulting isolated painted area; and c. Process to separate the total area of the sample from the background: 1. Resulting image of the subtraction Red-Green channels, 2. Adjustment of the threshold to filter the pixels that belong to the sample, 3. Resulting isolated sample, with changed values of the pixels.

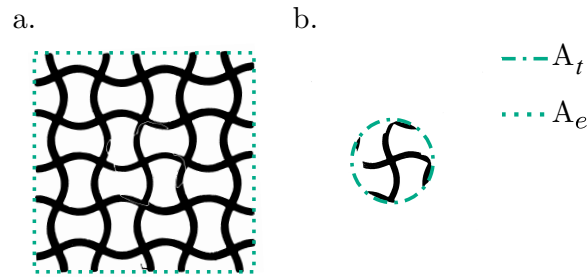


Figure 4.14: Geometrical selections of the processed images to obtain a. External area of the sample  $A_e$  and b. Touching area from paint  $A_t$ .

## 4.2.2 Experimental results and statistical analysis of conformability ratio

In order to determine which parameters and combination of them affected the conformability ratio, an statistical analysis was performed in Minitab. An important note is that the three repetitions of the densest topologies with  $\lambda = 5$  mm and  $t = 1.5$  mm of the square lattice, topology W1 with  $A = 1.6$  mm, and topology W2 with  $A = 0.8$  mm fractured during the experimental test, as presented in figure 4.15.

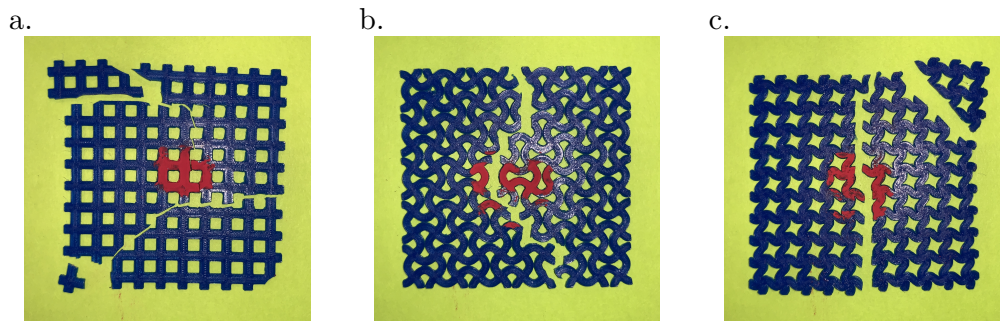


Figure 4.15: Fractured topologies during the experimental test a. SQ- $\lambda 5-t 2$ , b. W1- $\lambda 5-t 1.5-A 1.6$ , and c. W2- $\lambda 5-t 1.5-A 0.8$

Four separated generalized linear models (GLM) were performed, the first included all the samples studied, where the topology was considered as one of the factors; the other three correspond to each topology, separately. To consider the reliability of the

results, the residuals of the model need to be normally distributed with equal variance, these assumptions were validated with a normal probability test and an equal variance test. The results from the GLM are presented in analysis of variance (ANOVA) tables. If the P-Value obtained for a factor was greater than  $\alpha$ , this parameter affected the response variable.

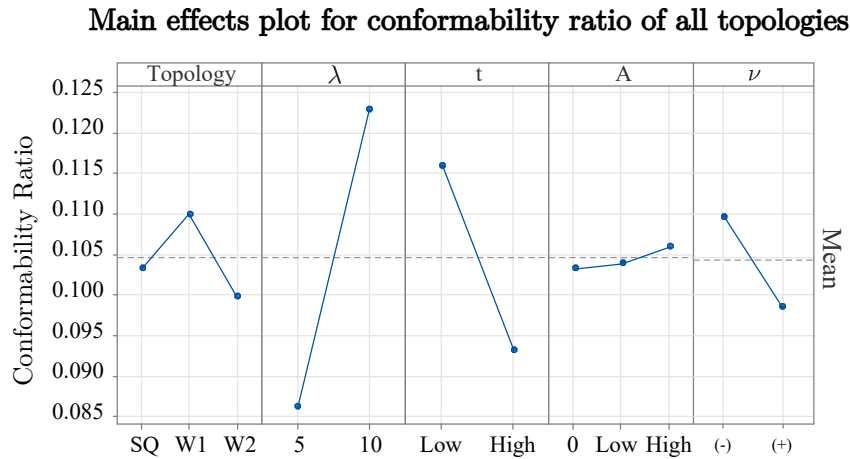


Figure 4.16: Main effects plot of the mean of conformability ratio of all the levels of each factor: topology type,

Before presenting the GLM results, the main effects plot of the mean of stiffness of all the levels in each factor is presented in figure 4.16. Since there were different values of amplitude for each sinusoidal topology, these were grouped as High and Low amplitude. There was also included the information of Poisson's ratio  $\nu$  to indicate if a sample was auxetic (-) or not (+). In the plot is observed that  $\lambda$  and  $t$  affect the most the conformability ratio, and from here, it can be hypothesized that topology W1 has better conformability, increasing the value of amplitude also improves conformability, and that auxetic samples perform better. Next is presented the results from the analysis of variance.

The generalized linear model performed to analyze all the experimental tests of all the topologies, considered the three parameters and the type of topology as factors. Parameter  $A$  was nested to the type of topology, since the values of the levels are specific to the topology (as described in Table 4.1), and is to be referred as  $A(\text{Topology})$ ; in a similar way the factor  $t$ , for which the thickness in the square lattice samples was calculated to

match the relative density in some samples of topologies W1 and W2, therefore it was also nested in Topology and  $\lambda$ , identified as  $t(\text{Topology}, \lambda)$ . In the model were also included the interactions between the variables  $\lambda$  and  $A$ , Topology and  $\lambda$ ; and  $A$  and  $t$ . The response variable evaluated was conformability ratio given a 0.05 confidence level  $\alpha$ , the results are shown in the ANOVA Table 4.4. From the P-Values that resulted, it is observed that the parameters  $\lambda$  and  $t$  affect significantly the conformability ratio.

Table 4.4: Analysis of variance table of the analysis including all the topologies tested.

Source	DF	Adj SS	Adj MS	F-Value	P-Value
$\lambda$	1	0.018715	0.018715	45.22	0.000
$t(\text{Topology}, \lambda)$	6	0.009838	0.001640	3.96	0.003
$A(\text{Topology})$	2	0.000105	0.000052	0.13	0.882
Topology	2	0.001235	0.000617	1.49	0.237
Topology* $\lambda$	2	0.001137	0.000568	1.37	0.265
$\lambda*A(\text{Topology})$	2	0.000879	0.000440	1.06	0.355
$A(\text{Topology})*t(\text{Topology}, \lambda)$	4	0.001494	0.000373	0.90	0.472
Error	40	0.016554	0.000414		
Total	59	0.051390			

For a deeper analysis on how each element in the model affects the response variable, a comparison between two groups of each element was made using the Tukey method to compute a 95% confidence interval of the difference of means. The Tukey method compares paired groups of factor levels while controlling the simultaneous confidence level. The results of this test are plotted in figure 4.17, a. contains the 95% confidence interval of the difference of  $\lambda$  10-5, being positive indicates that samples of  $\lambda = 10$  mm have higher conformability ratio. The plot in figure 4.17 b. presents the same comparison with parameter  $t$ , only the comparisons that are statistically different (i.e. those that do not contain zero in the confidence interval) are presented. Here it is observed that, when comparing thin and thick samples, thin samples have higher conformability ratio, regardless of the topology or  $\lambda$ .

In these results, comparing all the types of topology together, six samples present a conformability ratio above the mean, five of which correspond to the parameters  $\lambda = 10$  mm, and  $t = 0.5$  mm, all with an approximate value of relative density  $\bar{\rho} = 0.1$  (figure

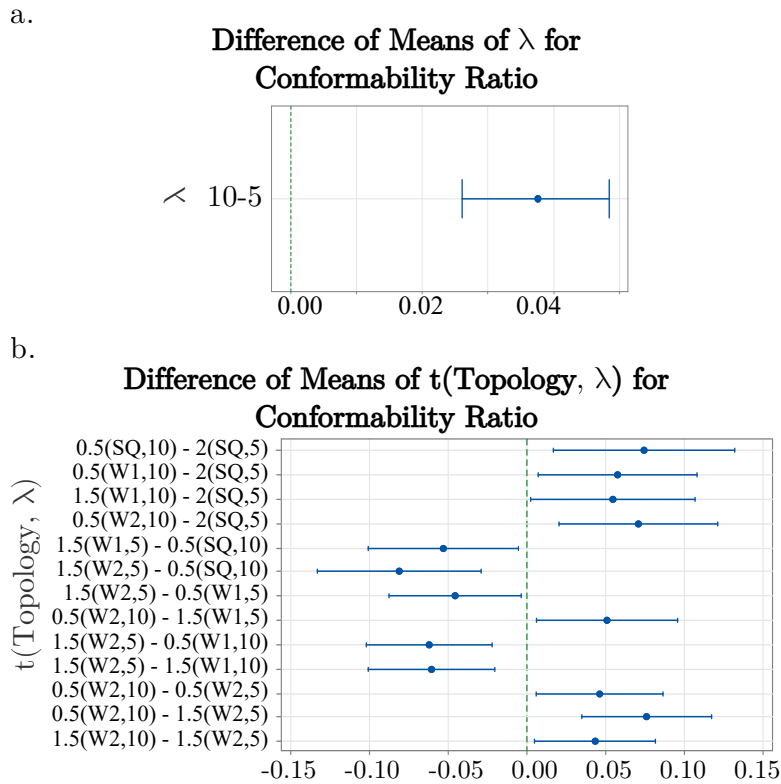


Figure 4.17: Simultaneous 95% confidence intervals comparison of means of the factors a. Length of the unit cell  $\lambda$ , and b. Thickness  $t$  that belongs to specific Topology and  $\lambda$   $t(\text{Topology}, \lambda)$  for the conformability ratio of all the samples tested. If an interval does not contain zero, the corresponding means are significantly different.

4.18a.) and high flexibility ( $k$  around 250 N/mm). The other topology corresponds to W1, with  $\lambda = 10$  mm,  $t = 0.5$  mm, and  $A = 0.5$  mm (figure 4.18b.), in comparison with the other grouped topologies, this is around 6 times stiffer, meaning it takes more force to conform the same as the others. It also is 10% more dense, allowing it to have more material touching the sphere. All these topologies are auxetic, except for the square lattice.

Moreover, it was found two groups with similar results of conformability ratio, the group with parameters  $\lambda = 5$  mm and  $t = 0.5$  mm (figure 4.19a.), and the other of  $\lambda = 10$  mm and  $t = 1.5$  mm (figure 4.19b). The difference in  $\bar{\rho}$  is only 10%, while the densest group is 3 times stiffer. Moreover, the samples from this group presented evident plastic



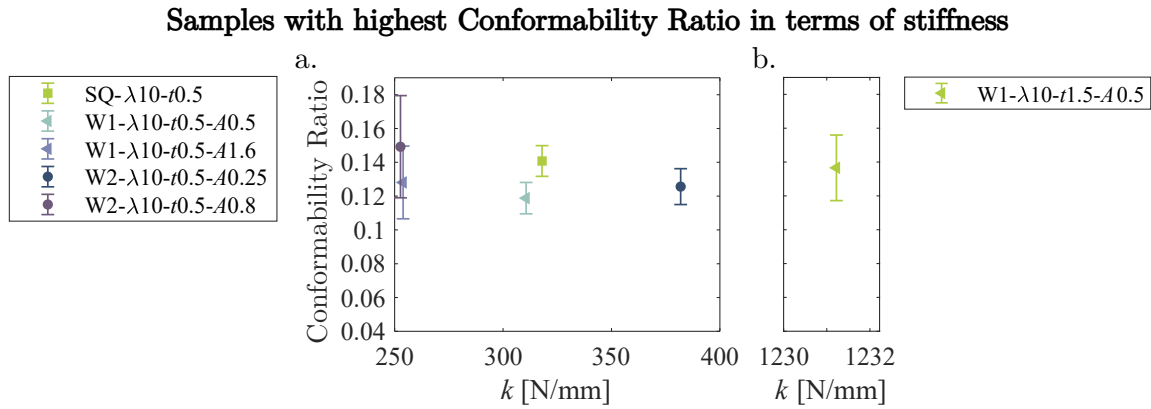


Figure 4.18: Topologies with highest conformability ratio in terms of stiffness, grouped by their relative density a.  $\bar{\rho} = 0.1$ , b.  $\bar{\rho} = 0.28$

deformation after being conformed to the sphere.

**Samples with equivalent Conformability Ratio grouped by relative density**

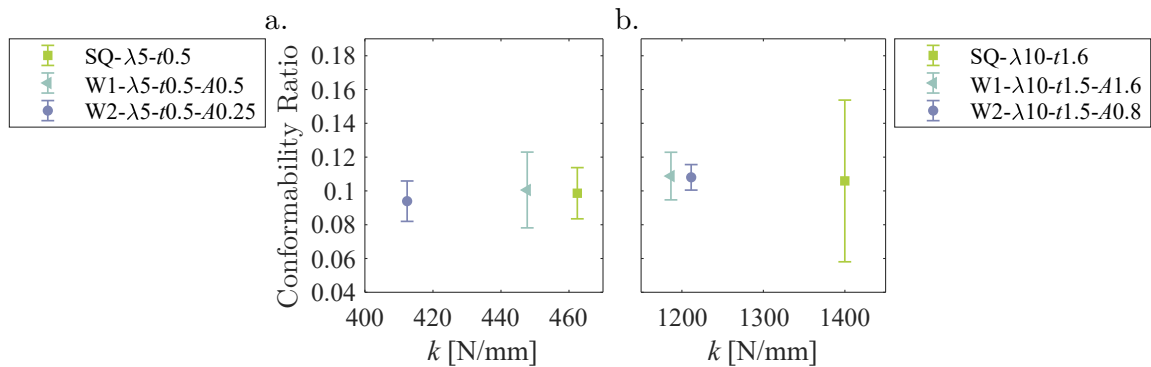


Figure 4.19: Topologies with similar conformability ratio grouped by relative density a.  $\bar{\rho} = 0.19$ , b.  $\bar{\rho} = 0.29$

From the analysis of the square lattice samples tests (ANOVA Table 4.5), it was obtained that only the length of the unit cell  $\lambda$  had an effect on the conformability ratio. Note from figure 4.20, that all the samples together, samples with  $\lambda = 10$  mm had higher conformability ratio.

On the analysis of the topology W1 samples, the ANOVA Table 4.6 indicates that

Table 4.5: Analysis of variance table of the analysis of the square lattice samples tests.

Source	DF	Adj SS	Adj MS	F-Value	P-Value
$\lambda$	1	0.002661	0.002661	5.80	0.043
$t(\lambda)$	2	0.003258	0.001629	3.55	0.079
Error	8	0.003668	0.000458		
Total	11	0.011761			

Difference of Means of  $\lambda$  for Conformability Ratio of Square Lattice Samples

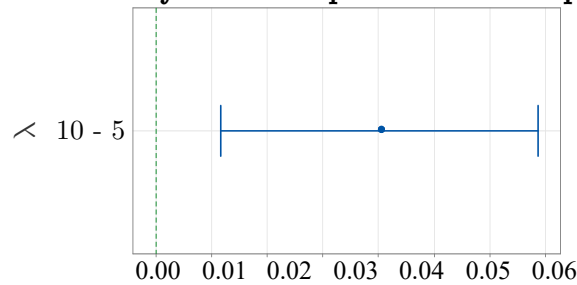


Figure 4.20: Simultaneous 95% confidence intervals comparison of the means of Length of the unit cell  $\lambda$  for the Conformability Ratio of square lattice samples tested. If an interval does not contain zero, the corresponding means are significantly different.

none of the factors have an effect on the conformability ratio, therefore there was not performed a comparison test.

Table 4.6: Analysis of variance table of the analysis of the topology W1 lattice samples tests.

Source	DF	Adj SS	Adj MS	F-Value	P-Value
$\lambda$	1	0.000500	0.000500	0.97	0.339
$t$	1	0.000404	0.000404	0.79	0.388
$A$	1	0.000281	0.000281	0.55	0.471
$\lambda*t$	1	0.000877	0.000877	1.71	0.210
$\lambda*A$	1	0.000014	0.000014	0.03	0.869
$t*A$	1	0.000066	0.000066	0.13	0.724
$\lambda*t*A$	1	0.000288	0.000288	0.56	0.465
Error	16	0.008228	0.000514		
Total	23	0.015297			

Finally, from analyzing W2 samples it was observed that  $\lambda$  and  $t$  affect the conformability ratio, given the P-Values smaller than  $\alpha$  in Table 4.7. From inspecting figure 4.21, it was also found that samples with  $\lambda = 10$  mm present higher conformability ratio (figure 4.21a.), the same case with thinner samples (figure 4.21b.). Comparing these results with the characterization of Poisson's ratio, it was included the comparison of the interaction thickness and amplitude  $t^*A$ , given that two of the three resulting auxetic samples belong to the parameters  $A = 0.8$  mm and  $t = 0.5$  mm (figure 4.21c). In this plot it is observed that the only significant differences are obtained when comparing this combination with non-auxetic samples, and that these samples have statistically significant higher conformability ratio.

Table 4.7: Analysis of variance table of the analysis of the topology W2 lattice samples tests.

Source	DF	Adj SS	Adj MS	F-Value	P-Value
$\lambda$	1	0.001506	0.001506	5.17	0.037
$t$	1	0.001310	0.001310	4.50	0.050
$A$	1	0.000023	0.000023	0.08	0.781
$\lambda^*t$	1	0.000096	0.000096	0.33	0.574
$\lambda^*A$	1	0.000569	0.000569	1.95	0.181
$t^*A$	1	0.000000	0.000000	0.00	0.989
$\lambda^*t^*A$	1	0.000203	0.000203	0.70	0.416
Error	16	0.004659	0.000291		
Total	23	0.023097			

When analyzing the conformability ratio results it was also found that increasing the amplitude of the samples in both sinusoidal topologies, there is an increase in relative density  $\bar{\rho}$ , which is encountered in less magnitude for topologies made from thin, big unit cells. This while maintaining a similar conformability ratio and reducing stiffness, (illustrated in figure 4.22a. for topology W1 and b. for topology W2).

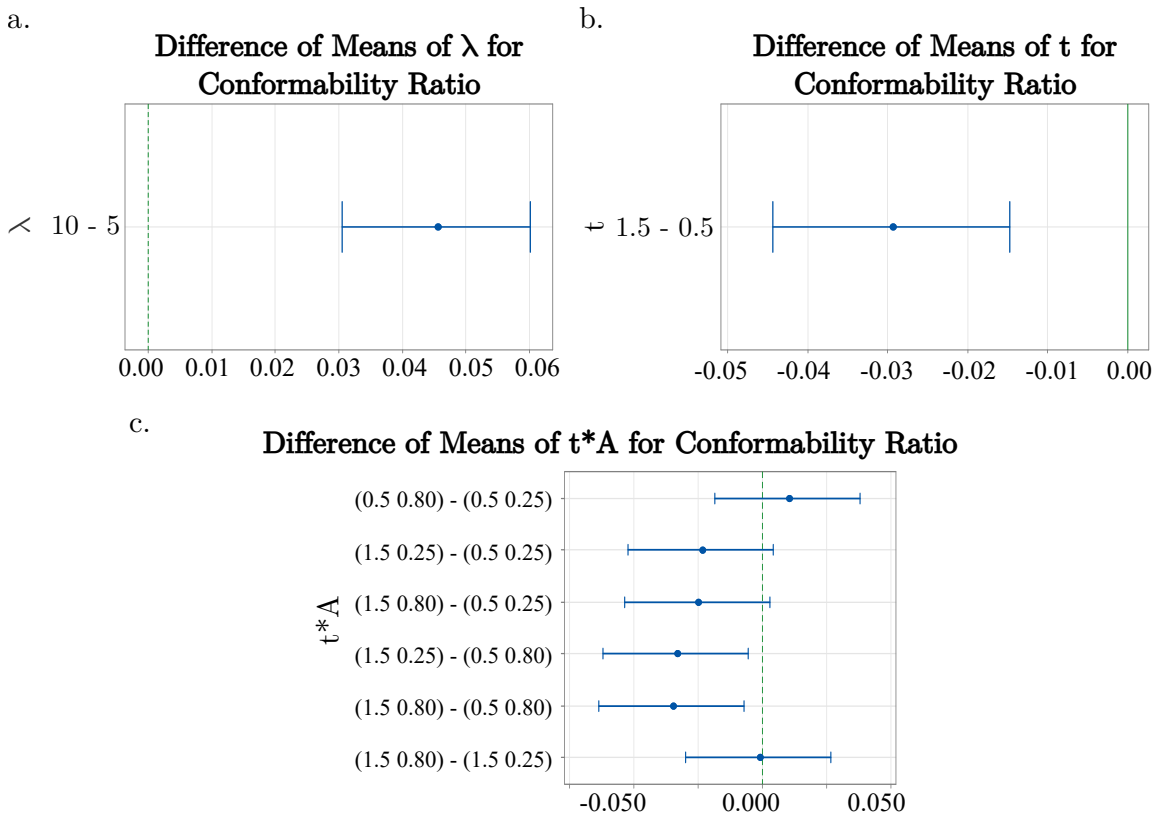


Figure 4.21: Simultaneous 95% confidence intervals comparison of means of the factors a. Length of the unit cell  $\lambda$ , and b. Thickness  $t$ ; and c. The interaction of amplitude and thickness  $A*t$ , for the conformability ratio of all the topology W2 samples tested. If an interval does not contain zero, the corresponding means are significantly different.

### 4.3 Summary

In the characterization of the out-of-plane stiffness of the samples it was found that  $t$  affects the most, regardless of the other parameters and type of topology. In general, when comparing the types of topology with the same parameters, it was found that topology W2 is the most flexible, and the square lattice is the stiffest. Which is an indication that adding a value of  $A$  different from zero to the square lattice result in more flexible samples, even though this parameter increases relative density. Moreover, it was found that around 28% of the error is attributed to manufacturing issues, such as obtaining 3D samples with thicker features than the intended CAD ones.

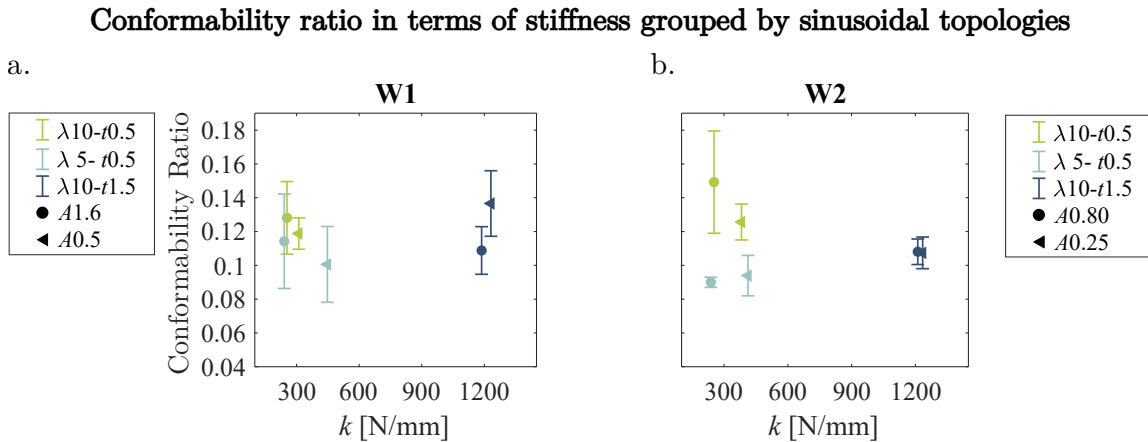


Figure 4.22: Topologies with similar conformability ratio in terms of stiffness grouped in colors by parameters  $\lambda$  and  $t$  of lattices with topology a. W1, and b. W2. Amplitude  $A$  values are identified by different markers.

The conformability ratio results were analyzed statistically using Minitab, comprehended by an analysis of variance performed with a generalized linear model with a 95% confidence interval, and a comparison test using the Tukey method using a simultaneous 95% confidence interval. In this analysis was found that the parameter that had an effect on all the topologies' conformability ratio was  $\lambda$ , in which topologies with  $\lambda = 10$  mm performed better. Meanwhile, specifically with the analysis of topology W1, none of the other parameters seemed to affect conformability. On the other hand, for topology W2, apart from  $\lambda$ ,  $t$  also affects the response, and was found that, when comparing the pairs of  $t \cdot A$ , the only significant differences are obtained when comparing the samples with  $A = 0.8$  mm and  $t = 0.5$  mm, which correspond to two of the three auxetic samples of this topology.

Finally, doing an analysis of the raw results of conformability ratio, it was found that the topology with highest conformability ratio (W2- $\lambda=10$ - $t=0.5$ - $A=0.8$ ) is one of the most flexible and porous. Meaning that it conforms at a very low magnitude of force, covering a wide area but not having many material in contact with the target surface. If wanting to increase the amount of material touching the target surface, increase relative density could be explored, as the case of the topology W1- $\lambda=10$ - $t=1.5$ - $A=0.5$ , which has only 1% less conformability ratio with 10% higher relative density, however, it requires around six

times more force to get to the same conformability, presenting plastic deformation after the test. One needs to be aware that despite having similar conformability ratios, a relation to the stiffness is needed. Increasing the amount of material needed to be in contact with the target surface will increase the stiffness without affecting significantly the conformability ratio.

## Chapter 5

# Auxetic pressure sensor: fabrication and electric response under mechanical loading

The most common pressure sensors are capacitive, resistive, piezoelectric and piezoresistive sensors. Piezoresistive sensors can be fabricated using flexible materials, one of these materials is Velostat, which is a conductive sheet impregnated with carbon black sensitive to pressure, torsion and bending. By applying force causes conductive particles to touch, increasing the current through the material, thus decreasing its resistance.

One of the applications of pressure measuring devices are in-socket pressure sensors. They are used to evaluate the pressure distribution of prosthetic sockets, which in turn allow to make personalized adjustments, thus preventing tissue damage in patients.

This chapter is structured as: electric characterization of the material in section ??, the fabrication method and instrumentation of the sensors in section 5.2, the static measurement of electric resistance reported in section 5.3, the electric response under two types of loads (tension and out-of-plane) presented in section 5.4, the velostat with cellular patterns evaluated in-socket in section 5.5, and main remarks are summarized in section 5.6.

## 5.1 Electric characterization of velostat

Velostat is a commercially available conductive sheet impregnated with carbon black. This material is sensitive to flexion and its inner resistance reduces with applied pressure. According to Steren, its maximum volume resistivity (specific electrical resistivity) is  $500 \Omega\text{-cm}$  and surface resistivity of  $31\,000 \Omega/\text{cm}^2$ . An electric static and dynamic characterization was performed to Velostat before implementing the cellular periodic arrangements. From the electric static tests its repeatability, linearity, sensitivity and hysteresis were evaluated. The dynamic characterization was used to evaluate its frequency response. The specifications of the experiment tests and the results are described in this section.

### 5.1.1 Instrumentation and data acquisition

A piece of velostat was cut from one of the sheets to be characterized. Its electrical resistance was measured between opposite faces of the material with a Truper MUT-39 multimeter, first without any applied load, then with a load of 1 kN. The average of three repetitions gave a change in resistance from  $488 \Omega$  to  $57 \Omega$ . A voltage divider circuit with a resistance of  $220 \Omega$  (illustrated in figure 5.1) was implemented to convert the resistance measurements to voltage.

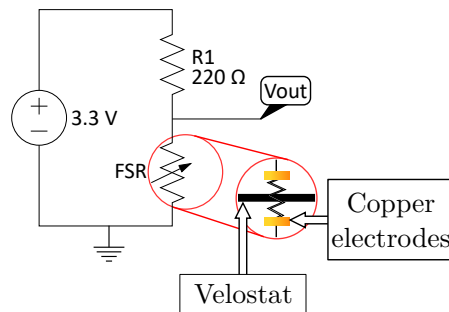


Figure 5.1: Schematic of the voltage divider circuit for data acquisition, FSR is the force sensing resistor (sheet of conductive material).

This signal went to an analogue to digital converter (ADC) input of the microcontroller Arduino UNO for data acquisition, also used for power supply. Data storage and



visualization was performed with a program developed in National Instruments system-design platform, LabVIEW, as illustrated in figure 5.2.

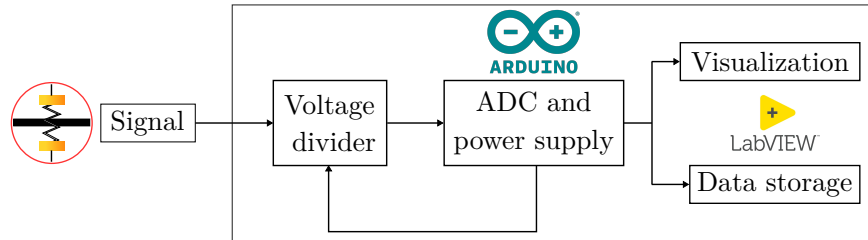


Figure 5.2: Schematic diagram of the data acquisition and storage.

### 5.1.2 Electric static characterization of velostat

The static response (measurement of the stabilized response on its steady state) of the material was evaluated with different weight loads in a range of 1 to 10 N in steps of 1, and 10 to 75 N in steps of 10. The loads were applied using the TVT 6700 texture analyzer. The electrode was compressed using a 1" cylindrical probe (figure 5.3). A piece of foam was placed over the support of the texture analyzer, the piece of velostat was placed on top of the foam, and the target load was set on the TexCal 5 software. Once it reached the target load, it held its position 5 seconds and three repetitions of each load were performed. An example of the complete data acquired is shown in figure 5.4, in this plot is marked the fraction of the data used to calculate an average of the voltage measurements to ensure that the reading corresponded to its steady state.

In figure 5.5 a. are presented the results of the force-voltage characterization. A curve was approximated to the data using the Curve Fitting tool from Matlab, this corresponds to the equation:

$$f(x) = 9.733x^{-0.04223} - 7.028. \quad (5.1)$$

From this equation is inferred that the response is not linear and the sensitivity that corresponds to -0.04223, i.e. an increase in load, decreases the voltage. In figure 5.5 b. is presented the standard deviation of the measurements in each load. It is noted the narrowing of the standard deviation with increased load. The maximum standard deviation

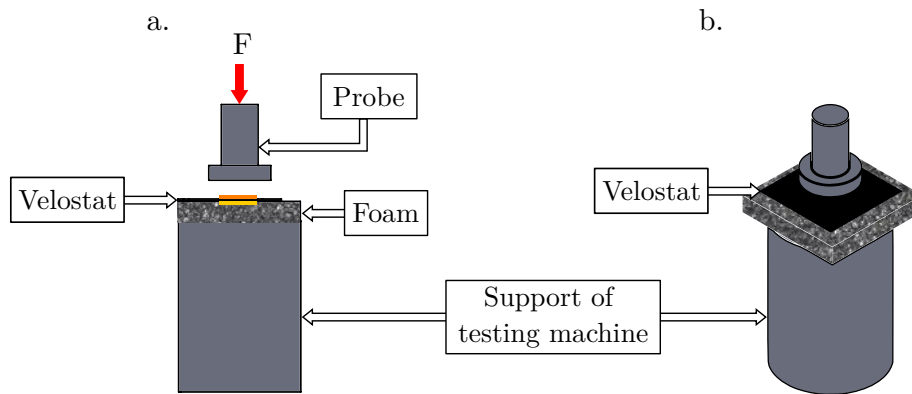


Figure 5.3: Experimental setup of the static characterization applying the load  $F$  to the velostat. a. Frontal and b. Isometric views.

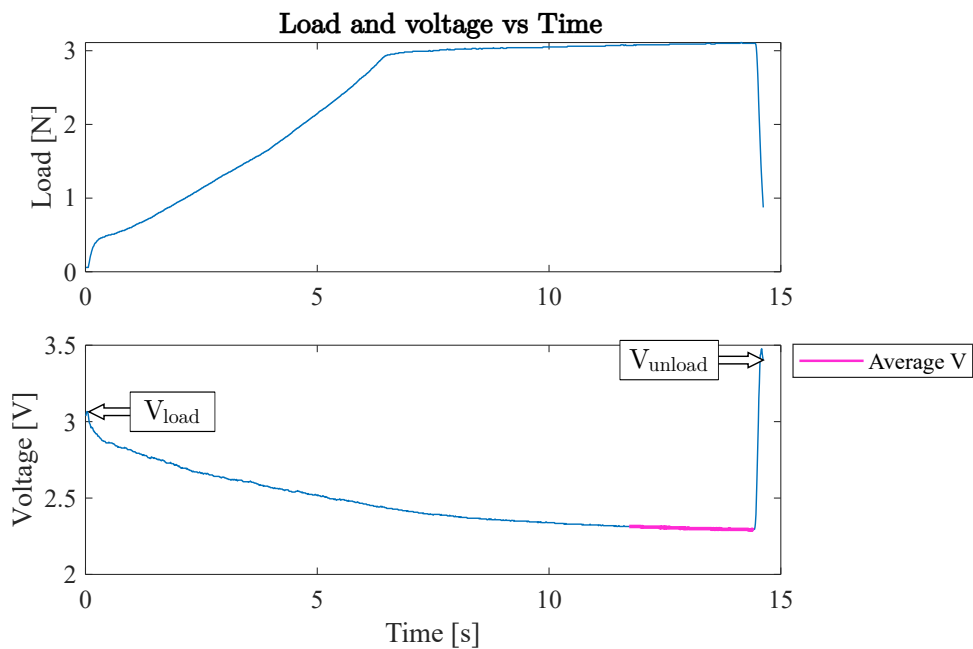


Figure 5.4: Example plot of Voltage and load in terms of time owith an applied load of 3N. It is highlighted the fraction sample from which it was obtained the steady state measurement.

corresponds to the smallest load (1 N) with 0.23 V.

Finally, from this data was obtained the hysteresis of the material from computing the difference of voltage in loading  $V_{load}$  and unloading  $V_{unload}$  conditions (illustrated in

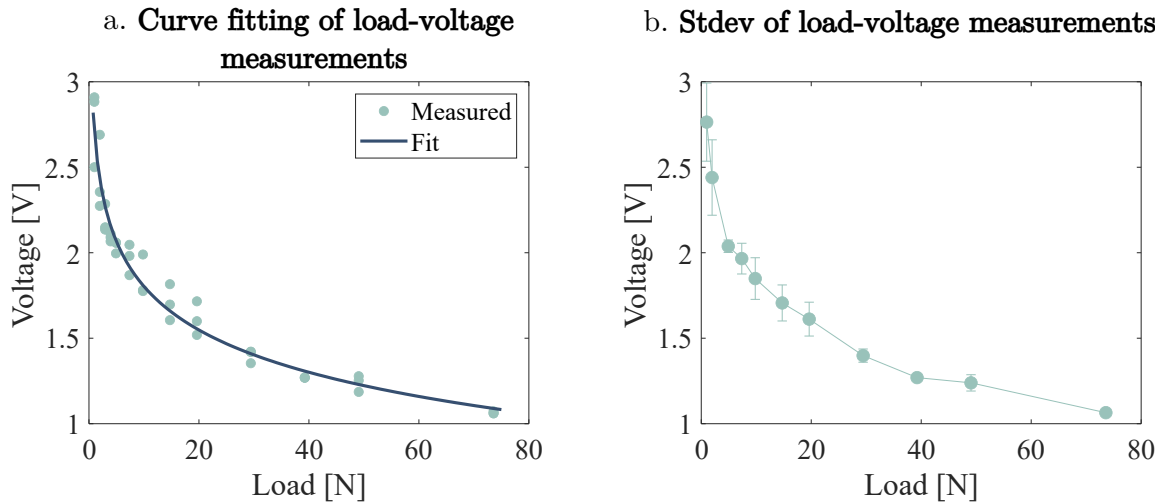


Figure 5.5: Static characterization data illustrating a. an approximation of a fitted curve to the data and b. the standard deviation of the measurements in each load.

figure 5.4), in terms of the full range tested, as presented in the next equation:

$$Hysteresis\% = \frac{|V_{load} - V_{unload}|}{V_{max} - V_{min}}. \quad (5.2)$$

Where  $V_{max}$  is the maximum load tested (7.5 N) and  $V_{min}$  is the minimum load (0 N). An average of 10 measurements taken computed a hysteresis of 5.14%.

### 5.1.3 Electric dynamic characterization of velostat

This test was performed using the same experimental setup as illustrated in figure 5.3. This test consisted of 10 cyclic loads of 10 N at a rate of 0.5 mm/s with no pause between cycles. The data from this test was used to get a transfer function (TF) using the applied load from the texture analyzer data as the input and the voltage stored with LabVIEW as the output of the system. Both sets of data were measured at a 100 points per second rate (sample time 0.01 s). Using the Matlab System Identification toolbox, a series of transfer functions were simulated and compared. The best fit was a 3 poles and 3 zeros TF with 90.05% fit for Cycle 1 and 91.78 % in the TF simulated for Cycle 10. In figure 5.6 are illustrated the simulated TF and the measured data of the first and tenth cycles.

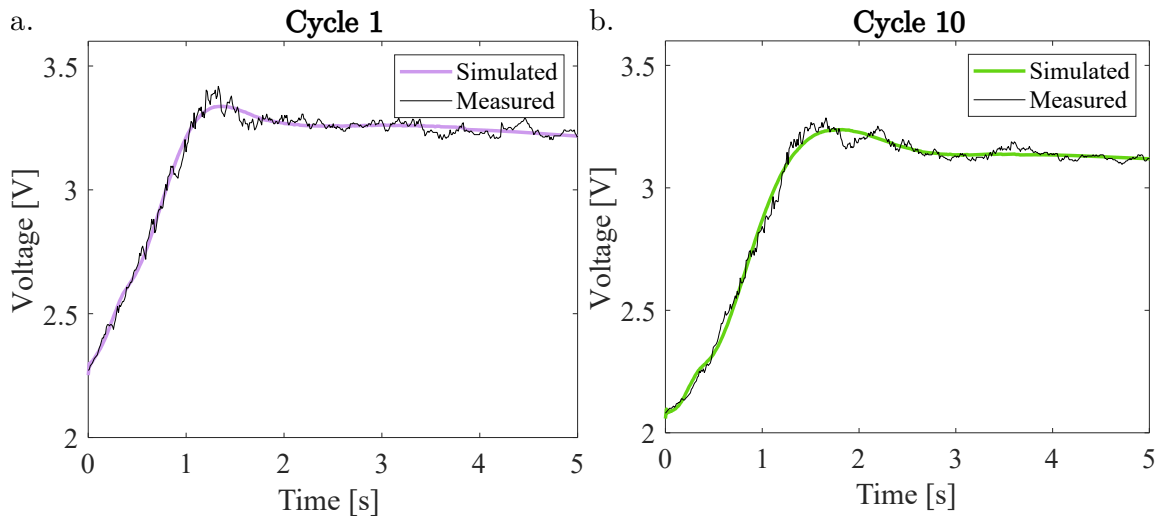


Figure 5.6: Measured and simulated model output from transfer function of a. Cycle 1 and b. Cycle 10.

From these transfer functions the amplitude bode plots were obtained (illustrated in figure 5.7). It is observed that a sensor fabricated using this material would respond better with low frequencies.

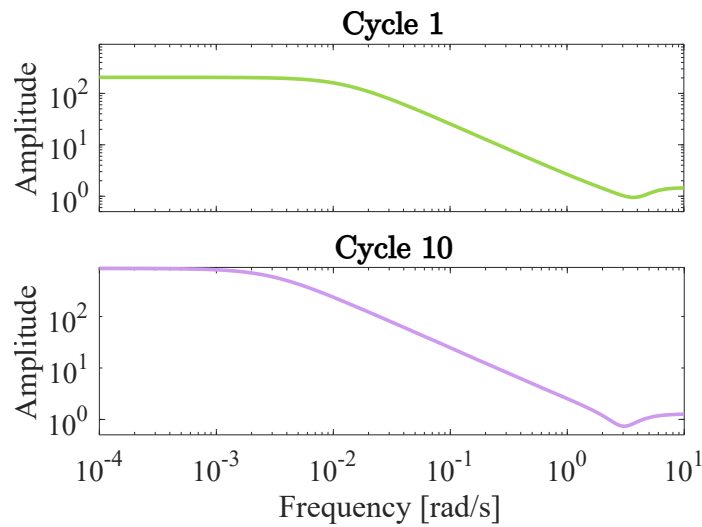


Figure 5.7: Amplitude bode plots of Cycles 1 and 10.

## 5.2 Fabrication of sensing samples: geometries and instrumentation

For the fabrication of pressure-sensing samples five different geometries were chosen to implement them into the conductive material, the specifics of fabrication and instrumentation of the devices are described in this section.

### 5.2.1 Auxetic cut patterns geometries

Two sinusoidal topologies were chosen from the previously studied (Chapter 4). The ones with high relative density were selected in order to have enough area to be able to place electrodes for the sensing device fabrication. Trials were performed to cut the material using the laser cutting machine, the smallest unit cell that could be fabricated was 12 mm. Therefore, the topology W1 with  $\lambda = 5$  mm,  $t = 1.5$  mm, and  $A = 1.6$  (figure 5.8a.) and topology W2 with  $\lambda = 5$  mm,  $t = 1.7$  mm, and  $A = 0.8$  (figure 5.8b) were chosen. Both were scaled 3 times to get a unit cell size of 15 mm.

In order to evaluate the sensing performance of the sinusoidal pattern, these were compared with other auxetic structures found in the literature [24][35][25]. These are the rotating square with rectangular cuts [24](figure 5.8c.), a pattern with rectangular perforations [35](figure 5.8d.), and the rotating triangle [25](figure 5.8e). The parameters and dimensions employed here are listed in Table 5.1, along with the relative density.

Table 5.1: Dimensions of the periodic cut samples

Pattern	$a$	$s$	$\theta$	$b$	$h$	$\bar{\rho}$
Rectangular perforations	24	0.8		1.4	12	0.6996
Rotating square	12	1.2		2		0.7708
Rotating triangle	16.5	1.2	15°			0.6923

The unit cell of each topology was repeated to create 20×20 cm samples. These were implemented into the electro-conductive sheets (Velostat) by laser cut of 8 Watts and

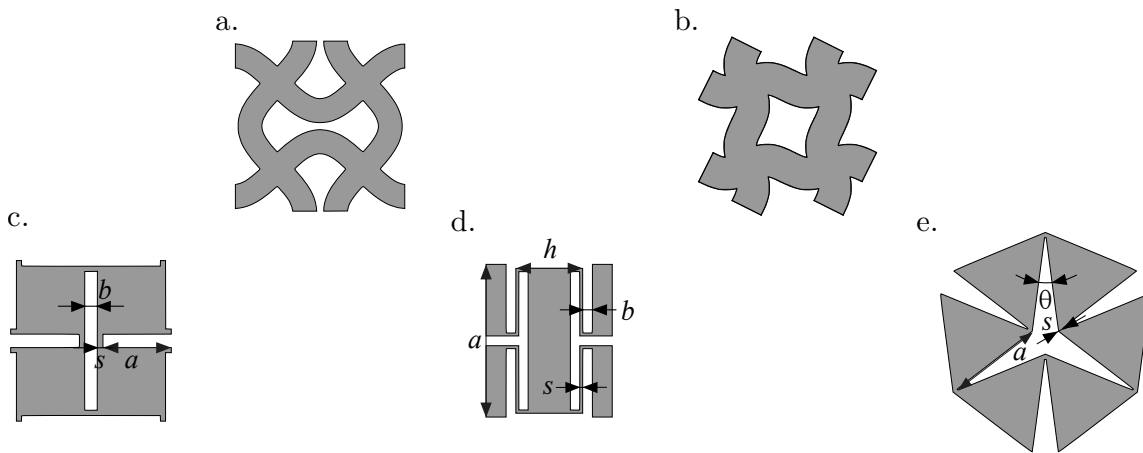


Figure 5.8: Sinusoidal topologies a. W1, and b. W2; and periodic cut patterns geometries with their parameters c. rotating square with rectangular cuts, d. rectangular perforations, and e. rotating triangle for sensing devices samples.

a speed of 150 mm/s. After each sample was finished, it was cleansed to remove powder that was left from the laser.

## 5.2.2 Instrumentation

Five nodes were selected from each sample to paste  $5 \times 5$  mm squares of adhesive copper on each side of the sheet as illustrated in figure 5.9. Each piece of copper was welded to copper cables and to a voltage divider (as the one illustrated in figure 5.1), which made an individual force sensing resistor (FSR). The output voltage of each FSR was connected to an analogue pin of an Arduino UNO for the data to be processed, visualized and saved by a program developed in National Instruments system-design platform, LabVIEW as illustrated in the diagram of figure 5.2. The circuit schematic of the complete sensor is presented in figure 5.10

These nodes were selected to analyze the electric response on different places of the sample. Apart from pressure, they were evaluated under tension and out-of-plane loading, since the conductive material is also sensitive to flexion. These tests are described in the next sections of this chapter.

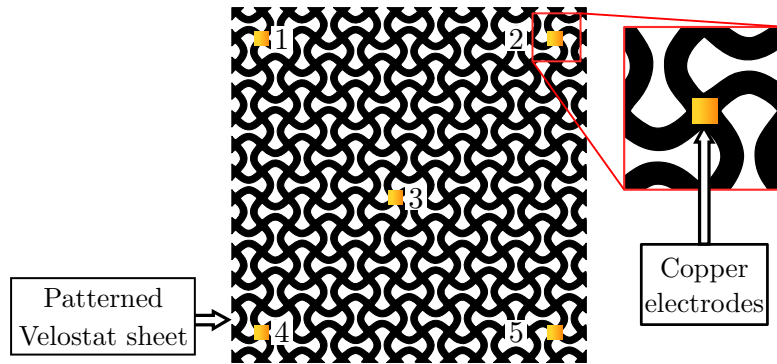


Figure 5.9: Adhesive copper pasted on each node (labeled) for electric measurements. Each node corresponds to a FSR that goes to a voltage divider for data acquisition with an Arudion UNO board and LabVIEW.

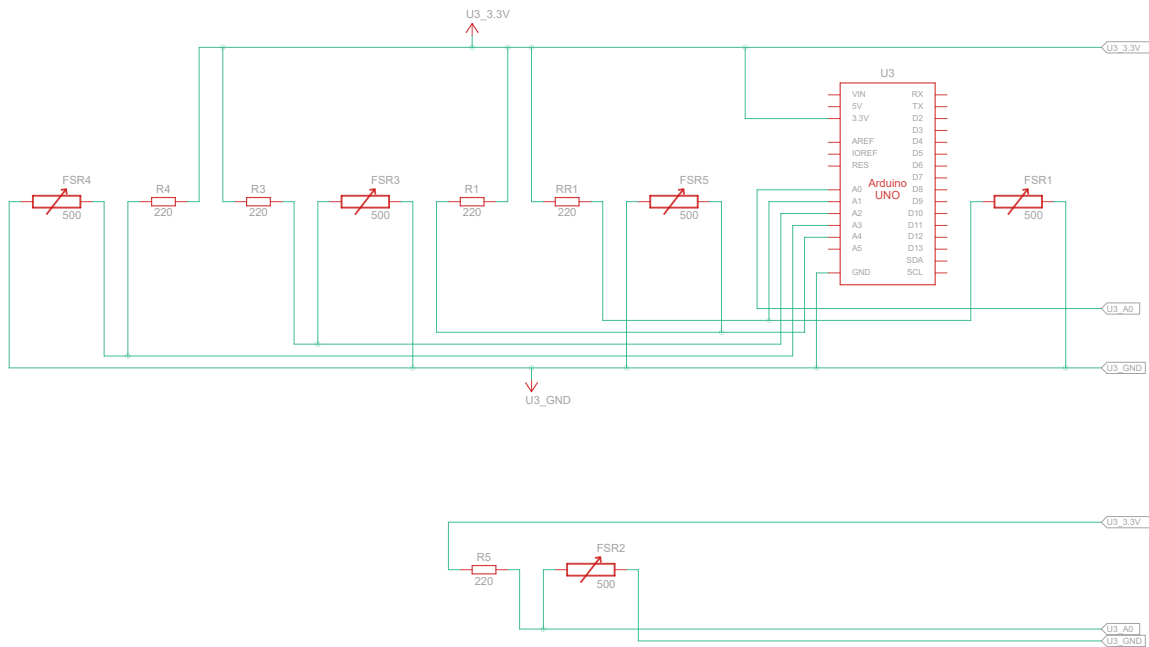


Figure 5.10: Circuit schematic of the 5 FSRs instrumented in each patterned sensor with its corresponding Arduino pin input.

## 5.3 Static measurement of electric resistance with varying loads of velostat based sensors

The static response (measurement of the stabilized response on its steady state) of all FSRs was evaluated with three different weight loads: 10 N, 20 N and 30 N. The specifications of the experiment tests and the results are described in this section.

### 5.3.1 Experimental setup and data acquisition

The loads were applied using the mechanical testing machine Cellscale UniVert, each FSR was compressed using a 1” cylindrical probe (figure 5.3). A piece of foam was placed over the support of the testing machine, the FSR to be tested was placed on top of the foam, and the target load was set on the Cellscale software. Once it reached the target load, it held its position 5 seconds for the 10 N load, 10 and 15 seconds for the 20 and 30 N loads. Three repetitions of each load were performed on each FSR, for which the order was randomized.

An example of the complete data acquired from each load is shown in figure 5.11, all nodes of all samples presented a similar behavior. It is also marked the fraction of data used to calculate an average of the measurements to ensure that the reading corresponded to its steady state.

### 5.3.2 Results and discussion of the steady state electric resistance measurements

The steady state electric resistance for each load was calculated from the output voltage acquired with the Arduino using the equation

$$R_{FSR} = R1 \frac{V_o}{V - V_o}, \quad (5.3)$$

where  $R_{FSR}$  is the value of the resistance of each sensing element,  $R1$  is the serial resistor of the voltage divider (220  $\Omega$ ),  $V_o$  is the output voltage, and  $V$  is the source voltage (3.3



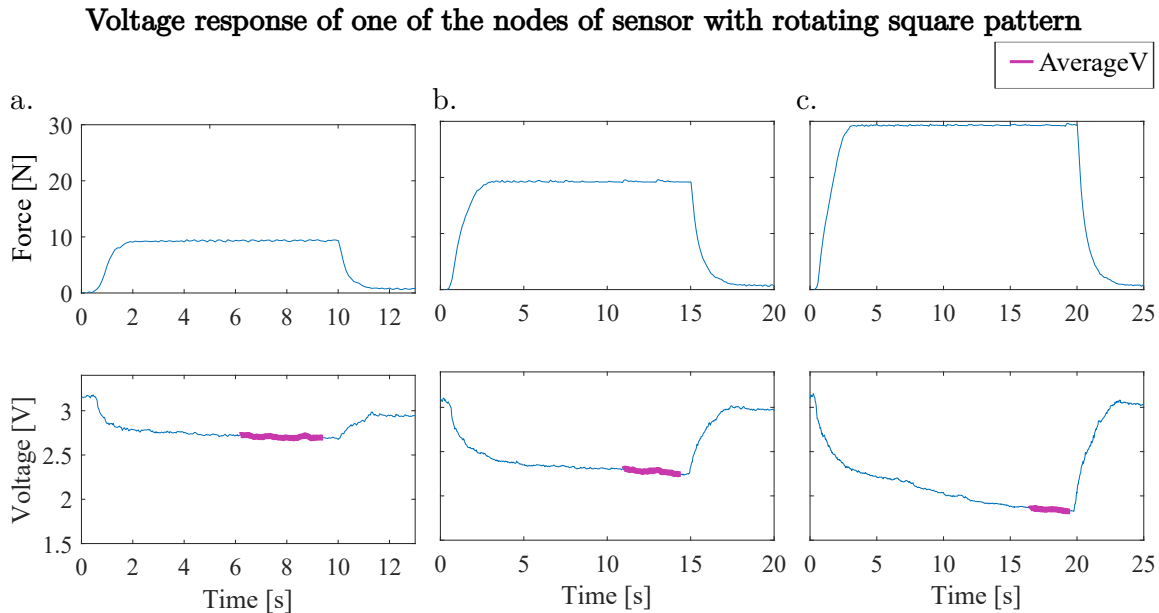


Figure 5.11: Voltage and force in terms of time of tests performed on one of the nodes of the rotating square sensor under different loads: a. 10 N, b. 20 N, and 30 N. It is highlighted on each plot the fraction sample from which it was obtained the steady state measurement average.

V).

No change in voltage was detected in node 3 of the topology W2, node 5 of the rotating square, and node 2 of the rectangular perforations sensors. This indicated that were disconnected during the tests and were not included in the results. The minimum, maximum, mean and standard deviation of the resistance of each FSR of each sample are plotted in figure 5.12. Note a higher variation with the smallest load (10 N), which decreases with higher load. This behavior is consistent with a previous study [16] where it is explained that, when applied high pressure, carbon powder particles get closer, and when this load is too high it is not possible a tighter distribution of the carbon particles. Moreover, the variation between FSRs of the same sensor can be explained with the surface resistivity, which depends on the area in contact of the copper electrodes, same that were manually cut. For instance, the highest measured resistance in topology W1 corresponds to the FSR of node 5 (figure 5.12a.), and the electrode area measured with a digital caliper was of  $19.68 \text{ mm}^2$ , whereas the others varied from  $16.8$  to  $17.28 \text{ mm}^2$ .

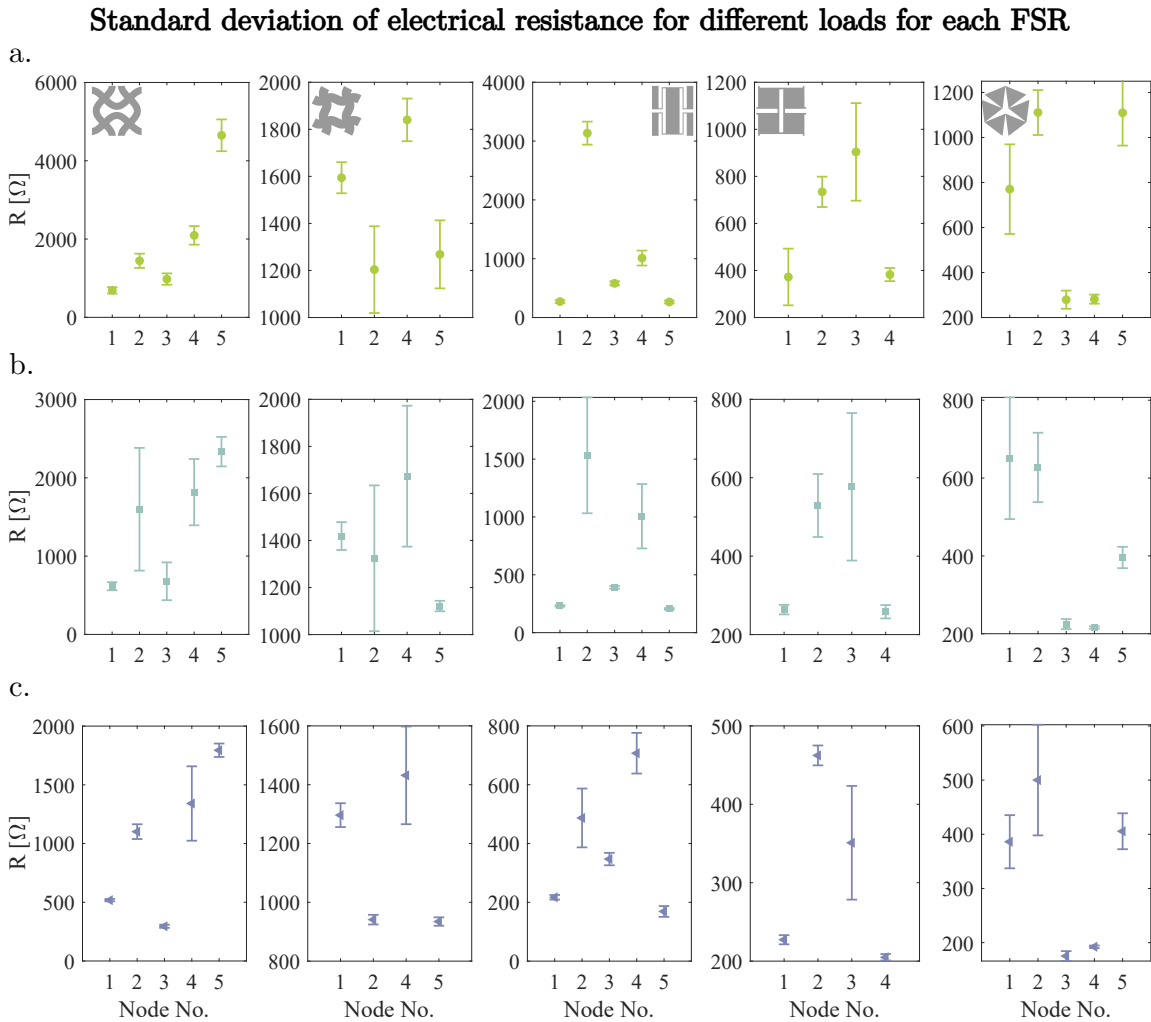


Figure 5.12: Plots of the steady state electrical resistance measured for each sensor, divided by the load applied a. 10 N, b. 20 N, and c. 30 N. Each sensor is presented by column.

The resistance values for each complete sensor were also plotted against the load applied (figure 5.13). These values were calculated with the average of the five FSRs in each sample, where resistance is decreasing exponentially for all samples as the applied pressure increases. Note the narrowing of the standard deviation for higher load (30 N), and a variation of the response between sensors. This could be attributed to the fabrication method, as mentioned before, the laser cut leaves loose carbon powder, concentrating

more material in certain areas of the sheet, therefore increasing the resistance. A relation between the relative density of the samples and the variation of the measurements is observed; higher relative density translates into less material removed, and viceversa. The highest variation of resistance corresponds to the sample with higher porosity (Topology W1 in figure 5.13a), where almost 40% of its material was removed. Furthermore, the smallest variation corresponds to the most dense sample (Rotating triangle in figure 5.13b), where only 23% of its material was removed.

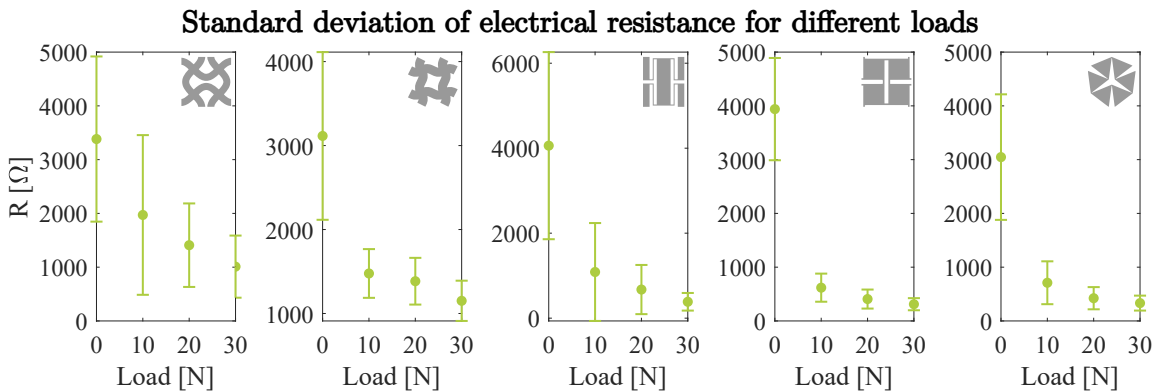


Figure 5.13: Averaged steady state resistance in terms of load of the five FSRs in each sensor.

## 5.4 Response of velostat based sensors under tension and out-of-plane loading

Since velostat is also sensitive to bending, sensors were evaluated under tension and out-of-plane loading, to see whether strain affected the response. The boundary conditions, specifics of the custom manufactured setup and the results from these experiments are described in this section.

### 5.4.1 Boundary conditions and experimental setup

All manufactured sensors went through a tension test using a MTS810 universal testing machine. Custom made PLA clamps were fabricated to hold the samples from its upper

and lower ends, as illustrated in figure 5.14a. The printer used was a Flashforge Creator Pro, with the next printing parameters: thickness layer 0.12 mm, 50% infill, and speed of 50 mm/s. Once the sample was mounted, the lower end had a controlled displacement of 5 mm, which corresponds to a 2.5% strain (figure 5.14b) at a 0.4 mm/s rate.

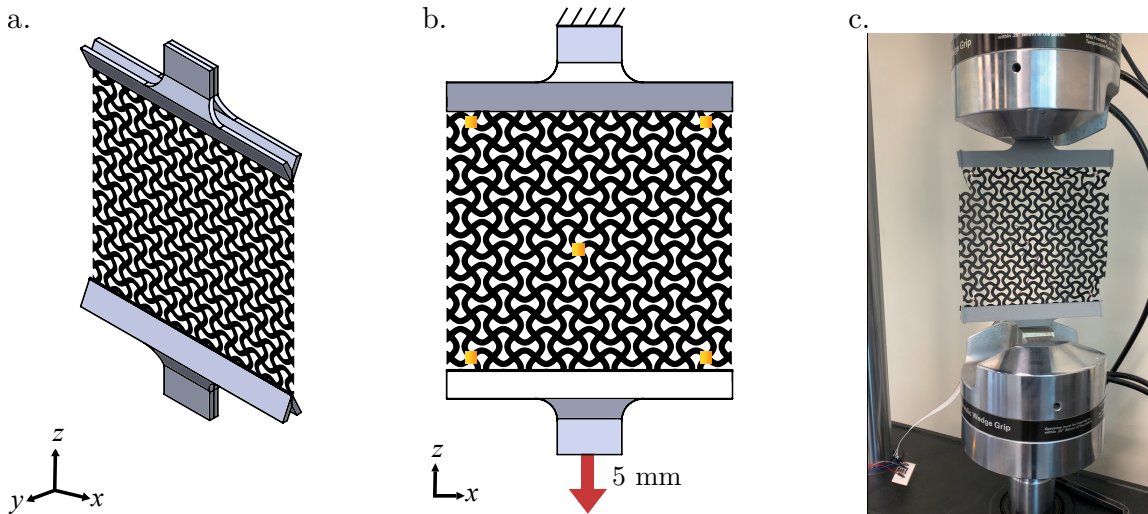


Figure 5.14: Experimental setup of the tensile test: a. Isometric view of the 3D printed clamps to secure the sample, b. Front view and boundary conditions of tensile test, c. Sinusoidal lattice W1 sample mounted on the universal testing machine.

The out-of-plane loading experiment was put together using four pairs of clamps (3D printed with the same material, machine and parameters as before) to hold the corners of the samples (illustrated in figure 5.15a. and figure 5.15b). A controlled displacement of 5 mm along the  $z$  axis was applied to the testing machine support towards a fraction of a 3D printed 10" diameter sphere gripped to the testing machine. In figure 5.15c is presented an image of the setup mounted with the sensor of topology W1.

In both tests, the output voltage of each FSR was measured by the Arduino, this data was visualized and saved with LabVIEW during the test, and was analyzed offline using MATLAB. The electric resistance was calculated from the output voltage using the equation 5.3. There were performed three repetitions of the test on each sample, and no change in force was detected by the machine, so the response was analyzed only in terms of displacement.

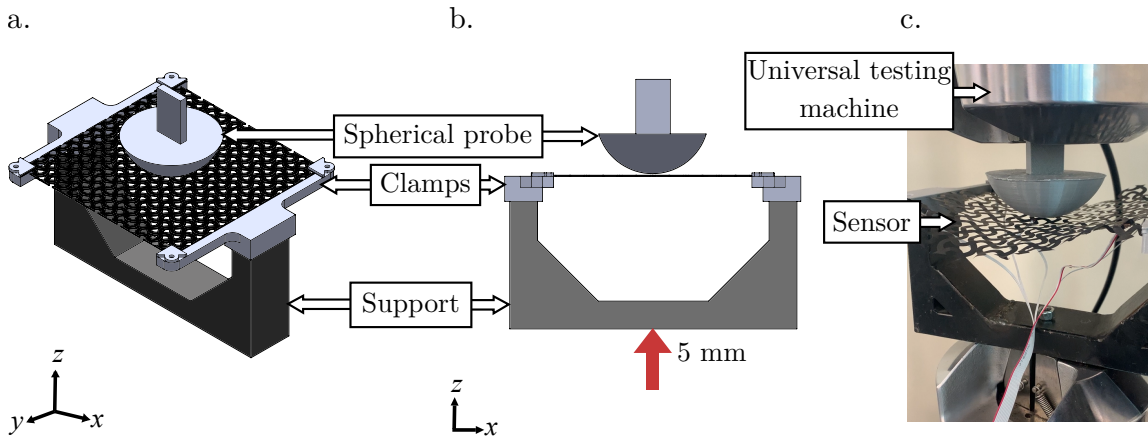


Figure 5.15: Experimental setup of the out-of-plane loading test: a. Front view and boundary conditions of tensile test, b. Isometric view of the 3D printed clamps to secure the sample, and c. Sinusoidal lattice W1 sample mounted on the universal testing machine.

## 5.4.2 Electric resistance results and discussion of sensors subjected to tension and out-of-plane loading

### *Tension experiment*

From inspecting the tensile test it was found that the sensors with topology W2 and topology W1 were the most affected by the load. The comparison between values of resistance was made by calculating the relative resistance with the equation

$$RR = \frac{R_{FSR} - R_o}{R_o} * 100\%, \quad (5.4)$$

where  $R_{FSR}$  is the measured resistance and  $R_o$  is the resistance without any loading. The former had a maximum relative resistance of 280%, and the latter 56%. While sensors with the cutting patterns had maximum relative resistance of 20%. In figure 5.16a. is presented the plot of the topology W2 sensor's response for each FSR with respect to time, where it is noted the clear change in resistance when the load is applied. In figure 5.16b. is plotted this response for the sensor with the rotating square pattern, where minor variations are observed. In both plots is present, first, a change of resistance in the FSRs on the bottom (where displacement is applied), then in the FSRs on the top. Additionally,

there is a minimal change in the central node, which is the one located furthest from the edges, hence, boundary conditions.

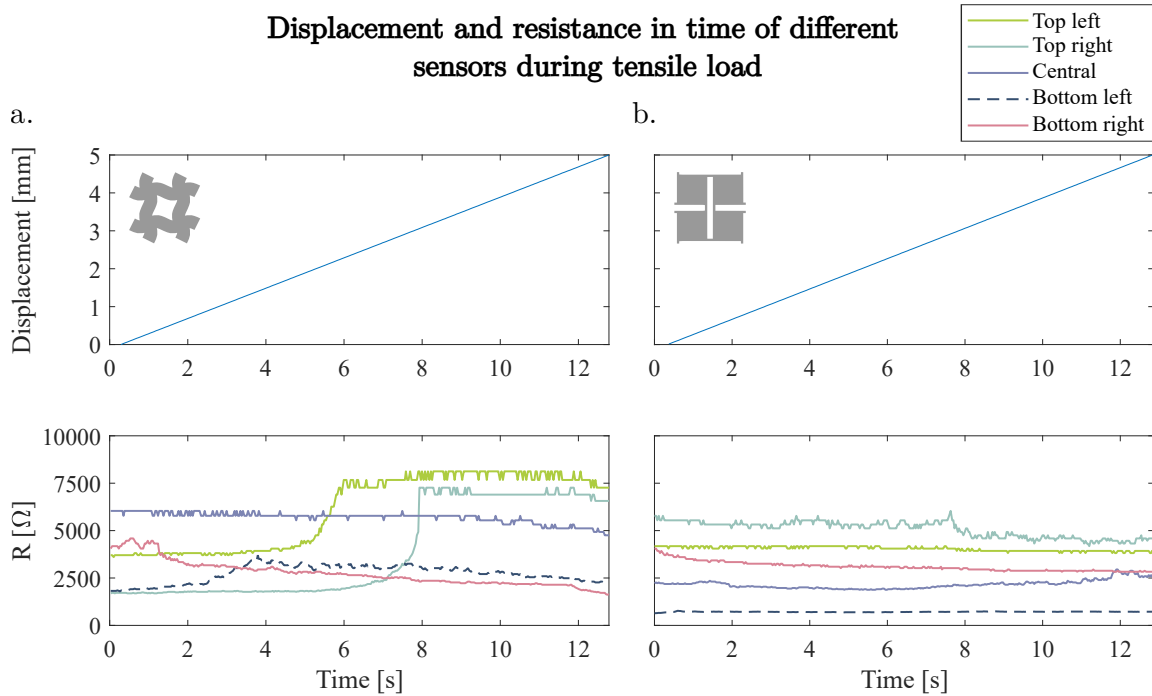


Figure 5.16: Displacement and resistance response of the sensors of a. Topology W2 and b. Rotating square pattern during tensile loading. Each line corresponds to a FSR and is identified by the position in the sensor.

The main difference between sinusoidal based topologies and the cutting patterns is the deformation mechanism. Pictures of an electrode of the former during the test are presented in figure 5.17a. Here it is observed the change from no applied load (figure 5.17a.1.) to the produced strain due to the stretching of the material (figure 5.17a.2.). Additionally, in figure 5.17b. is presented the sensor with rotating square pattern, showing the rotation of the hinges, which prevents strain in the material in the location of the electrode. Meaning that the material is sensitive to strain, but no clear relation could be established.

#### *Out-of-plane loading experiment*

For this test the sensor with rectangular perforations geometry was not considered,

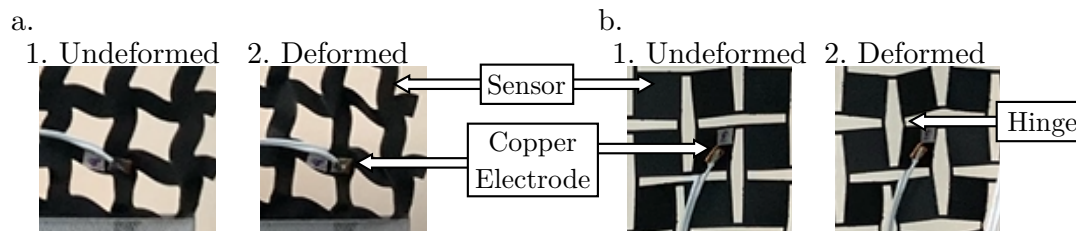


Figure 5.17: Example of the sensors with geometries a. Topology W2 1. before the tensile load, and 2. during the tensile load showing strain on the material; and b. Rotating square, 1. before the tensile load and 2. during the tensile load showing rotation of its hinges.

as it was extremely flexible and could not be held horizontally within the clamps. Because of the horizontal position of the samples and the weight of the electrodes, some FSRs were disconnected during the tests, which were removed from the analysis. All of them corresponded to some corner of the sample and would have a similar response to other corner because of their same distance to the load. Similar results to the ones measured from tensile loading were obtained during this test, no resistance change in the geometries with cut patterns nor in topology W1 caused by the strain of the sensor was detected. Relative resistance values in this FSRs remained below 5%. The sphere applied a direct load to the central FSRs, where changes in resistance went between 16% and 28%. The electrical resistance with respect to time during the test is shown in the plots of figure 5.18 for each sensor. Here it is also observed that the sensor of topology W2 detected strain in its corners, it was obtained a relative resistance of 12% in corner 2, and 56% in corner 3.

## 5.5 Auxetic patterned sensors evaluated in-socket

One of the applications of pressure sensing devices is the assessment of pressure distribution inside prosthetic sockets. This becomes relevant for their design and preventing tissue discomfort and injury in patients [1]. An experimental test to evaluate the performance of the sensors studied as in-socket pressure devices was also performed and the details and results are covered in this section.

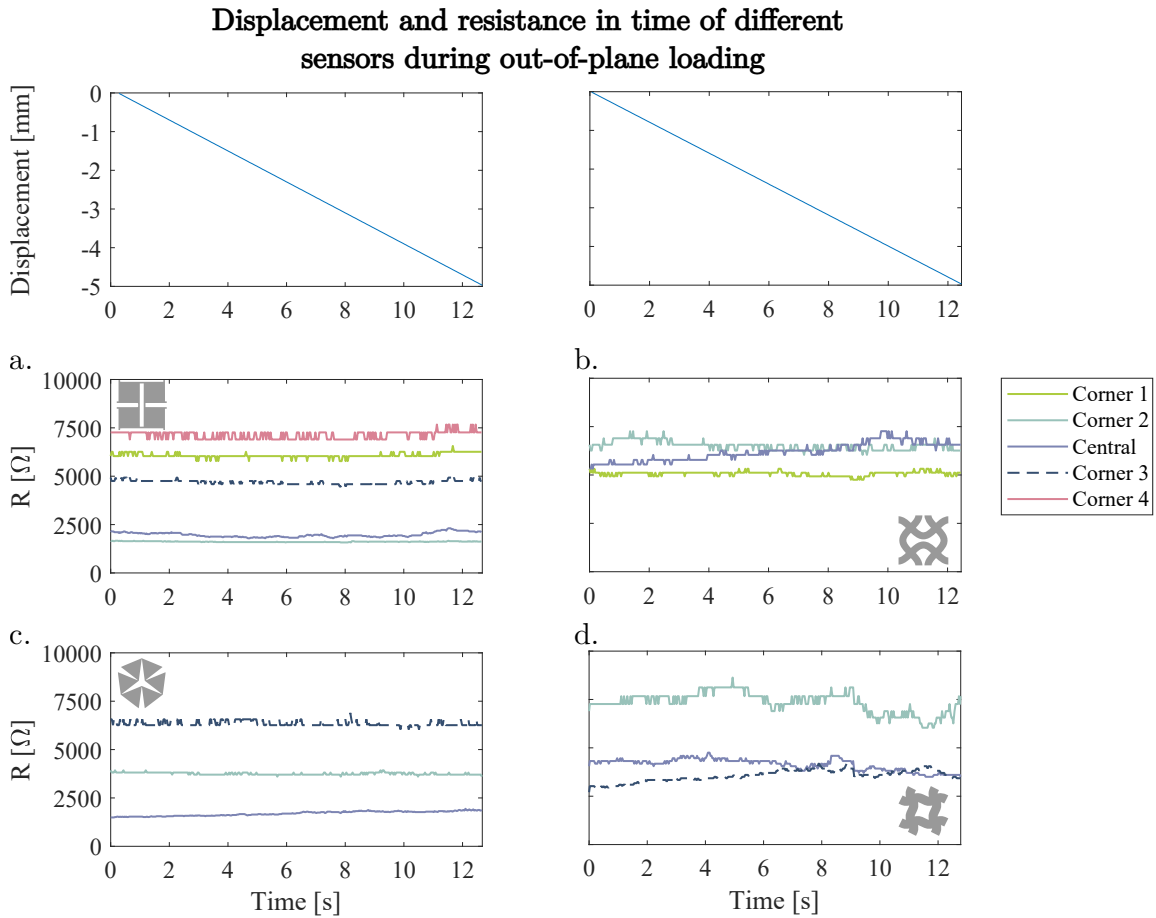


Figure 5.18: Resistance response of the sensors of a. Rotating square, b. Topology W1, c. Rotating triangle, and d. Topology W2 during out-of-plane loading. Each line corresponds to a FSR and is identified by its position.

### 5.5.1 Experiment description

The sensors with topology W1 and rotating square cuts were used to assess pressure exerted between the socket and an artificial residual limb (residuum) of a transtibial amputee's right leg. Six points of interest (illustrated in figure 5.19a., 5.19b. and 5.19c.) were selected to evaluate the pressure exerted from the socket to the residual limb.

According to the geometry of the residuum, 10×28 cm samples were fabricated to ensure having an electrode on all points of interest. The complete sensor was placed over



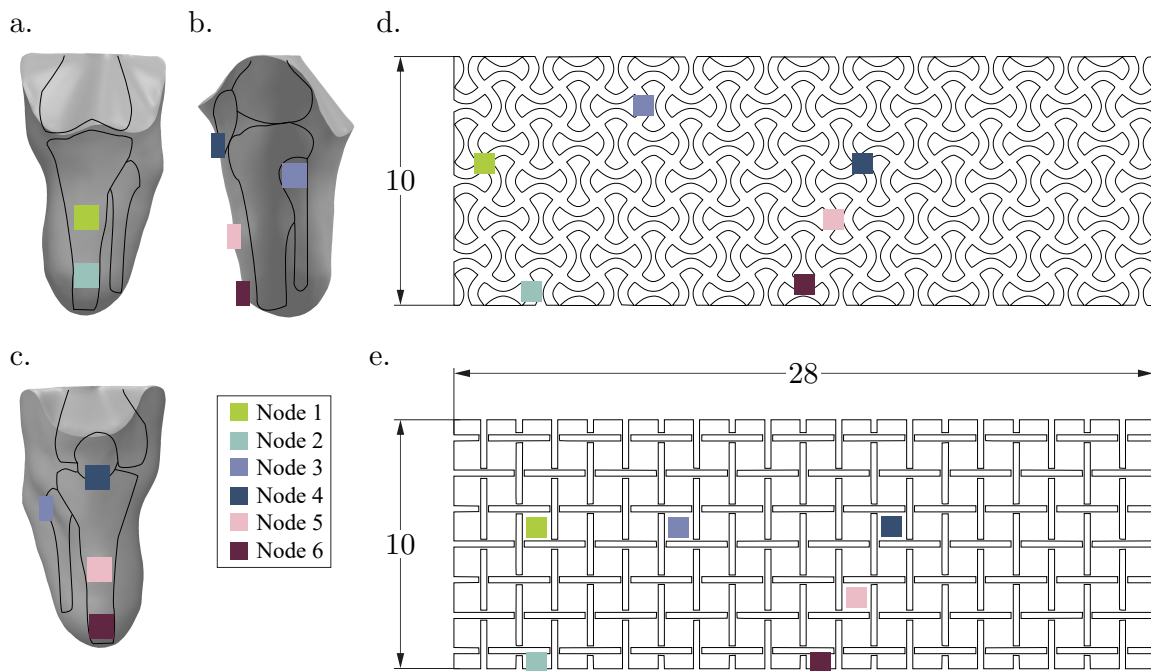


Figure 5.19: Location of the measuring points marked in the artificial residual limb, a. Posterior, b. Lateral and c. Anterior views; and in the sensors' geometries d. Topology W1 and e. Rotating square with their dimensions in cm.

the residuum to locate the points of interest and instrument them as before, with adhesive copper and the voltage divider. The location of the nodes for each device is illustrated in figure 5.19d. and 5.19e., the different locations are because of the deformation needed to conform the residuum.

Once instrumented, the whole sensor was fixed with adhesive tape to the residuum (figure 5.20a. and 5.20b.), and a prosthetic liner was collocated over them to prevent sensor motion inside the socket (figure 5.20c.). The complete implementation was placed inside a prosthetic socket, and a load was applied on top (figure 5.20d.) to simulate a person standing on their prosthesis. Limitations due to the intrinsic properties of the conductive sheets and fabrication method would not allow accurate measurements of physical quantities. Therefore, the objective of the test was to analyze and compare the behavior between both sensors inside the socket. The socket was manually moved towards the floor, process that was iterated three times for each run. Three runs for each sensor ere performed.

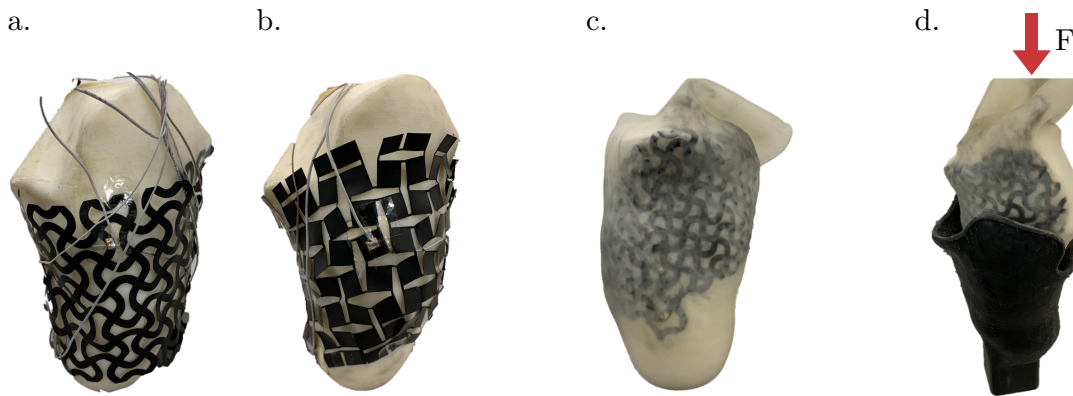


Figure 5.20: Location of the measuring points marked in the sensor samples with geometries a. Topology W1, and b. Rotating square.

Same as the tensile and out-of-plane evaluation, measurement of voltage was done by an Arduino, data visualization and acquisition was done by a LabVIEW during the experiment, and this was processed offline in Matlab to convert data of voltage to resistance using equation 5.3.

## 5.5.2 Results and discussion of in-socket evaluation tests

The plots obtained from the in-socket tests are presented in figure 5.21. Vertical lines indicate the beginning of each iteration, and each run is presented in two plots. These were divided by three measuring nodes for better visualization. The response of the sensor is presented in terms of relative resistance, obtained with equation 5.4, since data of electrical resistance had a large variation. Initial resistance (without load) of the sensor with topology W1 went from 900 to 4 k $\Omega$ , and peak values of 10 k $\Omega$ . On the other hand, the rotating square sensor's initial resistance went from 325 to 1.4 k $\Omega$ , and maximum of 1.8 k $\Omega$ . As mentioned before, variation of initial values of resistance relate to the fabrication method and the size of electrodes.

It can be observed in figure 5.21 that the sensor with the rotating square pattern has a more constant behavior between iterations and runs than the topology W1 sensor. This is explained with the conformability of each pattern to the geometry of the residuum. To place the sensor it was needed to be stretched and, as mentioned before, both patterns have

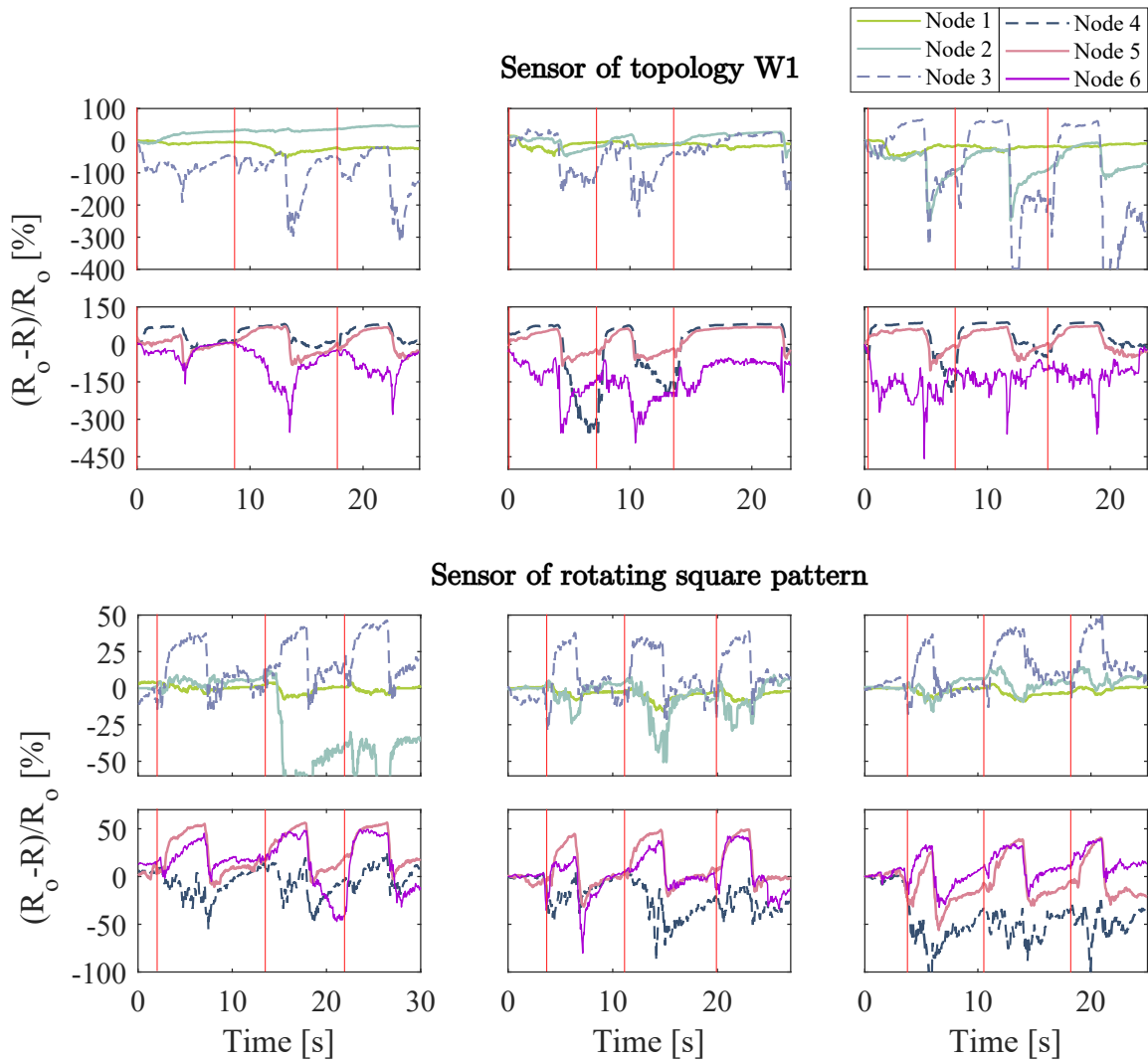


Figure 5.21: Relative resistance in terms of time plots for each run performed with Topology W1 and Rotating square sensors of the simulation of a person standing three times.

different deformation mechanisms. This is visually exposed in figure 5.22 where the strain of both patterns is mapped from a finite element simulation. The stretching of the lattice (figure 5.22a.) produces strain in the sine waves oriented along the axis of the load. To conform the residual limb it was needed stretching in both axis, which in turn, results in strain in the whole sample. Meanwhile, the rotation of the squares (figure 5.22a.) causes

the strain to concentrate only at the hinges of the pattern. This allows to have electrodes that are almost strain-free; generated by conformability.

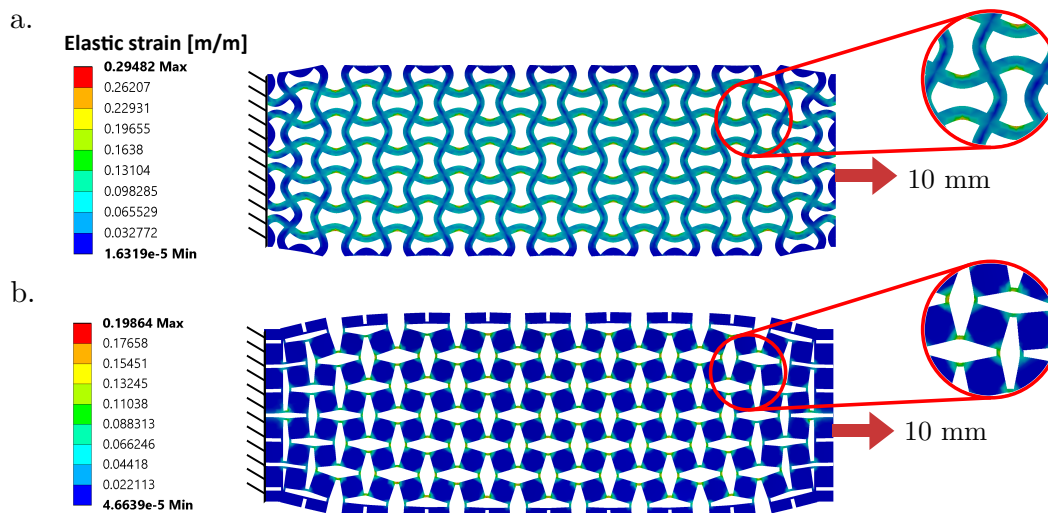


Figure 5.22: Location of the measuring points marked in the sensor samples with geometries a. Topology W1, and b. Rotating square.

It was found a similar behavior of the nodes 1 and 6 in the rotating square sensor compared to a previous evaluation of FSRs as in-socket pressure devices [1]. These were the only nodes that match the location of measuring points studied before.

## 5.6 Summary

The implementation of different arrangements of material to electro-conductive films and their instrumentation to build pressure sensing devices was achieved. These resulted low cost and easy to integrate, with some drawbacks. Mainly intrinsic from the material's properties and fabrication method, which did not allow accurate measurements of pressure. The fabrication method and instrumentation translated to a high variation of resistance range, even in the same sheet of material. According to literature [16] other factors, such as thermal response, are needed to be taken into account. It could be possible to model this effects, however it would cost computational capability to use this material in a real-time biomedical device.

However, the study allowed to obtain a general view of their behavior under different types of loads. There were found major variations on tensile loading of the sensor with sinusoidal topology W2, not present in the periodic cut patterned sensors. This comparison revealed a relation between the deformation mechanism and their response to this types of loads. In the implementation as in-socket pressure device, it was found that the strain produced by the stretching of the material affected the measurement of pressure by the sensor with topology W1. The rotation of the hinges of the periodic cut pattern samples make them an ideal design for this type of devices. Thus electrodes can be placed on most part of the material without altering the measurements with strain. Awareness to the type of deformation mechanism, along with relative density and auxeticity is key when deciding the type of geometry to apply. This brings great potential of implementing these patterns to other materials for reliable and conformable sensors.

This research paves the way to explore more into the mechanical behavior of auxetic structures implemented in sensors. Other materials and fabrication techniques would allow to make smaller samples to use other type of testing machine that could detect the small forces and consider adding stiffness to the evaluation of different topologies. Moreover, taking into account the irregular shape of the residual limb, a non-uniform functionally graded topology could be tuned with localized specific Poisson's ratio and strain characteristics.

# Chapter 6

## Conclusions and future work

In this chapter, conclusions from each chapter are summarized in the broader perspective of the potential of auxetic metamaterials in biomedical engineering. Further research possibilities are presented.

### 6.1 General conclusions

The parameterization and design of sinusoid based topologies was achieved. This allowed to model and fabricate them with variation of their geometrical parameters. An analysis of the effect on their in-plane (relative density and Poisson's ratio) and out-of-plane (stiffness and conformability) properties was performed. This brought up that amplitude increases relative density, when the other parameters ( $\lambda$  and  $t$ ) are kept constant. Also, independent from the individual values of the three geometrical parameters, different topologies of sinusoid W1 can be designed with the same Poisson's ratio by maintaining the amplitude to thickness ratio  $A/t$ . Moreover, auxetic topologies of the sinusoid W2 are obtained with small values of  $t$ , and changes in  $A$  or  $\lambda$  are almost negligible. By maintaining a thickness to length ratio  $t/\lambda$  different topologies of sinusoid W2 with the same Poisson's ratio can be designed. This offers the possibility to design topologies with targeted Poisson's ratio with geometrical considerations for specific applications.

With finite element modelling (FEM) of out-of-plane loading, thickness  $t$  was found

to make the topologies stiffer, regardless of the other parameters and type of topology. In less magnitude, incrementing the value of  $A$  results in more flexible topologies, even though it increases the relative density. These results were validated with experimental tests of additive manufactured samples. Samples with thicker features than the intended CAD models produced around 28% error in comparison with the FEM results. A conformability ratio to quantify adaptability of the fabricated samples to a sphere was proposed. The statistical analysis with a 95% confidence level stated that conformability ratio was mostly affected by  $\lambda$  and, specifically to topology W2,  $t$  also affected the response. These results were analyzed in terms of stiffness, and revealed topologies with similar conformability ratio (1% variation) with significant differences in stiffness. Meaning that some topologies conform the same area but with more or less magnitude of force, which is proportional to the area of material in contact with the target surface. One needs to be aware that despite having similar conformability ratios, a relation to the stiffness is needed. Increasing the amount of material needed to be in contact with the target surface will increase the stiffness without affecting significantly the conformability ratio.

The implementation of different arrangements of material to electro-conductive films and their instrumentation to build sensing devices was achieved. Some drawbacks, intrinsic to the materials properties and fabrication method were found and did not allow accurate measurements of pressure. However, a general view of their behavior under different types of loads was obtained. Compared to periodic cut patterned samples, sinusoidal topologies presented major variations on tensile loading. Also, when testing the samples as in-socket sensors, the strain produced by stretching the material to conform the artificial residual limb affected the measurements of pressure. This revealed a relation between the deformation mechanism and their response to these types of loads. The rotation of the hinges of the periodic cut patterned samples make them ideal for these devices, since it allows to take pressure measurements without affecting the signal with strain. Less than 5% variation of the voltage was obtained in comparison with the sinusoidal topologies with variations up to 56%. Awareness of the deformation mechanism, along with their relative density and auxetic behavior is key when deciding the geometry to implement.

The main contributions of this thesis are the following:

- Thorough analysis of the effect of the geometrical parameters of two sinusoid based

topologies on their Poisson's ratio.

- Out-of-plane stiffness characterization not found in literature for these topologies and its validation with experimental tests of additive manufactured samples.
- Novel technique to quantify conformability of auxetic structures to curved geometries using image processing.
- An analysis that allowed to establish a relation between conformability and stiffness of the samples.
- The implementation of auxetic topologies to fabricate pressure sensor samples was done for the first time in this project.
- Relation between the topology and electrical response of auxetic structures implemented in sensors which could allow to decide the best geometry to implement.

## 6.2 Future work

There are several aspects of auxetic structures and its application in biomedical engineering that require further study. These are presented below:

- Laboratory experiments to characterize additive manufactured Poisson's ratio of sinusoid based samples.
- Study of the out-of-plane behavior with other mechanical properties.
- Trajectory planning to obtain additive manufactured samples with continuous filament along the sine waves.
- Improve conformability ratio as a quantification variable.
- FEM and laboratory experiments of conformability to other complex-curved geometries.



- Functionally graded design of sinusoid samples specific to a curved geometry with targeted Poisson's ratio and strain.
- Exploration of other materials and fabrication techniques for accurate sensors.
- Study of the dynamic response of the sensors to obtain a model that can convert the measurements of electrical resistance to pressure.
- Fabrication of smaller pressure sensing samples to use a mechanical testing machine to detect small forces. This would allow to add other variables (stiffness) to the evaluation of auxetic structures and electric response.

# Appendix A

## Sine topologies generator

The following code is used to generate the sinusoidal curves for the CAD models.

```
' *****  
'macro recorded by Diana Laura Ramirez Gutierrez  
'This macro creates the unit cell for sine lattices as  
'splines by selecting each line that conforms it and then  
'fitting it to a spline  
' *****  
Dim swApp As Object  
Dim Part As Object  
Dim boolstatus As Boolean  
Dim longstatus As Long, longwarnings As Long  
  
Sub main()  
Set swApp = Application.SldWorks  
Set Part = swApp.ActiveDoc  
Dim COSMOSWORKSObj As Object  
Dim CWAddinCallBackObj As Object  
Set CWAddinCallBackObj = swApp.GetAddInObject("CosmosWorks.CosmosWorks")  
Set COSMOSWORKSObj = CWAddinCallBackObj.COSMOSWORKS
```

```
Dim skSegment As Object
Dim addToDbOrig As Boolean

addToDbOrig = Part.SketchManager.AddToDB 'get the original value
Part.SketchManager.AddToDB = True

'Initialize variables
Dim w As Integer
Dim lambda As Double
Dim k As Double
Dim A As Double
Dim x As Double
Dim y As Double
Dim t As Double
Dim pi As Double
pi = 4 * Atn(1)

'Input parameters values
w = 2 'Type of topology 1 or 2,
      'for the square lattice can be any value
lambda = 5 'length of unit cell (mm)
k = w * pi / lambda
A = 0.8 'Amplitude
thick = 1.5 / 2 'Thickness (mm)

stp = 0.05 'Separation between points

'Initialize parameters
numLines = lambda / stp / 2
b = thick * A * k
c = A * k
```

```

'First point position
tStart = -lambda / 2
tEnd = lambda / 2
lineID = 0
piXUp = tStart + b * Cos(k * tStart) / Sqrt(1 + (c * Cos(k * tStart))^2)
piYUp = A * Sin(k * tStart) - thick / Sqrt(1 + (c * Cos(k * tStart))^2)
piXDn = tStart - b * Cos(k * tStart) / Sqrt(1 + (c * Cos(k * tStart))^2)
piYDn = A * Sin(k * tStart) + thick / Sqrt(1 + (c * Cos(k * tStart))^2)
Part.ClearSelection2 True

'Make the upper horizontal left curve with lines between 2 points
For t = -lambda / 2 To 0 Step stp
'Calcualte coordinates of new point
    pXUp = t + b * Cos(k * t) / Sqrt(1 + (c * Cos(k * t)) ^ 2)
    pYUp = A * Sin(k * t) - thick / Sqrt(1 + (c * Cos(k * t)) ^ 2)
    pXDn = t - b * Cos(k * t) / Sqrt(1 + (c * Cos(k * t)) ^ 2)
    pYDn = A * Sin(k * t) + thick / Sqrt(1 + (c * Cos(k * t)) ^ 2)
'Create line between previous and new point
    Set skSegment = Part.SketchManager.CreateLine(piXUp / 1000,
    piYUp / 1000, 0#, pXUp / 1000, pYUp / 1000, 0#)
    piXUp = pXUp
    piYUp = pYUp
    piXDn = pXDn
    piYDn = pYDn
Next t
Part.ClearSelection2 True
'Select all lines created to convert to spline
For lines = 1 To numLines
    lineID = lineID + 1
    boolstatus = Part.Extension.SelectByID2("Line" & lineID,

```

```

    "SKETCHSEGMENT", 0, 0, 0, True, 0, Nothing, 0)
Next lines
boolstatus=Part.FeatureManager.MakeStyledCurves2(1.76224806751733E-06,10)
Part.ClearSelection2 True

'Make the upper horizontal right curve with lines between 2 points
For t = stp To lambda / 2 Step stp
    pXUp = t + b * Cos(k * t) / Sqrt(1 + (c * Cos(k * t)) ^ 2)
    pYUp = A * Sin(k * t) - thick / Sqrt(1 + (c * Cos(k * t)) ^ 2)
    pXDn = t - b * Cos(k * t) / Sqrt(1 + (c * Cos(k * t)) ^ 2)
    pYDn = A * Sin(k * t) + thick / Sqrt(1 + (c * Cos(k * t)) ^ 2)
    Set skSegment = Part.SketchManager.CreateLine(piXUp / 1000,
    piYUp / 1000, 0#, pXUp / 1000, pYUp / 1000, 0#)
    piXUp = pXUp
    piYUp = pYUp
    piXDn = pXDn
    piYDn = pYDn
Next t
Part.ClearSelection2 True
'Select all lines created to convert to spline
For lines = 1 To numLines
    lineID = lineID + 1
    boolstatus = Part.Extension.SelectByID2("Line" & lineID,
    "SKETCHSEGMENT", 0, 0, 0, True, 0, Nothing, 0)
Next lines
boolstatus=Part.FeatureManager.MakeStyledCurves2(1.76224806751733E-06,10)
Part.ClearSelection2 True
piXUp = tStart + b * Cos(k * tStart) / Sqrt(1 + (c * Cos(k * tStart))^2)
piYUp = A * Sin(k * tStart) - thick / Sqrt(1 + (c * Cos(k * tStart))^2)
piXDn = tStart - b * Cos(k * tStart) / Sqrt(1 + (c * Cos(k * tStart))^2)
piYDn = A * Sin(k * tStart) + thick / Sqrt(1 + (c * Cos(k * tStart))^2)

```

```

'Make the lower horizontal left curve with lines between 2 points
For t = -lambda / 2 To 0 Step stp
  pXUp = t + b * Cos(k * t) / Sqrt(1 + (c * Cos(k * t)) ^ 2)
  pYUp = A * Sin(k * t) - thick / Sqrt(1 + (c * Cos(k * t)) ^ 2)
  pXDn = t - b * Cos(k * t) / Sqrt(1 + (c * Cos(k * t)) ^ 2)
  pYDn = A * Sin(k * t) + thick / Sqrt(1 + (c * Cos(k * t)) ^ 2)
  Set skSegment = Part.SketchManager.CreateLine(piXDn / 1000,
  piYDn / 1000, 0#, pXDn / 1000, pYDn / 1000, 0#)
  piXUp = pXUp
  piYUp = pYUp
  piXDn = pXDn
  piYDn = pYDn
Next t
Part.ClearSelection2 True
'Select all lines created to convert to spline
For lines = 1 To numLines
  lineID = lineID + 1
  boolstatus = Part.Extension.SelectByID2("Line" & lineID,
  "SKETCHSEGMENT", 0, 0, 0, True, 0, Nothing, 0)
Next lines
boolstatus=Part.FeatureManager.MakeStyledCurves2(1.76224806751733E-06,10)
Part.ClearSelection2 True

'Make the lower horizontal right curve with lines between 2 points
For t = stp To lambda / 2 Step stp
  pXUp = t + b * Cos(k * t) / Sqrt(1 + (c * Cos(k * t)) ^ 2)
  pYUp = A * Sin(k * t) - thick / Sqrt(1 + (c * Cos(k * t)) ^ 2)
  pXDn = t - b * Cos(k * t) / Sqrt(1 + (c * Cos(k * t)) ^ 2)
  pYDn = A * Sin(k * t) + thick / Sqrt(1 + (c * Cos(k * t)) ^ 2)
  Set skSegment = Part.SketchManager.CreateLine(piXDn / 1000,

```

```

    piYDn / 1000, 0#, pXDn / 1000, pYDn / 1000, 0#)
    piXUp = pXUp
    piYUp = pYUp
    piXDn = pXDn
    piYDn = pYDn
Next t
Part.ClearSelection2 True
'Select all lines created to convert to spline
For lines = 1 To numLines
    lineID = lineID + 1
    'MsgBox "line it: " & lines & " line selected: " & lineID
    boolstatus = Part.Extension.SelectByID2("Line" & lineID,
        "SKETCHSEGMENT", 0, 0, 0, True, 0, Nothing, 0)
Next lines
boolstatus=Part.FeatureManager.MakeStyledCurves2(1.76224806751733E-06,10)
Part.ClearSelection2 True

'Initialize parameters to make the vertical curves
piXUp = tStart + b * Cos(k * tStart) / Sqrt(1 + (c * Cos(k * tStart))^2)
piYUp = A * Sin(k * tStart) - thick / Sqrt(1 + (c * Cos(k * tStart))^2)
piXDn = tStart - b * Cos(k * tStart) / Sqrt(1 + (c * Cos(k * tStart))^2)
piYDn = A * Sin(k * tStart) + thick / Sqrt(1 + (c * Cos(k * tStart))^2)

'Make the left vertical bottom curve with lines between 2 points
For t = -lambda / 2 To 0 Step stp
    pXUp = t + b * Cos(k * t) / Sqrt(1 + (c * Cos(k * t)) ^ 2)
    pYUp = A * Sin(k * t) - thick / Sqrt(1 + (c * Cos(k * t)) ^ 2)
    pXDn = t - b * Cos(k * t) / Sqrt(1 + (c * Cos(k * t)) ^ 2)
    pYDn = A * Sin(k * t) + thick / Sqrt(1 + (c * Cos(k * t)) ^ 2)
    Set skSegment = Part.SketchManager.CreateLine(-piYDn / 1000,
        piXDn / 1000, 0#, -pYDn / 1000, pXDn / 1000, 0#)

```

```

    piXUp = pXUp
    piYUp = pYUp
    piXDn = pXDn
    piYDn = pYDn
Next t
Part.ClearSelection2 True
'Select all lines created to convert to spline
For lines = 1 To numLines
    lineID = lineID + 1
    boolstatus = Part.Extension.SelectByID2("Line" & lineID,
        "SKETCHSEGMENT", 0, 0, 0, True, 0, Nothing, 0)
Next lines
boolstatus=Part.FeatureManager.MakeStyledCurves2(1.76224806751733E-06,10)
Part.ClearSelection2 True

'Make the left vertical top curve with lines between 2 points
For t = stp To lambda / 2 Step stp
    pXUp = t + b * Cos(k * t) / Sqrt(1 + (c * Cos(k * t)) ^ 2)
    pYUp = A * Sin(k * t) - thick / Sqrt(1 + (c * Cos(k * t)) ^ 2)
    pXDn = t - b * Cos(k * t) / Sqrt(1 + (c * Cos(k * t)) ^ 2)
    pYDn = A * Sin(k * t) + thick / Sqrt(1 + (c * Cos(k * t)) ^ 2)
    Set skSegment = Part.SketchManager.CreateLine(-piYDn / 1000,
        piXDn / 1000, 0#, -pYDn / 1000, pXDn / 1000, 0#)
    piXUp = pXUp
    piYUp = pYUp
    piXDn = pXDn
    piYDn = pYDn
Next t
Part.ClearSelection2 True
'Select all lines created to convert to spline
For lines = 1 To numLines

```



```

    lineID = lineID + 1
    boolstatus = Part.Extension.SelectByID2("Line" & lineID,
      "SKETCHSEGMENT", 0, 0, 0, True, 0, Nothing, 0)
Next lines
boolstatus=Part.FeatureManager.MakeStyledCurves2(1.76224806751733E-06,10)
Part.ClearSelection2 True

piXUp = tStart + b * Cos(k * tStart) / Sqrt(1 + (c * Cos(k * tStart))^2)
piYUp = A * Sin(k * tStart) - thick / Sqrt(1 + (c * Cos(k * tStart))^2)
piXDn = tStart - b * Cos(k * tStart) / Sqrt(1 + (c * Cos(k * tStart))^2)
piYDn = A * Sin(k * tStart) + thick / Sqrt(1 + (c * Cos(k * tStart))^2)

'Make the right vertical bottom curve with lines between 2 points
For t = -lambda / 2 To 0 Step stp
    pXUp = t + b * Cos(k * t) / Sqrt(1 + (c * Cos(k * t)) ^ 2)
    pYUp = A * Sin(k * t) - thick / Sqrt(1 + (c * Cos(k * t)) ^ 2)
    pXDn = t - b * Cos(k * t) / Sqrt(1 + (c * Cos(k * t)) ^ 2)
    pYDn = A * Sin(k * t) + thick / Sqrt(1 + (c * Cos(k * t)) ^ 2)
    Set skSegment = Part.SketchManager.CreateLine(-piYUp / 1000,
      piXUp / 1000, 0#, -pYUp / 1000, pXUp / 1000, 0#)
    piXUp = pXUp
    piYUp = pYUp
    piXDn = pXDn
    piYDn = pYDn
Next t
Part.ClearSelection2 True
'Select all lines created to convert to spline
For lines = 1 To numLines
    lineID = lineID + 1
    boolstatus = Part.Extension.SelectByID2("Line" & lineID,
      "SKETCHSEGMENT", 0, 0, 0, True, 0, Nothing, 0)

```

Next lines

```
boolstatus=Part.FeatureManager.MakeStyledCurves2(1.76224806751733E-06,10)
Part.ClearSelection2 True
```

'Make the right vertical top curve with lines between 2 points

```
For t = stp To lambda / 2 Step stp
```

```
    pXUp = t + b * Cos(k * t) / Sqrt(1 + (c * Cos(k * t)) ^ 2)
```

```
    pYUp = A * Sin(k * t) - thick / Sqrt(1 + (c * Cos(k * t)) ^ 2)
```

```
    pXDn = t - b * Cos(k * t) / Sqrt(1 + (c * Cos(k * t)) ^ 2)
```

```
    pYDn = A * Sin(k * t) + thick / Sqrt(1 + (c * Cos(k * t)) ^ 2)
```

```
    Set skSegment = Part.SketchManager.CreateLine(-piYUp / 1000,
    piXUp / 1000, 0#, -pYUp / 1000, pXUp / 1000, 0#)
```

```
    piXUp = pXUp
```

```
    piYUp = pYUp
```

```
    piXDn = pXDn
```

```
    piYDn = pYDn
```

Next t

```
Part.ClearSelection2 True
```

'Select all lines created to convert to spline

```
For lines = 1 To numLines
```

```
    lineID = lineID + 1
```

```
    boolstatus = Part.Extension.SelectByID2("Line" & lineID,
    "SKETCHSEGMENT", 0, 0, 0, True, 0, Nothing, 0)
```

Next lines

```
boolstatus=Part.FeatureManager.MakeStyledCurves2(1.76224806751733E-06,10)
```

```
Part.ClearSelection2 True
```

```
Part.SketchManager.AddToDB = addToDbOrig 'restore the original value
```

```
End Sub
```

# Bibliography

- [1] AGUILA, S. I., SÁNCHEZ, G. J., SAUVAIN, E. E., ALEMON, B., FUENTES-AGUILAR, R. Q., AND HUEGEL, J. C. Interface pressure system to compare the functional performance of prosthetic sockets during the gait in people with transtibial amputation, 2020.
- [2] AL-FAKIH, E. A., ABU OSMAN, N. A., AND MAHMAD ADIKAN, F. R. Techniques for interface stress measurements within prosthetic sockets of transtibial amputees: A review of the past 50 years of research. *Sensors (Switzerland)* 16, 7 (2016).
- [3] ALDERSON, A., ALDERSON, K. L., CHIRIMA, G., RAVIRALA, N., AND ZIED, K. M. The in-plane linear elastic constants and out-of-plane bending of 3-coordinated ligament and cylinder-ligament honeycombs. *Composites Science and Technology* 70, 7 (jul 2010), 1034–1041.
- [4] ANWARY, A. R., BOUCHACHIA, H., AND VASSALLO, M. Real time visualization of asymmetrical sitting posture. In *Procedia Computer Science* (jan 2019), vol. 155, Elsevier B.V., pp. 153–160.
- [5] BELLO RUIZ, J. M., AND DIAZ ROMERO, J. M. Diseño y desarrollo de un prototipo de medición de presión plantar portátil. 1–8.
- [6] CHEN, D. H. Bending deformation of honeycomb consisting of regular hexagonal cells. *Composite Structures* 93, 2 (jan 2011), 736–746.
- [7] CHO, H., SEO, D., AND KIM, D.-N. Mechanics of Auxetic Materials. *Handbook of Mechanics of Materials* (2018), 1–25.

- [8] CHOW, L., LUN YICK, K., WONG, K. H., HANG LEUNG, M. S., SUN, Y., YING KWAN, M., NING, K., YU, A., YIP, J., FAN CHAN, Y., AND PUI NG, S. 3D Printing Auxetic Architectures for Hypertrophic Scar Therapy. *Macromolecular Materials and Engineering* (2022).
- [9] DE BELLIS, M. L., AND BACIGALUPO, A. Auxetic behavior and acoustic properties of microstructured piezoelectric strain sensors. *Smart Materials and Structures* 26, 8 (2017).
- [10] DUNCAN, O., SHEPHERD, T., MORONEY, C., FOSTER, L., VENKATRAMAN, P. D., WINWOOD, K., ALLEN, T., AND ALDERSON, A. Review of auxetic materials for sports applications: Expanding options in comfort and protection, jun 2018.
- [11] FRIEDRICH, J., AND GENGNAGEL, C. Multi-layered auxetic structures for doubly-curved shapes. Tech. rep., 2018.
- [12] FRIEDRICH, J., PFEIFFER, S., AND GENGNAGEL, C. Locally Varied Auxetic Structures for Doubly-Curved Shapes. In *Humanizing Digital Reality*. Springer Singapore, 2018, pp. 323–336.
- [13] GOMEZ, M. Master thesis.
- [14] HAN, Y., AND LU, W. F. Structural design of wearable electronics suitable for highly-stretched joint areas. *Smart Materials and Structures* 27, 10 (sep 2018), 105042.
- [15] HEIKENFELD, J., JAJACK, A., ROGERS, J., GUTRUF, P., TIAN, L., PAN, T., LI, R., KHINE, M., KIM, J., WANG, J., AND KIM, J. Wearable sensors: Modalities, challenges, and prospects, jan 2018.
- [16] HOPKINS, M., VAIDYANATHAN, R., AND MCGREGOR, A. H. Examination of the Performance Characteristics of Velostat as an In-Socket Pressure Sensor. *IEEE Sensors Journal* 20, 13 (2020), 6992–7000.

- [17] JAVAID, M., AND HALEEM, A. Current status and applications of additive manufacturing in dentistry: A literature-based review. *Journal of oral biology and craniofacial research* 9, 3 (2019), 179–185.
- [18] JIANG, Y., LIU, Z., MATSUHISA, N., QI, D., LEOW, W. R., YANG, H., YU, J., CHEN, G., LIU, Y., WAN, C., LIU, Z., AND CHEN, X. Auxetic Mechanical Metamaterials to Enhance Sensitivity of Stretchable Strain Sensors. *Advanced Materials* 30, 12 (2018), 1–8.
- [19] KABIR, S., KIM, H., AND LEE, S. Physical property of 3D-printed sinusoidal pattern using shape memory TPU filament. *Textile Research Journal* (2020).
- [20] KANG, M., KIM, J., JANG, B., CHAE, Y., KIM, J. H., AND AHN, J. H. Graphene-Based Three-Dimensional Capacitive Touch Sensor for Wearable Electronics. *ACS Nano* 11, 8 (aug 2017), 7950–7957.
- [21] KAPNISI, M., MANSFIELD, C., MARIJON, C., GUEX, A. G., PERBELLINI, F., BARDI, I., HUMPHREY, E. J., PUETZER, J. L., MAWAD, D., KOUTSOGEORGIS, D. C., STUCKEY, D. J., TERRACCIANO, C. M., HARDING, S. E., AND STEVENS, M. M. Auxetic Cardiac Patches with Tunable Mechanical and Conductive Properties toward Treating Myocardial Infarction. *Advanced Functional Materials* 28, 21 (2018).
- [22] KELKAR, P. U., KIM, H. S., CHO, K. H., KWAK, J. Y., KANG, C. Y., AND SONG, H. C. Cellular auxetic structures for mechanical metamaterials: A review, 2020.
- [23] KIM, H. W., KIM, T. Y., PARK, H. K., YOU, I., KWAK, J., KIM, J. C., HWANG, H., KIM, H. S., AND JEONG, U. Hygroscopic Auxetic On-Skin Sensors for Easy-to-Handle Repeated Daily Use. *ACS Applied Materials and Interfaces* 10, 46 (2018), 40141–40148.
- [24] KO, J., BHULLAR, S., CHO, Y., LEE, P. C., AND BYUNG-GUK JUN, M. Design and fabrication of auxetic stretchable force sensor for hand rehabilitation. *Smart Materials and Structures* 24, 7 (2015), 75027.

- [25] KONAKOVIĆ, M., CRANE, K., DENG, B., BOUAZIZ, S., PIKER, D., AND PAULY, M. Beyond developable: Computational design and fabrication with auxetic materials. In *ACM Transactions on Graphics* (2016), vol. 35.
- [26] KONAKOVIĆ-LUKOVIĆ, M., PANETTA, J., CRANE, K., AND PAULY, M. Rapid deployment of curved surfaces via programmable auxetics. *ACM Transactions on Graphics* 37, 4 (2018).
- [27] LAI, C. W., AND YU, S. S. 3D Printable Strain Sensors from Deep Eutectic Solvents and Cellulose Nanocrystals. *ACS Applied Materials and Interfaces* 12, 30 (jul 2020), 34235–34244.
- [28] LEE, Y., KIM, J., JANG, B., KIM, S., SHARMA, B. K., KIM, J. H., AND AHN, J. H. Graphene-based stretchable/wearable self-powered touch sensor. *Nano Energy* 62 (aug 2019), 259–267.
- [29] LIN, Y. A., GUPTA, S., PEDTKE, A., AND LOH, K. J. Monitoring pressure distributions at human-socket prostheses interfaces using graphene-fabric sensors. In *Structural Health Monitoring 2019: Enabling Intelligent Life-Cycle Health Management for Industry Internet of Things (IIOT) - Proceedings of the 12th International Workshop on Structural Health Monitoring* (2019), vol. 2, pp. 2061–2068.
- [30] LIU, H., KOLLOSCH, M., YAN, J., ZELLNER, E. M., BENTIL, S. A., RIVERO, I. V., WIERSEMA, C., AND LAFLAMME, S. Numerical investigation of auxetic textured soft strain gauge for monitoring animal skin. *Sensors (Switzerland)* 20, 15 (2020), 1–17.
- [31] MCCAW, J. C., AND CUAN-URQUIZO, E. Curved-Layered Additive Manufacturing of non-planar, parametric lattice structures. *Materials and Design* 160 (dec 2018), 949–963.
- [32] MELNYKOWYCZ, M., TSCHUDIN, M., AND CLEMENS, F. Piezoresistive Carbon-based Hybrid Sensor for Body-Mounted Biomedical Applications. In *IOP Conference Series: Materials Science and Engineering* (feb 2017), vol. 175, Institute of Physics Publishing, p. 012006.

- [33] MERT, L. M., YAMAN, U., AND SAHILLIOĞLU, Y. A fabrication-oriented remeshing method for auxetic pattern extraction. *Turkish Journal of Electrical Engineering and Computer Sciences* 28, 3 (2020), 1535–1548.
- [34] MIR, M., ALI, M. N., SAMI, J., AND ANSARI, U. Review of mechanics and applications of auxetic structures. *Advances in Materials Science and Engineering 2014* (2014).
- [35] MIZZI, L., SALVATI, E., SPAGGIARI, A., TAN, J. C., AND KORSUNSKY, A. M. Highly stretchable two-dimensional auxetic metamaterial sheets fabricated via direct-laser cutting. *International Journal of Mechanical Sciences* 167 (feb 2020), 105242.
- [36] NABONI, R., SARTORI, S., AND MIRANTE, L. Adaptive-Curvature Structures with Auxetic Materials. *Advanced Materials Research* 1149 (aug 2018), 53–63.
- [37] PATTINSON, S. W., HUBER, M. E., KIM, S., LEE, J., GRUNSFELD, S., ROBERTS, R., DREIFUS, G., MEIER, C., LIU, L., HOGAN, N., AND HART, A. J. Additive Manufacturing of Biomechanically Tailored Meshes for Compliant Wearable and Implantable Devices. *Advanced Functional Materials* 29, 32 (2019), 1–10.
- [38] RAMYA, P., PADMAPRIYA, B., AND POORNACHANDRA, S. Foot pressure monitoring using single layer carbon loaded piezoresistive material. *Microprocessors and Microsystems* 79 (nov 2020), 103263.
- [39] REN, X., DAS, R., TRAN, P., NGO, T. D., AND XIE, Y. M. Auxetic metamaterials and structures: A review, 2018.
- [40] SAKAI, Y., AND OHSAKI, M. Parametric Study of Non-Periodic and Hybrid Auxetic Bending-Active Gridshells. *Journal of the International Association for Shell and Spatial Structures* (2021).
- [41] SÁNCHEZ-GONZÁLEZ, C. M., SORIANO-PEÑA, J. F., RUBIO-AVALOS, J. C., AND PACHECO-IBARRA, J. J. Fabrication of flexible piezoresistive sensors based on

- RTV-silicone and milled carbon fibers and the temperature's effect on their electric resistance. *Sensors and Actuators, A: Physical* 302 (feb 2020), 111811.
- [42] SANTOS, A. D., FORTUNATO, E., MARTINS, R., ÁGUAS, H., AND IGREJA, R. Transduction mechanisms, micro-structuring techniques, and applications of electronic skin pressure sensors: A review of recent advances, aug 2020.
- [43] SCHOFIELD, J. S., SCHOEPP, K. R., WILLIAMS, H. E., CAREY, J. P., MARASCO, P. D., AND HEBERT, J. S. Characterization of interfacial socket pressure in transhumeral prostheses: A case series. *PLoS ONE* 12, 6 (2017).
- [44] SPAHIU, T., CANAJ, E., AND SHEHI, E. 3D printing for clothing production. *Journal of Engineered Fibers and Fabrics* 15, August (2020), 0–8.
- [45] SU, X. W., ZHU, D. M., ZHENG, C., AND TOMOVIC, M. M. Mechanical properties of 65Mn chiral structure with three ligaments. *Acta Mechanica Sinica/Lixue Xuebao* 35, 1 (feb 2019), 88–98.
- [46] SWANSON, E. C., WEATHERSBY, E. J., CAGLE, J. C., AND SANDERS, J. E. Evaluation of Force Sensing Resistors for the Measurement of Interface Pressures in Lower Limb Prosthetics. *Journal of Biomechanical Engineering* 141, 10 (oct 2019), 1010091.
- [47] TARAR, A. A., MOHAMMAD, U., AND SRIVASTAVA, S. K. Wearable skin sensors and their challenges: A review of transdermal, optical, and mechanical sensors, 2020.
- [48] VEDANT, R. M., KRUGH, M., AND MEARS, L. Measuring finger engagement during manual assembly operations in automotive assembly. In *Procedia Manufacturing* (jan 2019), vol. 34, Elsevier B.V., pp. 1005–1009.
- [49] VIJAYAVENKATARAMAN, S., GOPINATH, A., AND LU, W. F. A new design of 3d-printed orthopedic bone plates with auxetic structures to mitigate stress shielding and improve intra-operative bending. *Bio-Design and Manufacturing* 3, 2 (2020), 98–108.



- [50] WANG, B., ZHANG, C., ZENG, C., KRAMER, L. D., AND GILLIS, A. Prosthetic socket apparatus and systems, Nov. 8 2016. US Patent 9,486,333.
- [51] WANG, H., PAN, C., ZHAO, H., WANG, T., AND HAN, Y. Design of a metamaterial film with excellent conformability and adhesion for bandage substrates. *Journal of the Mechanical Behavior of Biomedical Materials* 124, June (2021), 104799.
- [52] WANG, Z., LUAN, C., LIAO, G., LIU, J., YAO, X., AND FU, J. Progress in Auxetic Mechanical Metamaterials: Structures, Characteristics, Manufacturing Methods, and Applications, oct 2020.
- [53] WONG, J., GONG, A. T., DEFNET, P. A., MEABE, L., BEAUCHAMP, B., SWEET, R. M., SARDON, H., COBB, C. L., AND NELSON, A. 3D Printing Ionogel Auxetic Frameworks for Stretchable Sensors. *Advanced Materials Technologies* 4, 9 (2019), 1–6.
- [54] YANG, S., CHOI, I. S., AND KAMIEN, R. D. Design of super-conformable, foldable materials via fractal cuts and lattice kirigami. *MRS Bulletin* 41, 2 (2016), 130–137.
- [55] YAO, Y., WANG, L., LI, J., TIAN, S., ZHANG, M., AND FAN, Y. A novel auxetic structure based bone screw design: Tensile mechanical characterization and pullout fixation strength evaluation. *Materials & design* 188 (2020), 108424.
- [56] YEONG, L., LOH, W., CHOON, K., FOO, C., GUPTA, U., WANG, Y., ZHU, J., AND LU, W. F. Soft machines View project Graphene polymer composites View project 3D Printed Metamaterial Capacitive Sensing Array for Universal Jamming Gripper and Human Joint Wearables.

# Curriculum Vitae

Master student was born in Querétaro, México, on December 8, 1996. She earned the Mechatronics Engineering degree from the Instituto Tecnológico y de Estudios Superiores de Monterrey, Queretaro Campus in June 2020. She was accepted in the graduate programs in August 2010.

This document was typed in using  $\text{\LaTeX} 2_{\epsilon}$ <sup>a</sup> by Diana Laura Ramírez Gutiérrez.

---

<sup>a</sup>The style file `phdThesisFormat.sty` used to set up this thesis was prepared by the Center of Intelligent Systems of the Instituto Tecnológico y de Estudios Superiores de Monterrey, Monterrey Campus